Daniele Faccio,
Arnaud Couairon,
Paolo Di Trapani

Conical Waves, Filaments and Nonlinear Filamentation Optics.

Preface

X-waves, O-waves, Bessel beams or more generically Conical waves are characterized by quasi-stationary propagation in all media, they have a central, intense peak that does not diffract and does not spread in time, they have potentially tunable phase and group velocities and they have even proved to be robust against nonlinear losses. These features are maintained both in the linear regime and at high intensities rendering them unique with respect to other stationary wave-packets, such as the soliton.

As with many discoveries, the dramatic beauty of nature played a key role. In the late nineties a series of experiments in world-wide laboratories were investigating the long range filamentation of ultrashort laser pulses in a variety of media, ranging from glass to air. One of the most beautiful features of this was the generation of white light spread over a cone which, when observed through a spectrometer, showed incredible shapes and colors and an X-shaped multicolored spectrum that was cut in two by a strong rainbow of light with paraboliclike modulation patterns: an object of such beauty demanded an explanation!

Put in very simple terms, the research described in this work is dedicated to the understanding the beautiful features of these and similar spectra.

We shall describe the role and importance of Conical waves with a strongly experimental approach: the first chapters will give the information necessary to understand the physical processes that shall be treated later on. Many of the topics covered may be found in excellent text books and the reader will be referred to these for further reading. We shall then investigate into some depth the various experimental diagnostic tools that have been developed by the authors and coworkers and how these should be used, or not used, in order to derive the greatest amount of information possible regarding the nature of ultrashort conical wave-packets. We shall focus mainly on the role of conical waves in laser pulse filamentation. This indeed is a most demanding and interesting regime where a correct use of the diagnostics and full spatio-temporal characterization of the laser pulse shed new light

on a process that has been attracting attention since its first prediction and discovery in the 1960's.

A large number of individuals have contributed either directly or indirectly to the completion of this book. Particular thanks go to all members of the Virtual Institute of Nonlinear Optics (VINO, www.vino-stella.eu), directed by Prof. Paolo Di Trapani and involving many people from around the world: Prof. A. Piskarskas, Prof. A. Dubietis, Prof. G. Valiulis, Dr. G. Tamošauskas, Dr. A. Matijosius, Dr. A. Varanavičius, R. Piskarskas, E. Kucinskas (Department of Quantum Electronics, Vilnius University, Lithuania where many of the experiments were performed), Prof. M.A. Porras (Universidad Politécnica de Madrid, Spain), Prof. J. Trull (Universitat Politècnica de Catalunya, Spain), Prof. V. Degiorgio, Dr. F. Bragheri, Dr. C. Liberale (Università di Pavia, Italy), Prof. A. Parola, Dr. O. Jedrkiewicz, Dr. D. Salerno, A. Averchi, M. Clerici, P. Polesana (Università dell'Insubria, Como, Italy), S. Minardi (TEI, Chania, Crete), and finally Prof. M. Kolesik and Prof. J.V. Moloney (Department of Mathematics, University of Arizona, USA).

This book originated as a report of my PhD thesis: I am particularly grateful to Arnaud Couairon whose code (described in chapter 4) was constantly used during this work, to Paolo Di Trapani who followed the scientific progress day by day and finally to Prof. Jorge Tredicce for his precious time. Without the invaluable contributions of these and many others the work described in this book would never have been possible.

The authors currently work at the Department of Mathematics and Physics, University of Insubria, Como, Italy (Daniele Faccio), CNRS, École Polytechnique, Palaiseau, France (Arnaud Couairon) and Marie Curie Chair at the Department of Quantum Electronics, Vilnius University, Lithuania (Paolo Di Trapani, permanent address University of Insubria, Como).

Como *Daniele*
2007 *Faccio*

Contents

1

Ultrashort laser pulse filamentation

In this chapter we shall review some of the physics and more important aspects of ultrashort laser pulse filamentation in media with a Kerr nonlinearity. The best starting point for this is a description of the nonlinear effects experienced by intense laser pulses propagating in dispersive media. Some of these (such as Cross-Phase-Modulation or Stimulated Raman Scattering) may not have an immediately obvious relevance to the case of ultrashort laser pulse filamentation but understanding them will come in handy later on.

1.1 Kerr nonlinearity: self-action effects

All materials, ranging from solids to low-pressure gases, possess a third order optical nonlinearity and many of the associated physical effects are very general, displaying common features in many different media. The origin of the nonlinear optical response lies in the material response to an external electrical field. This response manifests itself as a charge displacement and, if the electric field becomes intense enough the charge displacement, or polarization, becomes a nonlinear function of the field. We shall speak of "self-action" effects when the propagation of the field is affected by the nonlinear polarization it itself has induced. The basic coupling between the optical field and the material occurs through outer shell or band electrons and the temporal response of these interactions is extremely fast, less than 1 fs, and may be considered as instantaneous at optical frequencies. This nonlinearity is often referred to as the Kerr nonlinearity. However slower molecular motions may also contribute to the nonlinear response and may lead to very large nonlinearities. An example is Stimulated Raman Scattering that shall be treated below.
In general it is possible to adopt a perturbative approach to the description of the nonlinear material response and write the material polarization vector in the frequency domain

$$\boldsymbol{P}(\boldsymbol{E}) = \chi^{(1)}\boldsymbol{E} + \chi^{(2)}\boldsymbol{E}\boldsymbol{E} + \chi^{(3)}\boldsymbol{E}\boldsymbol{E}\boldsymbol{E} + \cdots . \tag{1.1}$$

The first order term in this Taylor expansion will give the linear material response, usually described through the refractive index $n = \sqrt{1+\chi^{(1)}}$. The second order term is present only in non-centrosymmetric media, e.g. certain crystals or organized organic molecules. The majority of known elements aggregate in an amorphous state (gases, liquids, glasses etc.) and for these the lowest order nonlinearity is represented by the $\chi^{(3)}$ tensor, i.e. the Kerr nonlinearity. Collecting a common E-term in Eq.1.1 the refractive index may be written as

$$n = \sqrt{1 + \chi^{(1)} + \frac{3}{4}\chi^{(3)}|A|^2} \simeq n_0 + \frac{3}{8n_0}\chi^{(3)}|A|^2, \tag{1.2}$$

where $\boldsymbol{E} = \boldsymbol{A}\exp[j(kz-\omega t)]$ is the electric field and n_0 is the linear refractive index. The 3/4 multiplicative constant that appears here is due to a degeneracy that arises in the case of isotropic media (so that only diagonal terms in the tensor are different from zero and are also equal to each other) and in the case in which all interacting fields have the same frequency (see for example Ref.[1] or [2]). So we see that the Kerr term gives rise to an intensity dependent refractive index that may in general be complex. Let us now derive a wave-equation for the envelope A of the electric field into which we may insert the expression in Eq.1.2. A convenient way to derive the envelope equation is to Taylor expand the wave number $k = k(\omega, |A|^2)$ around the carrier frequency ω_0 and the electric field intensity $|A|^2$. Retaining only the lowest order of the group velocity dispersion (variation of the group velocity as a function of the light frequency) and under the paraxial approximation[1] $k_x^2 + k_y^2 << k_0^2$ we find:

$$\begin{aligned} k - k_0 = k - \sqrt{k_{0z}^2 - (k_x^2 + k_y^2)} \simeq \\ k - k_{0z} - \frac{1}{2}\frac{k_x^2 + k_y^2}{k_{0z}} \simeq k_0'(\omega - \omega_0) + \frac{1}{2}k_0''(\omega-\omega_0)^2 + \frac{\partial k}{\partial |A|^2}|A|^2, \end{aligned} \tag{1.3}$$

where k_{0z} indicates the longitudinal component of k calculated in ω_0. From here on primed variables will indicate derivatives with respect to ω. Eq.1.3 is written in Fourier space but may be easily converted to direct space by replacing

[1] This implies that the transverse components of the wavevector are small with respect to the longitudinal term, i.e. the propagation angles with respect to the propagation direction are small.

$$k - k_{0z} - \frac{1}{2}\frac{k_x^2 + k_y^2}{k_0} \quad \text{with} \quad j\frac{\partial}{\partial z} + \frac{1}{2k_0}\left(\frac{\partial^2}{\partial x^2} + \frac{\partial^2}{\partial y^2}\right),$$

$$\text{and} \quad \omega - \omega_0 \quad \text{with} \quad j\frac{\partial}{\partial t}.$$

The resulting equation reads

$$j\left(\frac{\partial A}{\partial z} + k'\frac{\partial A}{\partial t}\right) + \frac{1}{2k_0}\nabla_\perp^2 A - \frac{k''}{2}\frac{\partial^2 A}{\partial t^2} + \frac{\partial k}{\partial A^2}|A|^2 A = 0. \tag{1.4}$$

If we use the definition of the group velocity, $v_g = 1/k'$, and take $\partial k/\partial(A^2) \simeq (3/8n_0)(\omega_0/c)\chi^{(3)}$ (from Eq.1.2), the evolution of A in the coordinates moving at the pulse group velocity (i.e. $\tau = t - z/v_g$) is given by

$$j\frac{\partial A}{\partial z} + \frac{1}{2k_0}\nabla_\perp^2 A - \frac{k''}{2}\frac{\partial^2 A}{\partial \tau^2} + \frac{3\omega_0}{8cn_0}\chi^{(3)}|A|^2 A = 0. \tag{1.5}$$

The first term of this equation accounts for the z-evolution of the envelope A, the second term describes the effects of diffraction, the third term accounts for material dispersion and finally the last term, which we shall now analyze in detail, accounts for the nonlinearity.

Let us start by considering this equation in a much simpler context, so as to avoid any un-necessary complications while retaining the main physical effects. We may neglect the diffraction term, i.e. we consider the simpler 1D model, and we consider very long pulses so that we may neglect the second order time derivative. We then have a simple equation that allows us to isolate the effect of the nonlinearity alone

$$\frac{\partial A}{\partial z} = j\frac{3\omega_0}{8cn_0}\chi^{(3)}|A|^2 A. \tag{1.6}$$

In general the envelope A may be a complex quantity so that $A = |A|\exp(j\phi)$. The nonlinearity too will typically have a real and an imaginary part (in a similar fashion to the linear refractive index close to an absorption peak), $\chi^{(3)} = \Re[\chi^{(3)}] + j\Im[\chi^{(3)}]$. By equating the real and imaginary parts of Eq.1.6 we find [1]

$$\frac{\partial |A|}{\partial z} = -\frac{3\omega_0}{8c}\Im[\chi^{(3)}]|A|^3, \tag{1.7}$$

$$\frac{\partial \phi}{\partial z} = \frac{3\omega_0}{8c}\Re[\chi^{(3)}]|A|^2. \tag{1.8}$$

From these two equations we may immediately conclude that the imaginary part of the nonlinearity will lead to a modification of the envelope amplitude

(in particular the minus sign in front of the right hand term indicates that the amplitude will decrease) while the real part of the nonlinearity will affect only the envelope phase. Note that is in keeping with what happens in linear matter-wave interactions: the imaginary part of the refractive index is related to an absorption, the real part describes the phase-accumulation. The only difference here is that these effects now depend on the electric field intensity. The equations may be written for the intensity $I = |A|^2$

$$\frac{\partial I}{\partial z} = -\alpha I - \beta I^2, \tag{1.9}$$

$$\frac{\partial \phi}{\partial z} = n_2 I. \tag{1.10}$$

where β and α are the so-called nonlinear absorption coefficient and nonlinear refractive index, respectively. In the first equation we have also included, for generality, the linear absorption term.
The solutions to these equations are quite simple:

$$I(z) = \frac{\alpha I(0) e^{-\alpha z}}{\alpha + \beta I(0)(1 - e^{-\alpha z})}, \tag{1.11}$$

$$\phi(z) = \phi(0) + \frac{n_2}{\beta} \ln \left[1 + \frac{\beta}{\alpha} I_0 (1 - e^{-\alpha z}) \right] \tag{1.12}$$

1.1.1 Multiphoton absorption

Eq.1.11 describes an intensity-dependent absorption. This is often referred to as multiphoton absorption and may be viewed as a "virtual" process by which two photons from the pump are absorbed by passing through an intermediate virtual state. For example a given material may have an absorption band with a lower frequency limit ω_a. Linear absorption will occur if the photon frequency is $\omega > \omega_a$ and the material will be transparent if $\omega < \omega_a$. However, if the intensity is high enough then it is possible for two photons of frequency $\omega = \omega_a/2$ to be absorbed. This process is obviously not limited to just two photon interactions: we may have any number of photons K with frequency $\omega = \omega_a/K$ participating in the absorption. Therefore the absorption cross-section β_K will proceed in a step-like fashion as a function of the optical frequency, with sharp jumps each time the frequency reaches a multiple of ω_a. The generalized equation that describes the multiphoton absorption process is

$$\frac{\partial A}{\partial z} = -\frac{\beta_K}{2} |A|^{2K-2} A, \tag{1.13}$$

whose less trivial solution is

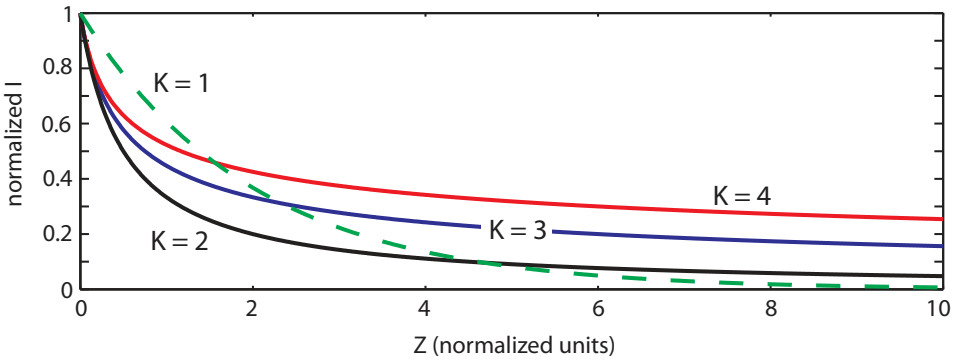

Fig. 1.1. Nonlinear absorption as a function of propagation distance Z. K=1 is simple linear absorption, K=2,3,4 refers to 2, 3 and 4 photon absorption. Nonlinear higher absorption leads to a much faster absorption rate during the early part of the propagation but the loss soon levels out, saturating at some intensity level.

$$I = \frac{I_0}{[1 + I_0^{K-1}\beta_K z(K-1)]^{1/(K-1)}}. \tag{1.14}$$

Fig.1.1 shows the intensity evolution described by Eq.1.14 for four different values of K: $K = 1$ corresponds to linear absorption which shows an exponential decay for all distances z. Nonlinear absoprtion on the other hand is characterized by an initial loss rate that is faster than in the linear case but it soon levels out, reaching a saturation level due to the fact that as the intensity decreases so does the loss rate.

1.1.2 The nonlinear phase shift

Let us now assume that the imaginary part of the nonlinearity is zero and consider the sole effect of the real part. Defining the nonlinear refractive index as

$$n_2 = \frac{3}{8n_0}\chi^{(3)}, \tag{1.15}$$

Eq.1.5 becomes

$$j\frac{\partial A}{\partial z} + \frac{1}{2k_0}\nabla_\perp^2 A - \frac{k''}{2}\frac{\partial^2 A}{\partial \tau^2} + \frac{\omega_0}{c}n_2|A|^2 A = 0. \tag{1.16}$$

It is a custom practice to factorize the impact of the phase intensity dependence into purely spatial or purely temporal effects. Following this approach we first consider the effect of an intensity dependent refractive index on an

ultrashort laser pulse and for the most general case of a positive nonlinear index, $n_2 > 0$. The tails of the optical pulse will have relatively low intensity such that the nonlinear term has no effect. As the intensity increases the refractive index will also increase, reaching a maximum at the pulse peak. n will then decrease along the tail of the pulse until the low-intensity linear value is restored. This will influence the pulse through the phase $\phi = \phi(t) = (2\pi/\lambda)n(t)z - \omega t$. In general the refractive index will follow the pulse intensity profile, will therefore depend on time and therefore also $\phi = \phi(t)$. This will give rise to a frequency broadening:

$$\Delta\omega = -\frac{d\phi(t)}{dt}. \tag{1.17}$$

On the rising edge of the pulse the frequency will be red-shifted, on the trailing edge it will be blue-shifted. Such a frequency-broadening, usually referred to as Self-Phase Modulation (SPM), is routinely observed in the presence of high intensity pulses, e.g. in optical fibers (where the spatial Kerr effect may be effectively ignored) but also in bulk media. The most extreme manifestation of SPM is the generation of the so called white light- or super-continuum. Ever since its first discovery and the proposal of a novel white light laser source, supercontinuum has attracted much attention and is still today a popular topic in laser research.

Let us now discard the temporal behavior of the laser pulse and consider only the spatial Kerr effect. A close analogy may be drawn with the temporal case: the low intensity tails of the spatial beam profile will not be modified by the nonlinear term. Moving toward the central intense part of the beam the refractive index will increase due to the Kerr term and reach a maximum at the beam peak. When discussing the temporal Kerr effect we noted that the time variation of the phase gives rise to a frequency shift that is maximum at the points of highest slope. If we now take the transverse spatial derivative of the phase $\phi = \phi(r) = (2\pi/\lambda)n(r)z - \omega t$

$$\Delta k = \frac{d\phi(r)}{dr}, \tag{1.18}$$

the maximum broadening of the beam wavevector spectrum occurs at the points of maximum intensity variation. If the beam is taken with radial symmetry the overall effect will be very similar to that of a lens. If $n_2 > 0$ the beam will undergo what is called self-focusing (SF) and if $n_2 < 0$ the beam will self-defocus. Fig.1.2 shows an example of the numerically evaluated evolution of a Gaussian beam full-width-half-maximum (FWHM) in the linear regime (diffraction, dash-dot line) and in presence of self-focusing nonlinearity (solid line). The beam contracts to a small diameter reaching a minimum width. At this point, if the intensity is high enough to induce nonlinear (multiphoton) absorption, saturation of self-focusing will occur and a

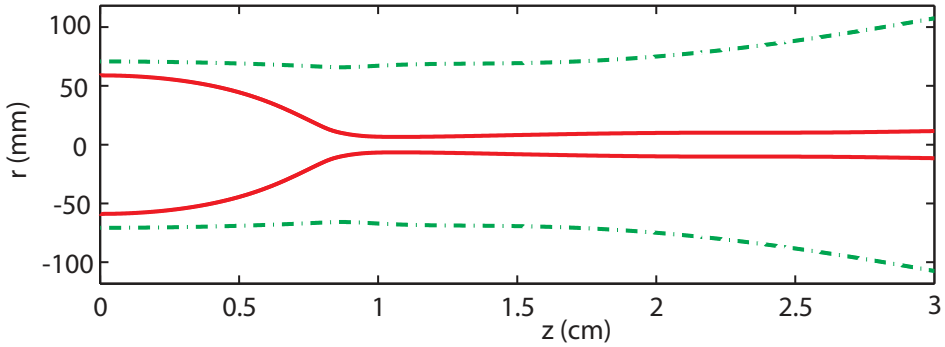

Fig. 1.2. Numerically calculated FWHM of the pulse fluence. The green dash-dot line indicates the evolution of the FWHM in the linear regime (diffraction), the solid red line shows the FWHM evolution in the presence of SF Kerr nonlinearity and NLL as the saturating mechanism.

filament will form, as shown in this example.

We note here that one of the main points that must be considered when treating ultrashort pulse SF and filamentation is that separating the physics into purely spatial or purely temporal effects is acceptable only for a basic comprehension but should otherwise be avoided. Even simple SF of ultrashort pulses, if treated alone, cannot be correctly described without accounting for the temporal dimension. For example in the presence of self-focusing an ultrashort pulse may exhibit a strong temporal compression even in normal group velocity dispersion [2] (see Fig.1.8, e.g. $z = 0.84$ cm). This is counterintuitive as one would expect GVD and SPM to increase the pulse duration. Only by accounting for the full space-time dimension of the pulse may the pulse compression be explained. Indeed SF will affect only the intense, central part of the pulse. The leading and trailing wings will remain unaffected. If viewed in (r, t) coordinates the pulse will assume a butterfly-like shape with central peak that has grown in intensity and therefore has a shortened temporal duration (and, of course, a shrinked diameter).

[2] A short note on terminology. Strictly speaking the terms "normal dispersion" and "anomalous dispersion" refer to spectral ranges in which $dn/d\omega > 0$ and $dn/d\omega < 0$, respectively. Extending such definitions to the second order derivative we speak of "normal group velocity dispersion" (NGVD) and "anomalous group velocity dispersion" (AGVD) when $d^2k/d\omega^2 > 0$ and $dk^2/d\omega^2 < 0$, respectively.

1.2 Kerr nonlinearity: XPM and parametric interaction

In the presence of fields at different frequencies the Kerr nonlinearity may lead to a strong interaction resulting in strong inter-pulse phase effects and frequency conversion. The former is referred to as Cross-Phase-Modulation (XPM) and the latter as Four-Wave-Mixing (FWM).

1.2.1 Cross Phase Modulation

We may start by separating the field into a strong and into a weak part. This will allow us to linearize the problem and is appropriate for describing the case in which the input field is composed of a strong field that excites the nonlinearity and by a weaker signal. The total field can then be written as $A = A_P + A_S$, where P stands for the strong pump and the S stands for the weak seed. Substituting this into Eq.1.16 and neglecting terms in the weak field beyond the linear term, we find two equations, one for the pump and one for the weak field

$$j\frac{\partial A_P}{\partial z} + \frac{1}{2k_0}\nabla_\perp^2 A_P - \frac{k''}{2}\frac{\partial^2 A_P}{\partial \tau^2} + k_0\frac{n_2}{n_0}[|A_P|^2 A_P] = 0, \tag{1.19}$$

$$j\frac{\partial A_S}{\partial z} + \frac{1}{2k_0}\nabla_\perp^2 A_S - \frac{k''}{2}\frac{\partial^2 A_S}{\partial \tau^2} + k_0\frac{n_2}{n_0}[2|A_P|^2 A_S] = 0. \tag{1.20}$$

The first equation describes self-phase modulation on the strong pump and we have already seen this, but the second equation is new: it describes what is known as cross-phase modulation (XPM). The strong pump induces a nonlinear phase shift on the weak field and, interestingly, this phase shift is twice as large as that self-induced on the pump. XPM may occur for example between two waves with different frequencies or between waves with the same frequency but different polarizations. An important consequence of XPM is the possibility to observe modulation instability even in the normal dispersion regime.

1.2.2 Modulation instability

Instabilities may occur in many types of nonlinear physical systems such as plasma physics, fluid mechanics and nonlinear optics. Generally speaking, optical instabilities can be classified as temporal or spatial depending on whether light is modulated spatially of temporally after its passage through the nonlinear medium. In one-dimensional systems such as optical fibers, the temporal instability is a well-known effect that occurs through the interplay between self-phase modulation and group velocity dispersion. When light propagates through a medium with a self-focusing nonlinearity and anomalous dispersion the instability manifests itself as a breakup of a continuous

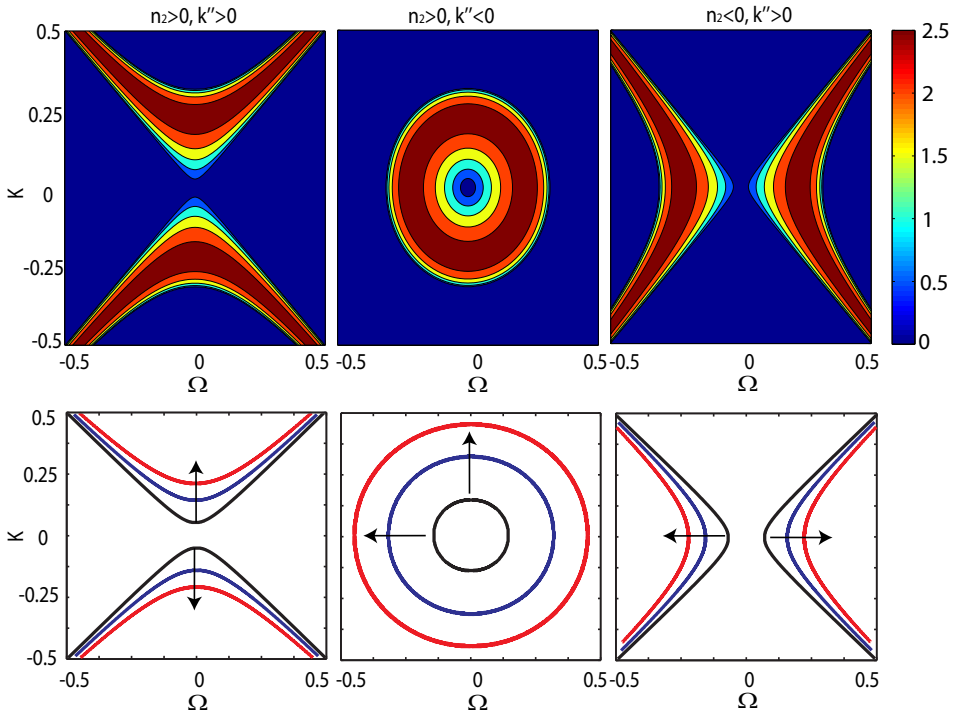

Fig. 1.3. Top row: numerically calculated modulation instability gain profiles for the three cases indicated. The fourth case, $n_2 < 0$, $k'' < 0$, is stable and does not present an instability growth. All axes are in arbitrary units. The bottom row shows the maximum gain curves for each case. Each graph shows three curves corresponding to three different values of the input pump intensity I: the arrows indicate the direction in which the curves move with increasing I.

wave (CW) field into a train of ultrashort pulses. The spatial analogue, with diffraction playing the role of anomalous dispersion, of this effect is observed as the formation of a ring pattern on the transverse intensity profile. As we have already pointed out when dispersion and diffraction are present simultaneously it is not possible to factorize the two effects and treat them independently. G. Agrawal and his colleagues worked this problem out and studied the modulation instability in this case. Details may be found in their paper ([3]): the starting point is the NLSE, Eq.1.16. The origin of the spatiotemporal instability is understood by considering the case of a CW plane wave. Such a wave remains unchanged during propagation in the nonlinear medium with the exception of an intensity-dependent phase shift. The stability of this steady state solution depends on whether small perturbations

grow or decay with propagation. By using a standard linear stability analysis, i.e. by assuming that the electric field amplitude $\sqrt{I}$ is perturbed by a quantity $a = a(x, y, z, t)$ so that $A = (\sqrt{I} + a)\exp(j\gamma z)$ with $\gamma = (k_0/n_0)n_2 I$ and substituting into Eq.1.16 we obtain a differential equation for a. Assuming a general plane wave solution for a, a nontrivial solution is found to exist only if

$$4k_0^2 k_z^2 = (k_x^2 + k_y^2 - k_0 k_0'' \Omega^2)(k_x^2 + k_y^2 - k_0 k_0'' \Omega^2 - 4\gamma k_0), \tag{1.21}$$

where $\Omega = \omega - \omega_0$. If we take $k_x = 0$ and $k_y = 0$, this dispersion relation is identical to that found for optical fibers. The steady state solution becomes unstable whenever the longitudinal wave-vector k_z has a negative imaginary part since the perturbation will then grow exponentially with a gain given by $g = 2\Im(k_z)$. Lets look at the top row of graphs in Fig.1.3. We have graphed the gain as a function of the transverse k-vector $K_\perp = \sqrt{k_x^2 + k_y^2}$ and Ω for three different cases: (i) $n_2 > 0$, $k'' > 0$, (ii) $n_2 > 0$, $k'' < 0$ and (iii) $n_2 < 0$, $k'' > 0$. The fourth possible case is not shown as for $n_2 < 0$, $k'' < 0$ the input plane wave remains stable and all perturbations decay with propagation. Note in Fig.1.3 how the gain profiles vary from one case to the other, in particular we are interested in self-focusing media: for $k'' > 0$ the instability is unbound in $(K_\perp, \Omega)$ space and has a strong X-shape while for $k'' < 0$ the instability is bound and has an O-shape.

The bottom row in Fig.1.3 shows the maximum gain curves for each case: obviously the same X and O shapes are seen, depending on the signs of k'' and n_2. However we have now included the maximum gain curves for three different values of the plane wave intensity. The arrows in the graphs indicate the directions in which the curves move with increasing intensity. Higher input intensities will lead to instability spectra that are further and further shifted away from the $k_\perp = 0$ and $\Omega = 0$, i.e. the input plane wave. Although it is not shown here but the absolute gain value also increases with increasing input intensity.

One last comment is due regarding the case $n_2 > 0$ and $k'' > 0$. Note how for this case no instability is expected along the $K_\perp = 0$ axis, i.e. in optical fibers or in bulk media along the propagation axis. However Agrawal analyzed the modulation instability of an axial plane wave (or equivalently of a fiber mode) in the particular case in which the instability arises not from one plane wave but rather from two coupled waves [4]. These will be coupled through XPM and the analysis should be performed starting from Eqs.1.19 and 1.20, taking care to include in both equations SPM and XPM terms. Proceeding in the same fashion outlined for the one-beam case it is possible to derive a gain curve in function of the frequency detuning Ω. Therefore cross-phase-modulation may lead to an on-axis modulation instability also in the normal dispersion case. Such a modulation instability

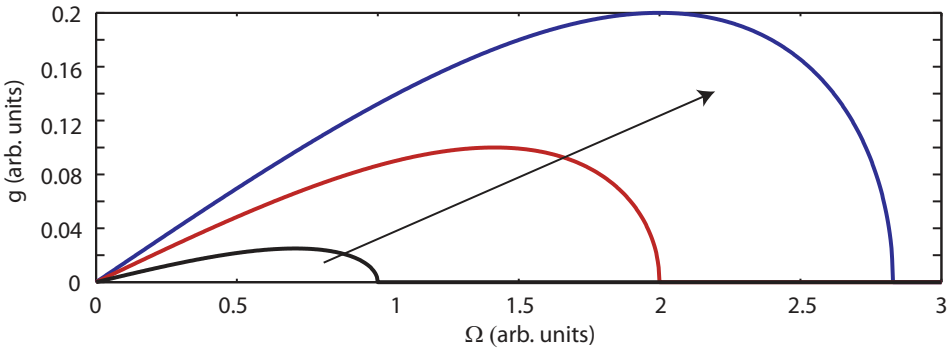

Fig. 1.4. Numerically calculated modulation instability gain along $K_\perp = 0$ in the case of two input beams coupled through XPM. The arrow indicates the direction of increasing input power. As the power increases the maximum gain increases and moves toward larger frequency shifts. Only half of the spectrum is shown as $g(-\Omega) = g(\Omega)$.

has been observed experimentally in optical fibers: we shall see evidence of a similar phenomenum also in the 3D case.

1.2.3 Four Wave Mixing

XPM highlights the effects of the Kerr nonlinearity on a weak field in the presence of a much stronger, intense pump field leading to a modification of the weak field's phase. But it is also possible to observe, under similar working conditions, generation of new frequencies and parametric amplification. Here we will treat the case of Four-Wave-Mixing (FWM), which is exactly what the name says: the Kerr nonlinearity will mix energy between four different fields. This effect may occur in many different combinations so that we speak of degenerate FWM when the four fields have the same frequency (but have different polarizations or propagation directions) or simply of FWM when two or more fields have different frequencies. FWM is commonly described within a context in which the interacting waves are treated as plane waves. Eq.1.1 shows that the nonlinear polarization may be written as $P(E) \propto \chi^{(3)} EEE$, so that if we take

$$E = \frac{1}{2}\sum_{n=1}^{4} E_n \exp(j(k_n z - \omega_n t)) + \text{c.c}, \tag{1.22}$$

the polarization will also be composed of four terms. For example

$$\begin{aligned} P_4 = \frac{3}{4}\chi^{(3)}\{[|E_4|^2 + 2(|E_1|^2 + |E_2|^2 + |E_3|^2)]E_4 + \\ +2E_1E_2E_3\exp(j\Gamma_+) + 2E_1E_2E_3^*\exp(j\Gamma_-) + \cdots\}. \end{aligned} \tag{1.23}$$

A first result of this calculation is the factor 3/4 in front of the nonlinear tensor, which explains the same term introduced in Eq.1.2. This is followed by a term that is formally identical to the nonlinear terms in Eq.1.19 and Eq.1.20 and describes SPM and XPM. Finally we have the terms that describe FWM, where

$$\Gamma_+ = (k_1 + k_2 + k_3 - k_4)z - (\omega_1 + \omega_2 + \omega_3 - \omega_4)t, \tag{1.24}$$

$$\Gamma_- = (k_1 + k_2 - k_3 - k_4)z - (\omega_1 + \omega_2 - \omega_3 - \omega_4)t. \tag{1.25}$$

How many of these terms actually lead to a parametric interaction depends on the relative phase between the field E_4 and the polarization P_4 and this is given by $\Gamma_{+,-}$. Significant FWM will occur only if $\Gamma \sim 0$, a condition that is usually referred to as phase-matching. Further on we will be interested in FWM interactions between 2 degenerate (same frequency) fields two different frequency fields so that the phase matching condition reads

$$\Delta k = 2k_1 - k_3 - k_4 = 0 \tag{1.26}$$

$$\Delta\omega = 2\omega_1 - \omega_3 - \omega_4 = 0. \tag{1.27}$$

The nonlinear polarization may now be introduced into the NLSE, Eq.1.16, and the procedure may be repeated for each polarization term so that we obtain four coupled equations that describe the evolution and parametric interaction of the fields. However this is usually done under a strong approximation: the transverse field evolution is ignored (or treated as constant) and the pulse is treated as a continuous wave. In other words the fields involved in the FWM process are treated as plane monochromatic waves. This is particularly appealing due to the fact that the correspondingly simplified NLSE contains only a z-derivative and the nonlinear polarization term and consequently may be solved analytically.
Such a description is extremely useful and allows us to precisely model the evolution of the four fields and study in detail the parametric interaction between the fields in most cases of interest. However this model may breakdown and induce some confusion if the fields may no longer be modeled in such a fashion. This will be the case in which the interacting pulses have very short durations, or more generally very large frequency bandwidths so that these overlap with each other. The same limitation will exist also if the pulses are very tightly localized so that the spatial k-spectra of the pulses will overlap. So in any situation in which it is not possible to separate the pulses and treat them as distinct plane monochromatic waves even qualitative reasoning with such a model must be treated with great care as it may lead to erroneous conclusions.
Let us return to the phase-matching relations given in Eqs.1.26 and 1.27. We shall refer to these relations as the “linear” phase-matching conditions

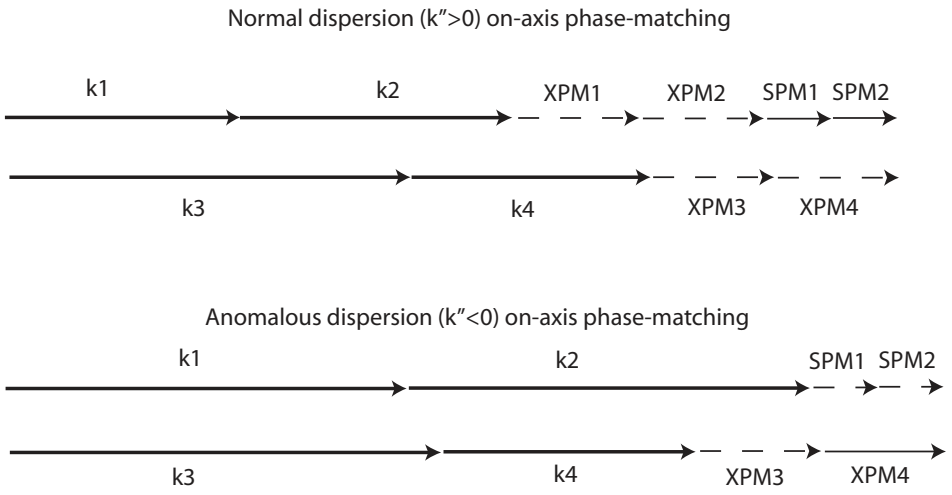

Fig. 1.5. Wave-vectors participating the phase-matched FWM processes that lead to MI in normal dispersion (top scheme) and in anomalous dispersion (bottom scheme). In both cases phase-matching between on-axis wave-vectors is due to the nonlinear corrections to the linear wave-vectors (k1, k2, k3 and k4) arising from SPM and XPM. The dashed wave-vectors correspond to terms that cancel each other out and may thus be negelcted in calculating the phase-matching relations.

and indeed, they only account for the linear, intensity-independent, phase terms of the interacting waves. However we have seen that if the intensities are high enough then we may have an additional intensity-dependent phase term due to SPM and, if degeneracy is broken (e.g. due to waves differing in frequency) also due to XPM. In such cases these terms should be accounted for leading to "nonlinear" phase-matching relations. Actually, if we look again at Fig.1.4 we may wonder what are the physics lying behind the intensity dependent gain profile. Indeed MI may be interpreted as a FWM process in which two photons from the pump waves mix with two other frequencies, one upshifted and the other downshifted. Lets look into this in more detail and consider the situation of self focusing nonlinearity and only the axial photons, i.e. the instability along $k_\perp = 0$. This renders things a bit simpler without losing physical meaning: optical fibers and channel waveguides are typical systems that would be described by such an approach.

Only two cases show an instability, that is in anomalous group velocity dispersion or normal group velocity dispersion (in the presence of two pump waves). In anomalous dispersion it is often quoted, following Agrawal's approach [5], that modulation instability may be interpreted in the frequency domain as a phase-matched FWM interaction in which phase-matching is

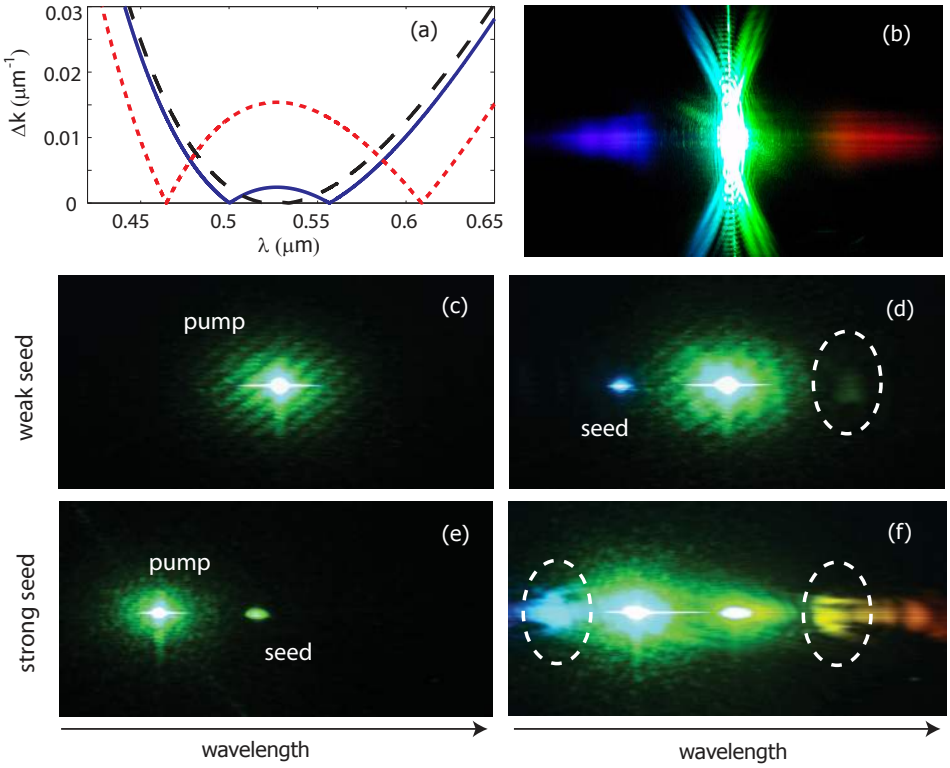

Fig. 1.6. Examples of FWM in fused silica with high intensity laser pulses centered around 527 nm. (a) Calculated Δk versus signal/idler wavelength. The dashed curve gives the linear Δk. The solid curve describes the Δk corrected for XPM assuming that the pump has split into two pulses separated by 1 nm in wavelength and both with equal intensity, $I = 0.3$ TW/cm^2. The dotted line is the same as the solid line but for $I = 2$ TW/cm^2. (b) Spontaneous appearance of blue and red-shifted axial components due to FWM. The central pump has undergone strong reshaping due to filamentation. (c)-(f): seeded FWM experiments. (c) shows the 527 nm pump close to the filament nonlinear focus without any seed. (d) In presence of a temporally overlapped seed at 500 nm a weak signal appears at 557 nm due to FWM. (e) The 527 nm pump and a relatively strong 550 nm seed and both present but are not temporally overlapped so no interaction occurs. (f) The pump and seed are now overlapped, FWM occurs with such efficiency that cascaded frequency conversion occurs. Newly generated frequencies are outlined with dashed ellipses.

enabled thanks to SPM on the pump wave. We have reproduced this reasoning in Fig.1.5. The drawings show the pump wave-vectors, k_1 and k_2, and

the signal and idler wave-vectors, k_3 and k_4. In anomalous dispersion we have $\Delta k = 2k_1 - k_3 - k_4 > 0$. However if we account also for SPM, that will lengthen the pump wave-vectors by a quantity $\delta k = n_2 k_0 I$, and for XPM, that will lengthen the seed wave-vectors by a quantity $2\delta k = 2n_2 k_0 I$, then we end up with the situation shown in the bottom part of Fig.1.5. The dashed terms will cancel each other out in the calculation of the total Δk so that, for a certain value of the intensity I we will find $\Delta k = 2k_1 + 2\delta k - k_3 - k_4 = 0$. Altough both XPM and SPM need to be accounted for, this is equivalent to stating that SPM enables phase-matching and thus the growth of instabilities at well defined frequencies $\omega_{3,4} = ck_{3,4}n_{3,4}$. It is also clear that different values of I will phase-match different frequencies thus explaining the increase in the maximum gain frequency with intensity, shown in Fig.1.3. We may now consider the case of normal dispersion: $\Delta k = 2k_1 - k_3 - k_4 < 0$. Adding SPM and XPM terms will not lead to phase-matching. However if we break the degeneracy of the two pump beams and suppose that they have different frequencies then we must start from $\Delta k = k_1 + k_2 - k_3 - k_4 < 0$, and now we must account for XPM also between the two pumps. This leads to the picture shown in Fig.1.5 for normal dispersion. Once again, the dashed vectors will cancel out and we are left with a single XPM term so that $\Delta k = k_1 + k_2 + 2\delta k - k_3 - k_4 = 0$. This explains XPM-induced phase-matching in normal dispersion and the dependence of the gain profile on intensity (Fig.1.4).

As an experimental example of XPM-induded phase-matching we show in Fig.1.6 three different examples in which on axis FWM occurs the normal group velocity regime. The experiments were carried out in fused silica with an input pump wavelength of 527 nm, i.e. in the normal group velocity dispersion regime, and the pump intensity was just above the self-focusing threshold so that during the propagation the pulse contracts and reaches a minimum diameter. Close to this nonlinear focus, high intensities in the TW/cm^2 range are reached. The dashed line in Fig.1.6(a) shows the calculated linear phase-mismatch Δk for varying signal and idler wavelengths. The pump is assumed to have split by 1 nm wavelength due to the spatio-temporal self-focusing process that may lead to pulse splitting close to the onset of filamentation. $\Delta k \sim 0$ close to the pump but quickly increases due to material dispersion. The dotted line gives the Δk accounting also for XPM assuming an equal peak intensity in both pump pulses, $I = 3$ TW/cm^2. $\Delta k = 0$ for signal/idler wavelengths of 460 nm and 640 nm. Experimentally we observed spontaneous amplification at these wavelengths just after the nonlinear focus, as shown in Fig.1.6(b). The image shows the (θ, λ) spectrum altough here we are interested on the wavelength features of the spectra. Indeed the pump has undergone a strong spatio-temporal transformation but the on-axis signal and idler wavelengths are clearly visible. The remaining

images show the recorded spectra in the presence of an additional weak seed signal. A weak FWM signal is measured (highlighted by a dashed ellipse in Fig.1.6(d)). If the seed energy is increased we start to observe cascaded FWM frequency generation (Fig.1.6(f)). These phase-matched FWM interactions may be explained very well by accounting for XPM with split pumps that have equal intensities, $I = 0.3$ TW/cm^2 (solid line in Fig.1.6(a)).

1.3 Stimulated Raman Scattering

So far we have considered the effect of "instantaneous" nonlinearities. These are instantaneous in the sense that they are due to electric dipole excitations and these occur on a time scale shorter than 1 fs. So, if compared to the few fs oscillation time of an optical pulse we may safely neglect any effect due to long build-up or decay times. But this is not always the case. Stimulated Raman Scattering (SRS) provides a good example of a nonlinearity that is characterized by a non-instantaneous response time and that therefore will typically have a very different impact on the optical pulse evolution depending on the pulse's duration.

The physical origin of the delay in the SRS nonlinear response may be connected to the specific material energy levels that are involved. SRS does not find its origin in the electronic dipole oscillations but rather in the excitation of the rotational/vibrational levels of the molecules that compose the material. These have much longer response times if compared to electron oscillations due to the larger inertia of the molecules. Therefore SRS is most efficient for relatively long pulses, e.g. with temporal durations greater than 10 ps, but this too depends on the specific material and the molecules from which it is composed. SRS may be viewed as a transfer of energy from the pump pulse frequency ω_P to the so-called Stokes frequency ω_S. The frequency shift $\Delta\omega = \omega_P - \omega_S$, the bandwidth and the signal gain at the Stokes frequency are determined by the specific excited molecule level or levels. Generally speaking an organized, regular crystalline material, such as silicon, will exhibit a large Raman gain within a small bandwidth (due to the fact that all the molecular transitions are similar) whereas an amorphous material, such as glass, will exhibit a lower Raman gain albeit with a much larger bandwidth (due to the larger number of possible molecule configurations and thus the broader energy-level distribution).

SRS manifests itself in dispersive media as a signal build-up with gain at the Stokes frequency. If we compare this to the case of FWM one may note that SRS behaves as if it were a spontaneously phase-matched process. This is due to the active participation of the medium in the frequency conversion process or, in other words, due to the fact that the molecular levels are distributed in highly populated and widely spread energy/momentum states

so that phase-matching is always guaranteed. However it is also possible to observe Four Wave Mixing mediated by the Raman nonlinearity. This will only occur under similar conditions to those necessary for FWM mediated by the Kerr nonlinearity, that is phase-matching between the pump, Stokes and anti-Stokes ($\omega_{AS} = \omega_P + \Delta\omega$) frequencies. In such a situation the exponential gain at the Stokes frequency will be substituted by a parametric oscillation between the Stokes and anti-Stokes signals that is mediated by the Raman nonlinearity (and not by the Kerr nonlinearity).
Let us now return to the influence of the pulse duration. For pulses that are shorter than the SRS build-up time, we may outline two different regimes:

i) transient SRS if the pulse spectrum is smaller than the Raman frequency shift ν_S but larger than the Raman gain linewidth $\Delta\nu_S$,
ii) seeded SRS if the pulse spectrum is larger than ν_S.

SRS in these two regimes is usually much less efficient with respect to the stationary regime (i.e. with long pulses). A further issue that must not be neglected when treating the formation of the Stokes pulse is the role of the Group Velocity Mismatch (GVM). GVM arises due to material dispersion and more precisely to the fact that the group velocity of an optical pulse is given by $(dk/d\omega)^{-1}$ so that if $k = k(\omega)$ the group velocities at different frequencies will in general be different. This will lead to a temporal splitting of the pump and Stokes pulses which in turn will strongly reduce the SRS gain experienced by the Stokes wavelength. In fact in most cases this is the greatest limitation for SRS with ultrashort pulses.
The role of SRS in optical filament formation and propagation has been studied extensively but only in the regime of relatively long input pulses, e.g. from 1 ns down to 100 ps. For such pulse durations SRS may be treated as in the stationary regime for practically all materials. Vastly different is the case of ultrashort laser pulses. It is known that SRS may play an important role in soliton formation if the interacting wavelengths are chosen near the zero-dispersion and Raman-solitons, i.e. solitons at the Raman wavelength, may form. This is due to the fact that near the zero-dispersion wavelength the GVM splitting length may be very large. However from what said above, in the normal dispersion regime, or far into the anomalous dispersion regime, we should generally expect ultrashort pulse to remain insensitive to SRS

1.4 Optical Filaments

In the early 60's Chiao et al. predicted that a high intensity laser beam under the action of self-focusing may take on what is now referred to as the Townes profile and thus propagate without spreading [6]. The basic reasoning is that for a specific critical power the lensing effect will perfectly

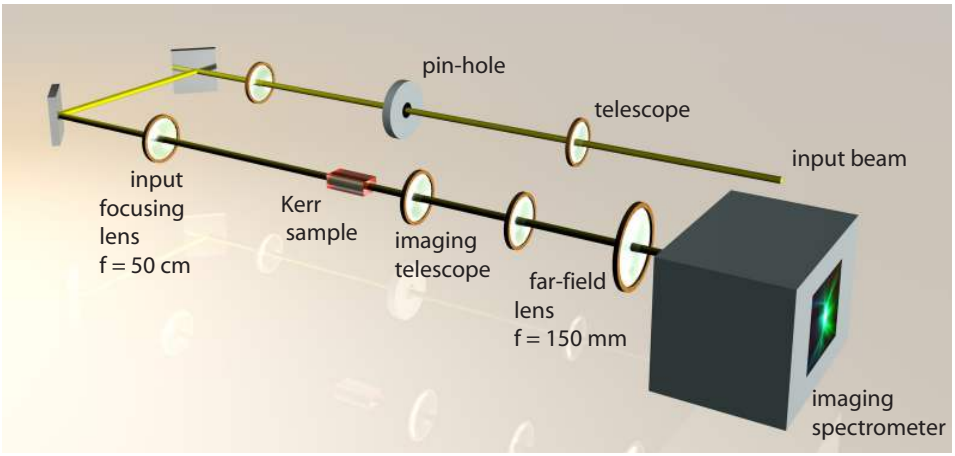

Fig. 1.7. Example of experimental layout used for observing filamentation in condensed Kerr media (e.g. water or glass). The input beam is spatially filtered (telescope + pinhole) and is then focused into the Kerr medium with an $f = 50$ cm lens. The ouptut filament is collected with a telescope and the spatial far-field is then obtained in the focal plane of an $f = 150$ cm lens. The imaging spectrometer (illustrated in more detail in Fig.3.6) reproduces the (θ, λ) spectrum. All numbers given here are purely as an example and have been tested to give good results with an input beam that has a duration of 1.2-0.2 ps, central wavelength 400-1100 nm, energy 1-10 μJ and condensed Kerr media such as liquids (ethanol, water, acetone etc.) or solids (fused silica, BK7 glass, Lithium Triborate crystal, transparent polymers etc.).

balance diffraction. This finding was also corroborated by experimental observation of filamentary damage tracks in glass samples, tracks that were clearly somehow defying diffraction [7].

This first simple theory laid the foundations for future investigations with filaments. Shortly after, Lallemand et al. [8] showed a connection between SF, filament formation and a reduction in the Stimulated Raman Scattering threshold triggering a strong interest in optical filaments that is possibly even stronger now than ever.

So, what is a filament? Curiously there is not a clear-cut definition of an optical filament and one usually refers to the associated phenomena in order to define it. For example, in many experiments using infrared lasers in gases the filament is defined as a high-intensity peak propagating over many Rayleigh ranges without diffracting. The filament length is defined as the distance over which nitrogen fluorescence (excited by multiphoton absorption from the high intensity peak) appears. In solids or liquids a much more obvious manifestation of filament formation is the generation of colored conical

emission (i.e. a broad spectral broadening with different wavelengths emitted at different angles) and strong super-continuum emission. These too are a manifestation of the tightly focused high intensity peak propagating over many Rayleigh ranges. A modern definition of the filament would depart somewhat from Chiao's original idea of the optical pulse creating it's own self-sustained waveguide and could be formulated as [9]:

a filament is a **dynamic** *optical pulse structure with an intense core that is able to propagate over extended distances much larger than the typical diffraction length while keeping a narrow beam size without the help of any external guiding mechanism*

Note the highlighted "dynamic". It is generally acknowledged that the filament is not the result of the propagation of a stationary soliton-like structure. Chiao et al. showed that the nonlinear Schrödinger equation has a stationary solution, usually referred to as the Townes profile. This is just the mathematical formulation of the idea expressed earlier on based on the balance between SF and diffraction. However it is now known that the Townes profile is not stable. Any small perturbation from the critical power will lead either to collapse or to diffraction. Clearly, although the Townes profile may be a good candidate as an attractor for the initial self-focusing dynamics, it is unlikely to be sustained in any way over long propagation distances. We are not particularly interested in the case in which the Townes profile evolves toward a diffracting beam. Rather the question arises as to what limits an unphysical catastrophic collapse of the self-focusing beam. There are many possible limiting mechanisms that will lead either to a forced defocusing of the pulse or to strong (nonlinear) losses that will affect the high intensity collapsing peak. These may be

- nonlinearity saturation [10]: a higher order nonlinearity of opposite sign to the SF Kerr nonlinearity
- self-generated plasma defocusing [11]: extremely high intensities will lead to multiphoton ionization in the medium. The generated electrons will lower the medium effective index and thus give rise to a defocusing effect
- nonlinear losses [12]: the imaginary part of the nonlinearity will induce multiphoton absorption. This depends directly on the pulse intensity and will thus influence the high intensity regions that are self-focusing
- Stimulated Raman Scattering (SRS): it is a possible energy dissipation mechanism proportional to the pulse peak intensity and that may therefore limit SF
- group velocity dispersion, GVD [13]: it is well known that GVD will promote pulse-splitting in time [14]. Although this will not saturate SF

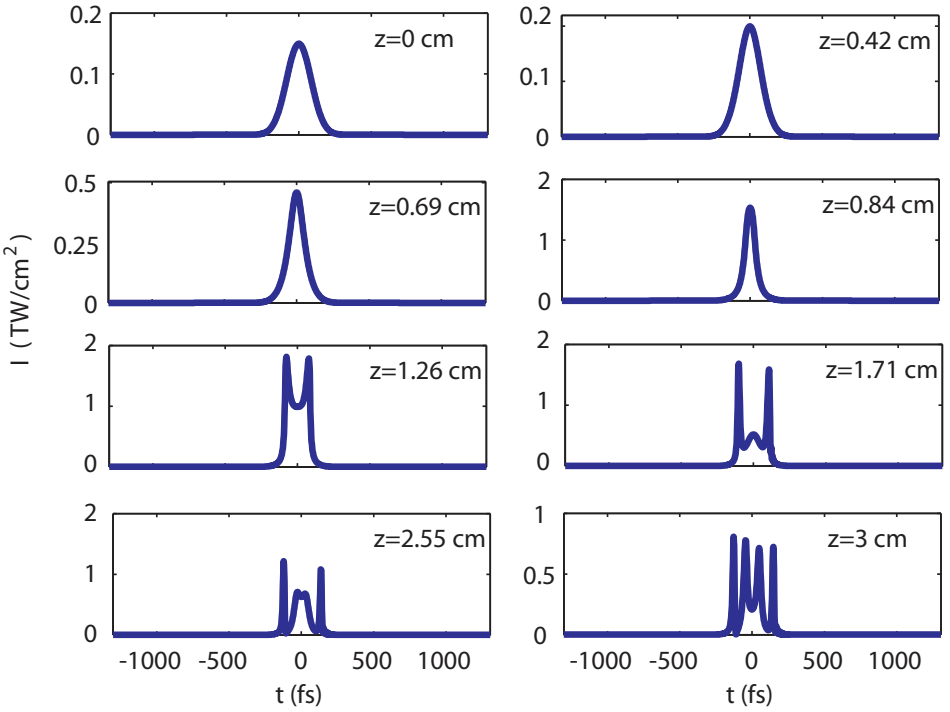

Fig. 1.8. Numerically calculated evolution of the temporal on-axis profile of a pulse propagating in the presence of a SF Kerr nonlinearity. The saturating mechanism is NLL. Initial space-time focusing leads to a pulse compression, followed by pulse splitting as a result of pump depletion due to nonlinear absorption and replenishment of the central peak that finally splits one more time.

it will shift energy dividing it between the two split pulses and therefore increase the power threshold for catastrophic collapse.

In general, depending on the material and pulse central wavelength one of these mechanisms may dominate although in some cases limiting may be due to a combination of these.

We briefly note that although in principle a saturating $\chi^{(5)}$ nonlinearity may actually give rise to a true soliton state, no experimental evidence has been given in this sense. It has also been numerically demonstrated that in real world cases the intensities required for such a soliton formation are actually higher than the thresholds for any of the other listed nonlinearities, so these will step in at an earlier stage effectively acting as the true limiting mechanism [15].

We may conclude by stating that the filament will therefore appear as a

dynamic competition between self-focusing and some saturating or defocusing mechanism. This may eventually involve successive focusing-defocusing cycles that may give the overall impression of a stationary-like propagation but it is actually far more complex.

1.5 Physical phenomena associated to filamentation

We have already pointed out that filaments are characterized by a strong self-focusing that is then followed by the formation of a high intensity peak that propagates over a long distance. However filamentation may manifest itself in many different ways. The interesting point is that these features appear to be common to all media, input pulse wavelengths and durations (within the ultrashort pulse regime).

- position of the nonlinear focus: a linearly propagating beam that has passed through a lens will focus at a certain distance that is determined by the lens focal distance and by the beam diameter at the lens. A collimated beam will not focus at all. Spatial self-action leads to a focusing distance even for a collimated beam and with a lens the nonlinear focus is shifted nearer to the lens with respect to the linear case (see Fig.1.2). In order for this to occur the beam should have a power that is larger than a critical power defined as [16]

$$P_{cr} = 3.77\frac{\lambda^2}{8\pi n_0 n_2}. \tag{1.28}$$

  A collimated beam with $P > P_{cr}$ will focus (due to the nonlinearity) at a distance given by [16]

$$f_{NL} = \frac{0.367 Z_R}{\sqrt{[(P_{in}/P_{cr})^{1/2} - 0.852]^2 - 0.0219}}, \tag{1.29}$$

  where Z_R is the beam Rayleigh range. In the case of a beam that has passed through a lens with focal length f the collapse, or nonlinear focus, position may be found as

$$\frac{1}{f_{NL}^L} = \frac{1}{f_{NL}} + \frac{1}{f}. \tag{1.30}$$

- super-continuum (SC) emission: with this term we indicate the generation of an extremely broad-band, coherent emission with a low angular divergence. The continuum may span more than 1 octave.
- conical emission (CE): broadband emission is observed also at angles with respect to the propagation direction. The emission angle increases with the frequency shift with respect to the pump frequency. The nature of CE is the main topic of this work.

- pulse splitting and temporal compression (see Fig.1.8): space-time coupling has already been described as the mechanism leading to pulse-compression in the presence of SF and normal GVD. During filament formation the pulse will split and the daughter pulses will be further temporally compressed. As an example, a 1 ps pump pulse will split into two pulses with durations of the order of 40-50 fs. The energy balance between the two pulses may favor one or the other or a possible strong unbalance may arise due to propagation effects such as absorption of the trailing pulse due to the self-generated plasma from the leading pulse. This can lead to the isolation and survival of a single, temporally compressed, intense pulse. Filamentation may therefore be considered as a potential novel laser pulse compression technique and single cycle durations may be achieved [17].
- intensity clamping: the peak intensity if the input pulse may increase by some orders of magnitude during the filamentation process. The final peak intensity actually reached will depend on the material characteristics. In gaseous media, for which peak intensities of the order of tens of TW/cm^2 have been reported, the main limiting mechanism is related to self-generated plasma defocusing. In solid or liquid media the role of plasma defocusing is usually somewhat reduced, maximum intensities of the order of 1 TW/cm^2 are found and the main limiting mechanisms are related to multiphoton absorption and GVD. In any case it has been shown that in both gaseous ([11, 18, 19]) and condensed media ([20]) the filament will reach a maximum "clamped" intensity level. On the one hand this may help to explain why, for example the maximum blue-shift due to SPM is independent of the pulse energy above a certain critical value but on the other it also poses possible limits for the use of filaments in applications that require high peak intensities such as extreme ultraviolet generation.
- pulse mode self-cleaning: it has been observed that the far-field profile of the conical emission originating form the filament exhibits an extremely high beam quality [21]. This remarkable feature is of great importance for applications. Seeded parametric interactions in air filaments have shown the possibility to obtain efficient wavelength conversion combined with a notable increase in pulse shot-to-shot stability (ascribed to intensity clamping) and beam quality ([22]).
- spatial robustness: the intensity peak associated to the filament is highly localized in space. Typical filament diameters are of the order of 100 μm in air and 10-40 μm in condensed media. However this tightly localized peak is surrounded by a large background that acts as an energy reservoir continuously refueling the central hot core. This feature is at the basis of the filament robustness to spatial perturbations such that filaments may,

for example, survive propagation through scattering media such as fog and clouds ([23]).

All these features render filaments extremely attractive for a number of applications such as waveguide writing in glass-materials, nonlinear frequency conversion, extreme ultraviolet generation, atmospheric lightning protection and many others.

1.6 Filamentation models

The aim of this section is just to give a short overview of the most important models used to describe filamentation of ultrashort pulses. This is by no means meant to be exhaustive but references are given for further reading. Filamentation is a rather robust effect and may occur with pulses of practically any duration. Ultrashort laser pulse sources have become common in research laboratories only in the last twenty-or-so years. Before this filamentation was studied and modeled using much longer (in the 30-1000 ps range) pulses. The physics in the nanosecond (ns) or picosecond (ps) regime may be quite different due, for example, to much higher plasma generation and absorption, lower material damage threshold, temporal modulation instability and pulse breakup. Experiments with ns pulses were described either within the self-guiding model, based on the spontaneous formation of the Townes profile as discussed above, or with the so-called moving focus model. These models were then extended also the femtosecond regime. We shall therefore give a brief description of these, and other models, some of which are still currently used.

1.6.1 The self-guiding model

The self-guiding model originated from the idea that the Townes profile is a stationary state of the nonlinear Schrödinger equation [6]. A spontaneous reshaping of the input Gaussian pulse into the Townes profile could therefore explain the non-diffractive, tightly localized peak observed in filaments. It is also reasonable to expect such a spontaneous reshaping as the Gaussian profile and the Townes profiles are very similar (see Fig.1.9) and it has indeed been experimentally observed [24]. However it is now recognized that although the initial SF dynamics may lead to the formation of the Townes profile, the filament is not simply a propagating Townes wave-packet. The Townes profiles is unstable and will thus "explode" under the effect of small perturbations. One may therefore study the effects of this explosion or, more precisely, study the modulation instability of the Townes profile in order to understand if and how the evolution of the Townes profile may explain

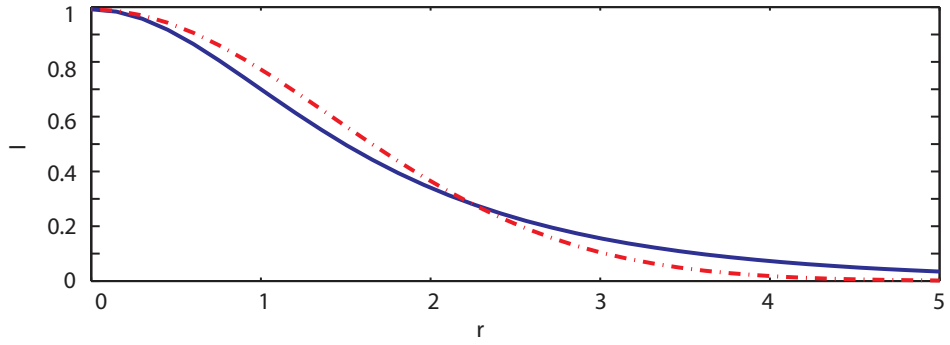

Fig. 1.9. Comparison of the Gaussian (red, dashed line) and the Townes profile (blue, solid line). All units are normalized.

filamentation. This will be topic of one of the following chapters.
Often one may find other terms such as "self-channeling" or "self-trapping". These terms, along with "self-guiding", are not always understood in the same manner in literature. Details, such as the role of the self-generated plasma in the balancing mechanism, may change from one case to the other, but overall it should be intended that these terms indicate simply the absence of any external guiding mechanism ([9]).

1.6.2 The moving focus model

The moving focus model ([25]) starts from the assumption that the laser pulse may be divided into independent time slices and that the effect of collapsed time slices will not influence in any way subsequent propagation. This is true only when physical effects that couple the various time slices together, such as GVD or plasma generation/defocusing, remain weak.
The filament is then formed by the different time slices, each with a different peak power, focusing at different distances, according to Eq.1.29: the central time-slice will have the highest power and will thus determine the position of the nonlinear focus. Time slices further away from the central one will lead to focusing at increasing distances. However it is important to note that this simple model fails in the case of a beam that has passed through a lens as the nonlinear focii of all time slices occur before the linear focus distance. This is in contradiction with experiments and numerical simulations performed with the NLSE. This shortcoming may be explained by noting that coupling between different time slices cannot be neglected. This is true even in air that has very low GVD but also suffers strong self-induced plasma-defocusing effects.

1.6.3 Dynamical spatial replenishment

The self-guiding and moving-focus models do not account for the temporal evolution of the pulse and therefore oversimplifies the full dynamical picture that emerges that was first highlighted in numerical simulations [26]. Self-focusing creates an intense leading peak that will create a defocusing plasma in its wake and will also suffer nonlinear losses. The generated plasma will be strongly reduced so that the beam may shrink once again due to the still active SF. This cycle may repeat itself many times within the same filament thus leading to long-range propagation.

1.6.4 The (extended) nonlinear Schrödinger equation

An equation cannot be considered as a "model" in the sense used above. Nevertheless we shall describe here the extended nonlinear Schrödinger equation (NLSE) as it is the prototype equation that is most widely used to model ultrashort laser pulse filamentation. We use the term "extended" in the sense that the NLSE actually only accounts for diffraction and Kerr nonlinearity. However it may be easily extended so as to include many other effects ranging such as nonlinear losses, plasma generation and plasma-induced absorption, higher-order nonlinear effects, Raman nonlinearity and so on. Details of the actual equation used in the numerical simulations shown in this work may be found elsewhere (see e.g. Refs.[27, 28]) and Chapter 4 is devoted to an in depth description of how to implement a numerical code based on this model.
The nonlinear equation used in simulations may be expressed in terms of the Fourier transformed envelope $\hat{\mathcal{E}}(r,\omega,z) \equiv \mathrm{FT}[\mathcal{E}(r,t,z)]$:

$$2i\hat{K}\partial\hat{\mathcal{E}}/\partial z + [\nabla_\perp^2 + (k^2 - \hat{K}^2)]\hat{\mathcal{E}} = -\mathrm{FT}\{N(\mathcal{E})\}, \tag{1.31}$$

$$N(\mathcal{E}) = k_0(2\frac{k_0 n_2}{n_0}T^2|\mathcal{E}|^2 - \frac{k_0\rho}{n_0^2\rho_c} + iT\beta_K|\mathcal{E}|^{2K-2})\,\mathcal{E}. \tag{1.32}$$

This particular model accounts for diffraction, dispersion *via* the relation $k(\omega) \equiv n(\omega)\omega/c$, Kerr self-focusing ($n_2 = 3.2\cdot 10^{-16}$ cm^2/W in water), multiphoton absorption ($\beta_K = 2\cdot 10^{-60}$ cm^{19}/W^{10}, $K = 10$ in water at a wavelength of $\lambda = 1055$ nm), defocusing by the plasma with density ρ described by $\partial\rho/\partial t = (\beta_K/K\hbar\omega_0)|\mathcal{E}|^{2K}$, space-time focusing and self-steepening *via* the operators $\hat{K} \equiv k_0 + k_0'(\omega-\omega_0)$ and $T \equiv 1+(i/\omega_0)\partial/\partial t$. $\rho_c \equiv (\epsilon_0 m/e^2)\omega_0^2$ denotes the wavelength dependent critical plasma density.
In the next chapters we shall see many examples and situations in which this equation is applied with success and reproduces even at a quantitative level experimental measurements.

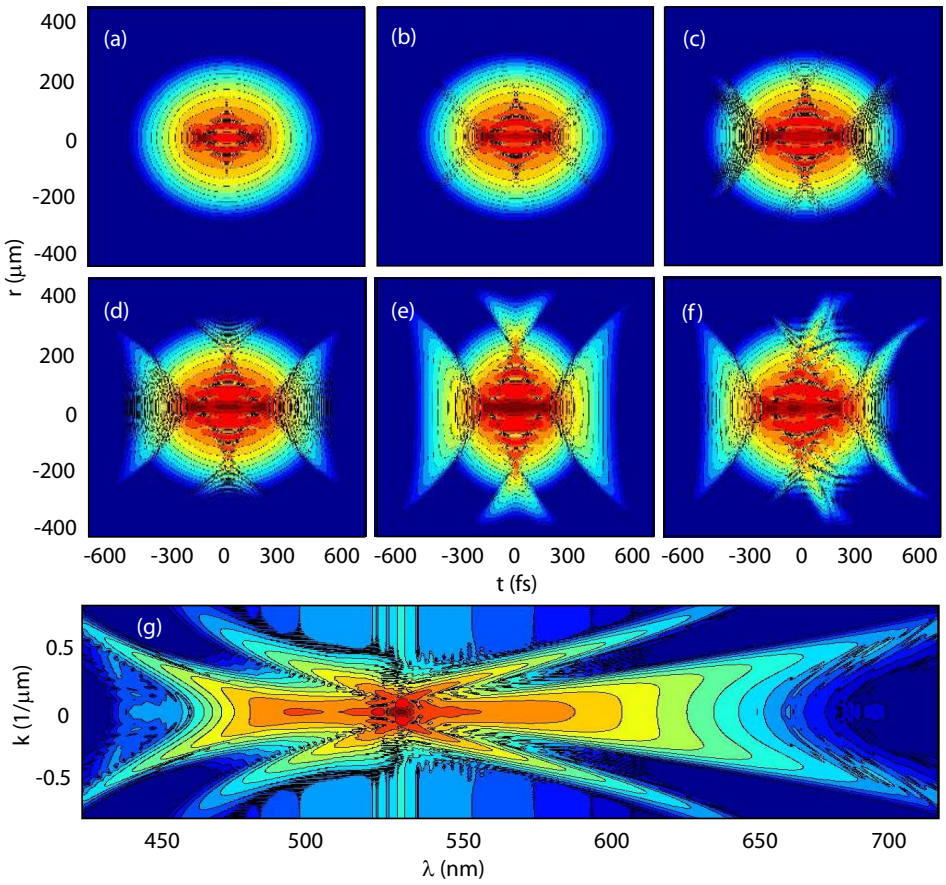

Fig. 1.10. Near-field intensity profile (shown over 6 decades) evolution of a 527 nm, 200 fs laser pulse undergoing filamentation in water at five different distances just after the nonlinear focus at (a) 3 cm, (b) 3.2 cm, (c) 3.4 cm, (d) 3.6 cm, (e) 4 cm. (a) to (e) include only second order dispersion (k") effects. (f) is the same as (e) but the full material dispersion and plasma generation are accounted for. (g) $(k_\perp, \lambda)$ spectrum corresponding to the (r, t) intensity profile shown in (e).

1.6.5 The X wave model

The last years have seen the rapid advance of a new approach to filamentation, what we may call the "X wave" model. This model is based on the interpretation of filamentation in terms of the spontaneous generation and successive dynamical interaction of conical wave-packets. The particularity of conical waves is the energy flux that occurs along a conical surface that leads to stationary propagation, i.e. they are characterized by a central intense peak that propagates without diffraction and without dispersion. As

we shall see the generic conical wave is best studied and described in the Fourier $(k_\perp, \omega)$ domain. The most general form of the conical wave then becomes $k_\perp = \sqrt{k^2 - k_z^2}$ where stationarity is imposed by taking the longitudinal wave-vector k_z to be linear function of frequency,

$$k_z = k_0 + k_0' \Omega. \tag{1.33}$$

X waves, so-called due their evident "X" shape in both the near and the far-field, are a specific example of conical waves that are stationary in the normal group velocity dispersion regime. The spontaneous formation of X waves in the presence of nonlinearity was first demonstrated by P. Di Trapani et al. [29] in a crystal with second order nonlinearity. The same concept of conical waves was later used by Dubietis et al. to explain certain anomalies observed related to the propagation of laser pulse filaments [30, 12]. By placing a pinhole in the path of the filament such that only the very central high-intensity peak was allowed to pass through, Dubietis observed that the filament was effectively killed and further propagation was dominated by strong diffraction. On the other hand, placing a stopper in the filament path so that now only the central spike is blocked, the filament reforms almost immediately after the obstacle and continues propagating as in the unperturbed case. This was interpreted by assuming that the filament is actually a conical wave so that the central intense peak results as an interference effect, continuously refilled by a large yet low-intensity surrounding energy reservoir. Finally, using numerical simulations, Kolesik et al. clearly proved that filamentation in condensed media may be interpreted as a dynamical interaction between X waves that form spontaneously within the filament [31].

The X wave model takes these ideas one step further: the spontaneous evolution of a Gaussian pulse in a Kerr medium is interpreted as a spontaneous reshaping into one or more X waves. All subsequent features of the pulse propagation, e.g. pulse splitting, conical emission and any nonlinear interactions, are intrepreted treating the pulses as X waves. This implies for example that phase and group velocities must be accordingly corrected with respect to those expected for Gaussian pulses or that nonlinear interactions are no longer treated as interactions between plane waves but rather between X waves. We underline that this model does not affirm that X waves (in the sense of truely stationary solutions to the wave propagation equation) are actually formed during the filamentation process. Indeed the tails may appear to decay at a different rate than that expected for the "true" X wave and both measurements and numerics clearly highlight that the filament propagation is a strongly dynamic event that does not seem to show any particular stationary behavior. Rather, the model lies on the assumption that the input pulse will try to evolve toward a final stationary state that

has the form of an X wave and that this feature is so strong that effectively interpreting the dynamics in terms of X waves leads to a deep comprehension of the filamentation process.
In order to justify the assumption at the basis of the X wave model, in Fig.1.10 we show the numerically simulated near field evolution of a 527 nm, 200 fs pump pulse undergoing filamentation in water. The intensity profiles are plotted on a logarithmic scale with over a 6 decade range so as to highlight the weaker X-features. Graphs (a) to (e) show the (r,t) evolution just after the nonlinear focus at distances of 3, 3.2, 3.4, 3.6 and 4 cm. As can be seen pulse splitting has already set in and each split pulse starts to develop weak but very clear X-shaped profiles. These graphs were obtained accounting only for second order material dispersion. Accounting for the full material dispersion and also plasma generation leads to a more complicated (r,t) profile but the X-features are still present. An interesting feature of filamentation is that, although the near fields may be rather difficult to interpret it turns out that the full space-time Fourier transform $(k_\perp,\omega)$ shows clear X wave features with well separated features (see fig.1.10(g)). This will be very important for the ideas described in the following pages.

1.6.6 The Effective Three Wave Mixing model

The Effective Three Wave Mixing (ETWM) model was developed by Kolesik et al. [32, 31, 33]: the idea is based on an interpretation of the nonlinear interaction between the pump wave and the medium as a scattering process in which the intense pump generates a perturbation in the material (a "material" wave) that in turn scatters the pump pulse into the output pulse. This model derives directly from the Unidirectional Optical Pulse Propagation Equation (UPPE) [34] used by Kolesik et al. to simulate ultrashort pulse propagation and filamentation. By describing the material perturbation $\Delta\chi$ as a sum of individual response peaks and writing these as a decomposition into Fourier components the UPPE leads to a relation for the scattered amplitude [33]

$$A_{\text{out}}(z) = \frac{i\omega^2}{2c^2k_z} \times \int dz \sum \Delta\chi(z) A_{\text{in}} \times \exp\left[iz \left(-k_z(\omega, k_x, k_y) + k_z(\Omega, u, v) + \frac{\omega - \Omega}{v_r} \right) \right]. \quad (1.34)$$

The most significant contribution to the output spectral components A_{out} will come from the processes for which the fast oscillating exponential term ~ 1. Approximating the input pulse with a plane monochromatic wave we have the condition

$$\left| -k_z(\omega, k_x, k_y) + k_z(\omega_0, 0, 0) + \frac{\omega - \omega_0}{v_r} \right| = 0. \tag{1.35}$$

This equation may be interpreted as a phase matching condition for the process in which a material wave with frequency $\omega - \omega_0$ scatters an incident optical wave at ω_0 to produce a scattered wave with frequency ω and transverse wave-numbers $k_{x,y}$. The shape of the output spectrum defined by this relation depends on the linear chromatic dispersion parameters of the material an on a single parameter v_r, the group velocity of the material response peak. It is interesting to note that this phase-matching relation is formally identical to Eq.1.33, i.e. to the condition of dispersion-less propagation used to describe stationary conical waves. Therefore the X wave and the ETWM models have some similarities: they both show that filamentation in the normal group velocity dispersion regime is accompanied by a spontaneous formation of X waves and the relations used to fit measured and numerically calculated spectra are identical. However there are also some differences: the ETWM model is derived through a rigorous derivation starting from Maxwell's equations that lead to the UPPE equations and finally to eq.1.35. Furthermore the output spectrum is described as the result of a linear scattering process. The X wave model is based on the assumption that due to the nonlinearity the input pulse will transform with a dynamics that may be explained as the approach toward a stationary state. This is not derived with a mathematical formulation but is rather postulated on the basis of experimental and numerical observations. These two approaches are somehow complementary but we would like to underline that the ETWM model gives no prediction or physical explanation for the specific values observed of the material group velocity. On the other hand the X wave model was developed so as to give a tool useful for investigating the details of the filamentation dynamics, such as pulse splitting and the group velocities of the split pulses.

For an in-depth review of filamentation in all of its aspects we strongly suggest reading Ref.[9]. The next chapters will go through the details of conical waves, followed by a detailed description of the experimental methods used to characterize polychromatic conical waves and finally the main results and applications within the field of ultrashort laser pulse filamentation.

2

Conical waves

Conical waves are a particular class of waves that owe their name to the fact that the energy flux occurs along a conical surface. Their importance is related to the fact that they represent stationary solutions to the wave propagation equation, even in the presence of dispersion. The simplest example of a conical wave is the monochromatic Bessel beam. We shall therefore start our description from here and then extend the analysis to pulses, polychromatic, conical waves. We shall then conclude the chapter by studying the role of nonlinearity.

2.1 Linear conical waves

In 1987 Durnin and co-workers gave the first experimental demonstration that by properly shaping the spatial profile of an optical beam so as to reproduce the Bessel function, it is possible to overcome the natural diffraction of the central localized intensity peak [35]. This discovery was based on the prediction that the Bessel profile is a diffractive-free (stationary) solution to the wave equation $(\nabla^2 - c^{-2}\partial^2/\partial t^2)E = 0$ that governs the propagation of a monochromatic beam. Indeed if we look for a solution to this equation of the form $E(z,t) = A(r)\exp(-j(k_z z - \omega t))$, i.e. with an amplitude that does not depend on the propagation distance z but only on the radial coordinate $r = \sqrt{x^2 + y^2}$ we find

$$\frac{d^2A}{dr^2} + \frac{1}{r}\frac{dA}{dr} + (k^2 - k_z^2)A = 0. \tag{2.1}$$

This equation has the solution

$$A(r) = J_0(k_r r) \qquad \text{with} \quad k^2 = k_z^2 + k_r^2. \tag{2.2}$$

Where J_0 Writing $k_r = k\sin\theta$ and $k_z = k\cos\theta$ and using the integral form of the Bessel function we have

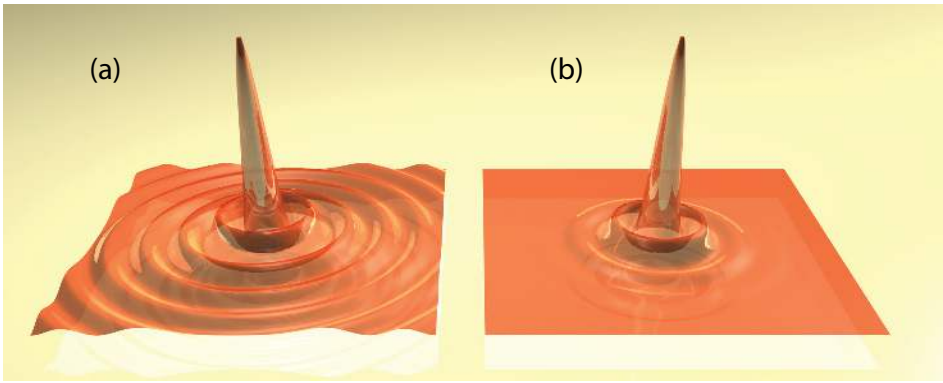

Fig. 2.1. Spatial profiles of the (a) Bessel beam and (b) Bessel-Gauss beam.

$$\begin{aligned} E(z,t) &= J_0(kr\sin\theta)e^{j(kz\cos\theta-\omega t)} \\ &= \frac{1}{2\pi}\int_0^{2\pi} d\phi e^{j(kz\cos\theta-\omega t)} e^{j(kx\sin\theta\cos\phi+ky\sin\theta\sin\phi)} \\ &= \frac{1}{2\pi}\int_0^{2\pi} d\phi e^{j(\boldsymbol{q}\cdot\boldsymbol{r}-\omega t)}, \end{aligned} \tag{2.3}$$

where the vector $\boldsymbol{q} = k(\hat{x}\sin\theta\cos\phi + \hat{y}\sin\theta\sin\phi + \hat{z}\cos\theta)$ intersects the z-axis at an angle θ. The Bessel beam may therefore be viewed as formed by infinite plane waves, all propagating at an angle with respect to the propagation axis and arranged with their k-vectors along a conical surface. These plane waves will overlap along the z-axis and the resulting interference pattern will give rise to a Bessel-modulation of the transverse beam amplitude (see Fig.2.1).

The phase velocity of the Bessel beam is $v_\phi = c/\cos\theta$. We note that this "superluminal" phase velocity is merely a geometrical effect due to the fact that the plane waves are propagating at an angle with respect to the z axis. Indeed the points of contact of the plane waves along the z axis are not causally connected so there is no violation of Einstein causality.

Also note that the ideal non-diffracting wave of the form given in Eq.2.3 must have infinite energy. This is due to the fact that the energy calculated as $\int |E|^2 dr \propto \int |J_0(\alpha r)|^2 dr$ ($\alpha = k\sin\theta$) is not finite. Put in other words, we note that each ring in the Bessel profile contains the same energy as the central spot so an infinite number of rings will lead to an infinite energy. In order to remove the divergence problem the Bessel-Gauss beam has been introduced in accordance also to experimental possibilities [36]. The typical experimental situation is that of an initial Gaussian beam that is reshaped using linear optical elements, into a Bessel-Gauss beam (see Fig.2.1)

$$E(z,r,t) = J_0(\alpha r)e^{(-r^2/\sigma^2)} \cdot e^{[j(kz-\omega t)]}. \tag{2.4}$$

The price to be paid for this apodization is the reappearance of diffraction. The tighter the apodization (small σ) the stronger the diffraction will be. It is possible to give general relation between the non-diffractive ranges of the Bessel-Gauss beam and the Gaussian beam [37]

$$\text{Bessel-Gauss range} \sim N \cdot \text{Gaussian range}, \tag{2.5}$$

where the Gaussian range, usually defined as the Rayleigh range, is $Z_R = \pi w^2/\lambda$ where w is the beam diameter. The extended non-diffractive range of the Bessel-Gauss comes at the expense of higher power request, that is no longer infinite due to the apodization but is given by

$$\text{Bessel-Gauss power} \sim N \cdot \text{Gaussian power}. \tag{2.6}$$

The Bessel range may also be given as a function of the input beam diameter and cone angle [38]:

$$\text{Bessel-Gauss range} \sim \frac{\sigma}{\tan\theta}. \tag{2.7}$$

So, generaly speaking, any beam has a "diffraction-free" distance. The advantage of the Bessel-Gauss beam is that in principle this distance may be made as long as you wish.

2.1.1 Experimental methods for Bessel beams

Experimentally the Bessel-Gauss beam may be generated using holograms or, more efficiently, using axicons (see Fig.2.2). Axicons are particular optical elements similar to lenses with the difference that the input glass surface is flat and the output surface is cone-shaped. Such an optical element will generate a Bessel beam that is apodized with the input beam profile (usually Gaussian). Care must be taken in aligning the axicon with the input beam. A simple trick may help in this case. The far-field pattern of the Bessel beam is a ring: it is a sufficient to let the Bessel-Gauss beam propagate for a certain distance and this ring will become clearly visible. A correct alignment of the axicon is obtained when the far-field ring is uniformly illuminated. Finally care must be taken in assuring that the axicon is also orthogonal to the input beam, for example by checking that the back-reflection from the input surface of the axicon returns along the input beam path. Failure to do this will lead to star-shaped patterns departing from the central peak that may significantly perturb or alter experimental results.
An alternative to the axicon is the so-called lensacon ([39, 40, 41]): this is

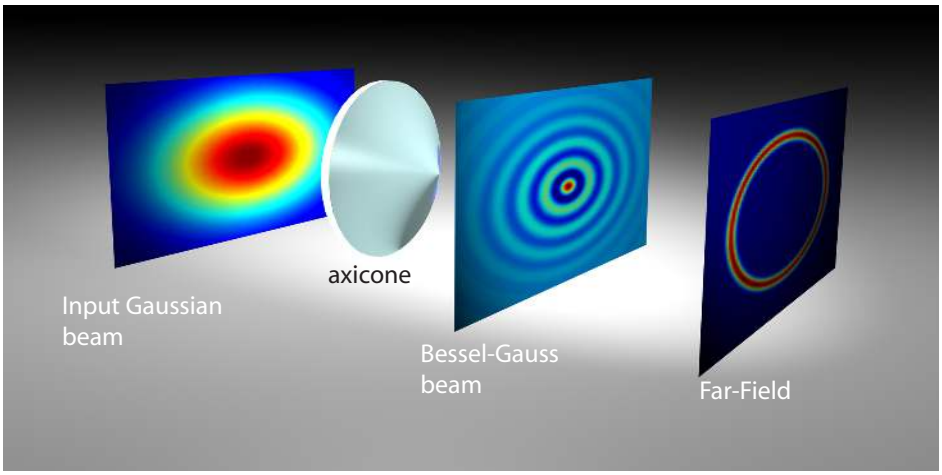

Fig. 2.2. Experimental setup for generating Bessel beams using an axicon. The input Gaussian beam passes through the axicon and at the output we find a Bessel beam, apodized by the input Gaussian profile. Looking at the far-field, or sufficicntly far away from the axicon, we will observe a ring pattern.

formed by a using a ring shaped aperture combined with a focusing lens. In this way the aperture will block most of the beam with exception for those plane waves propagating at a well defined angle with respect to the propagation axis. This layout has the main disadvantage with respect to the axicon that most of the input beam energy is lost (absorbed by the ring-aperture) but has the advantage that it is made of standard and readily available optical components and, most importantly, the Bessel beam angle may be easily varied by simply changing the diameter of the ring aperture. Finally, a common method used to generate Bessel beams is based on holograms, basically circular grating patterns [42]. These may be easily generated using a PC and printing the pattern on a transparency. Advantages and disadvantages with respect to the axicon are similar to those of the lensacon: the holograms are easy and relatively cheap to generate but a lot of the input beam energy is lost in the higher diffraction orders.

2.1.2 Pulsed Bessel Beams

So far we have considered only monochromatic continuous wave (CW) beams but obviously the Bessel Beam generation techniques we have described may be applied to laser pulses. The fluence pattern will not in general show a marked variation with respect to the monochromatic case. However when using pulses the central Bessel peak will now be a peak not only in space

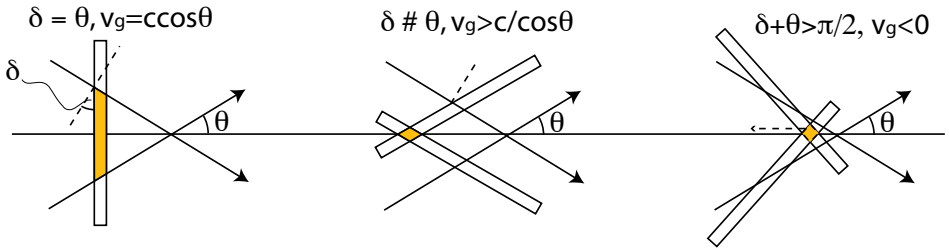

Fig. 2.3. Various configurations for the Bessel Beam: different pulse-front tilt angles will lead to different group velocities, In general the group velocity may be subluminal, superluminal or even negative.

but also in time and it is therefore important to know the velocity at which this peak is traveling along the propagation direction.
We have already pointed out that the phase velocity is given by $v_\phi = \omega/k = c/\cos\theta$. We define the group velocity v_g of a Bessel pulse as $v_g = d\omega/dk$ where $k = k_0 \cos\theta$. The group velocity of a Bessel pulse in vacuum is given by [43]

$$v_g = \frac{c}{\cos\theta[1 - (\omega\partial\theta/\partial\omega)\tan\theta]}, \tag{2.8}$$

where the term $\omega\partial\theta/\partial\omega$ is related to the pulse front tilt. The pulse front is defined as the surface coinciding with the peak intensity and, due to angular dispersion this may be tilted with respect to the phase front. A common example of a tilted pulse front is that resulting from reflection of a polychromatic pulse from a grating as shown in Fig.3.13. The angle between the pulse and phase front, the tilt angle, δ, is given by

$$\tan\delta = \frac{\omega\partial\theta}{\partial\omega}. \tag{2.9}$$

Therefore the group velocity may be written as

$$v_g = \frac{c\cos\delta}{\cos(\theta \pm \delta)}. \tag{2.10}$$

The sign in the denominator is determined by the sign of the angular dispersion. In other words, the angular pulse front tilt will strongly influence the pulse group velocity which may be subluminal, superluminal or even negative [43, 44]. In turn, the pulse front tilt is determined by how we generate the Bessel pulse. In particular, if we use a hologram and take the forward transmitted zero-order peak the pulse front will remain parallel to the input pulse front while the phase fronts will be bent at an angle θ with respect to the propagation axis. In other words the the angular dispersion is negative with the tilt angle is equal to the cone angle. As a result, the group

velocity of the Bessel pulse is smaller than the speed of light (subluminal): $v_g = c\cos\theta$. On the other hand, for a refractive axicon with a wedge angle γ and refractive index n the cone angle of the Bessel beam is determined by Snell's law, $n\sin\gamma = \sin(\gamma+\theta)$, and the angular dispersion is given by $\partial\theta/\partial\omega = (\partial n/\partial\omega)\sin\gamma/\cos(\gamma+\theta)$ [43]. If the material dispersion is normal then the angular dispersion is positive and pulse front tilt results in a superluminal Bessel pulse, $v_g > c/\cos(\theta)$. Superluminal propagation of the Bessel peak has been clearly demonstrated in two different experiments: in one, by measuring the plasma trail induced by the pulse [45] and in the other by an ingenious interference technique [46]. This last example is particularly interesting: the Bessel pulse generated in this case is actually what is called a Bessel-X pulse due to the fact that the spatio-temporal profile of the pulse is X shaped. With long pulses this X shape is not apparent but was very clear in the white-light experiment (with a roughly 10 fs coherence time). Finally, if we take the positive sign in Eq.2.10 and δ large enough, i.e. a very large pulse front tilt, so that $\cos\delta > 0$ but $\cos(\theta+\delta) < 0$ then the group velocity of the Bessel peak will be negative implying that we will observe the peak forming at the leading edge of the overall temporal energy profile and that this will shift toward the trailing edge as the overall pulse energy propagates forward [47].

2.1.3 Polychromatic conical waves: X, O and "Fish" waves

At this point the interesting question is if the Bessel beam may be generalized to the polychromatic case, i.e. to optical pulses, in such a way that not only spatial spreading (diffraction) but also temporal spreading (dispersion) is eliminated. The quest for such a wave-packet, often referred to as a "light-bullet", has attracted much interest for a number reasons related both to fundamental physics and to applications. The first and most popular candidate for the light bullet was originally thought to be the 3-dimensional optical soliton. The 3D soliton would result from the balance between nonlinear spatio-temporal nonlinear phase shift and diffraction and dispersion. However, if realistic conditions are imposed in the numerical calculations, accounting also for nonlinear losses, it turns out that there are no trivial materials or conditions for which the soliton may actually form [48]. On the other hand polychromatic conical waves, at the price of being weakly localized, may indeed be stationary and counteract both diffraction and dispersion, and all this without requiring any particular nonlinear interaction. Actually the first polychromatic conical waves were not discovered in optics but in acoustics. Clearly the Durnin 1987 paper on Bessel beams does not refer solely to light waves but to any kind of propagating waves. J. Lu, a postdoc at the Mayo Clinic in Rochester, Minnesota recognized in Durnin's nonspreading Bessel beam the potential for extending the focal depth of ul-

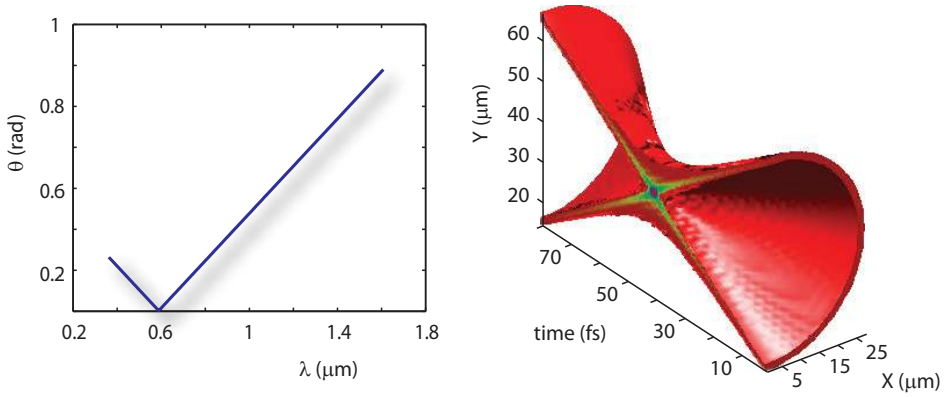

Fig. 2.4. X wave (θ, λ) relation and volume plot of the resulting X wave calculated from Eq.2.11. The volume plot is cut in half so as to highlight the internal intensity distribution.

trasound imaging [49]. Ultrasound images, like radar maps of approaching aircraft, are formed by sweeping a pulsed beam through the region of interest. Lu, together with Greenleaf, found a way to create short pulses from the superposition of Bessel beams of different frequencies [50]. Because of their distinctive profiles, Lu and Greenleaf named the pulses X waves (see Fig.2.4).

The X wave may be obtained by writing the electric field as a linear superposition of monochromatic Bessel beams

$$E(r,z,t) = \int_{-\infty}^{\infty} S(\omega) J_0(k_\perp r) \exp[j(k_z z - \omega t)] d\omega, \tag{2.11}$$

where the transverse wave-number is $k_\perp = k \sin\theta = \omega/c \sin\theta$ and is determined by the Bessel cone angle θ and

$$k_\perp = \sqrt{k^2(\omega) - k_z^2}. \tag{2.12}$$

The longitudinal wave number $k_z = k\cos\theta$ must be a linear function of ω in order for the pulse to be stationary, i.e. $k_z = \omega/v_z^\phi$. We find that the longitudinal phase velocity $v_z^\phi = (\omega/k)(1/\cos\theta) = c/\cos\theta > c$ and the longitudinal group velocity $v_z^\phi = v_z^g > c$ so the X wave has both phase and group velocities that are superluminal.

In Fig.2.4 we show the X wave (θ, λ) relation and the relative X wave profile[1]. The X-shaped profile is clearly visible in the volume plot that has been

[1] Note that the (θ, λ) space is analogous to the $(k_\perp, \omega)$ space. However we shall preferably refer to the former as this corresponds to the space in which experiments are performed.

cut in half so as to highlight the internal intensity distribution.
Lu and Greenleaf's superposition scheme, works because the chromatic dispersion of ultrasound in water is negligible. That's not the case for light in most condensed media so that the optical pulse will actually spread in time. In 1997, Sönajalg and co-workers of the University of Tartu in Estonia figured out how to counter chromatic dispersion and create optical X wave pulses that do not spread in time [51]. Their setup included a holographic element, the "lensacon", which distributes the frequency components of an X-shaped pulse about different, adjustable cone angles. Indeed, dispersion causes standard pulses to spread due to the different way in which phases are accumulated at different frequencies. However we may take the transverse wave number so that $k_\perp = (\omega/c)n(\omega)\sin\theta(\omega)$: if the relation $\theta(\omega)$ is chosen correctly it may compensate the effect of the dispersion term $n(\omega)$ and the pulse will be stationary. In other words, in dispersive media the X wave may remain stationary due to a mutual compensation of diffractive and dispersive phase shifts. This condition may be expressed as a two parameter function [52, 53]

$$k_z(\omega) = k(\omega)\cos\theta = [k(\omega_0) - \beta] + (k_0' - \alpha)(\omega - \omega_0), \tag{2.13}$$

where α and β are two arbitrary parameters, $k_0' = (dk/d\omega)|_{\omega_0}$ and $\omega_0 = 2\pi cn(\lambda_0)/\lambda_0$ with λ_0 the central wavelength at which the relation is calculated. The cone angles θ may be chosen for each frequency so as to satisfy this relation and the group velocity along the propagation z direction, $v_z^g = (dk_z/d\omega)^{-1}$, will be constant and all dispersive effects are removed. The stationary polychromatic wave is often described as an "envelope X wave", i.e. rather than describing the full electric field E the field amplitude A is given by

$$A(r, z, t) = \int_{-\infty}^{\infty} S(\Omega) J_0[k_\perp(\Omega) r] \exp[j\Omega t] d\omega, \tag{2.14}$$

with $\Omega = \omega - \omega_0$. Equations 2.14 and2.13 are not limited to the description of just X waves but describe a larger family of stationary conical wavepackets.
It is possible to divide conical waves into three families on the basis of the particular form of the $k_\perp(\omega)$ relation. This in turn depends solely on the material dispersion relation $k(\omega)$. We may see this by taking the Taylor expansion of the wavevector k

$$k(\omega) = k(\omega_0) + k_0'(\omega - \omega_0) + \frac{1}{2}k_0''(\omega - \omega_0)^2 + \frac{1}{6}k_0'''(\omega - \omega_0)^3 + \cdots \tag{2.15}$$

with $k_0' = dk/d\omega|_{\omega_0}$, $k_0'' = d^2k/d\omega^2|_{\omega_0}$ and $k_0''' = d^3k/d\omega^3|_{\omega_0}$. The relative weight of each of these terms will determine the shape of the spectrum. Three different cases may be described:

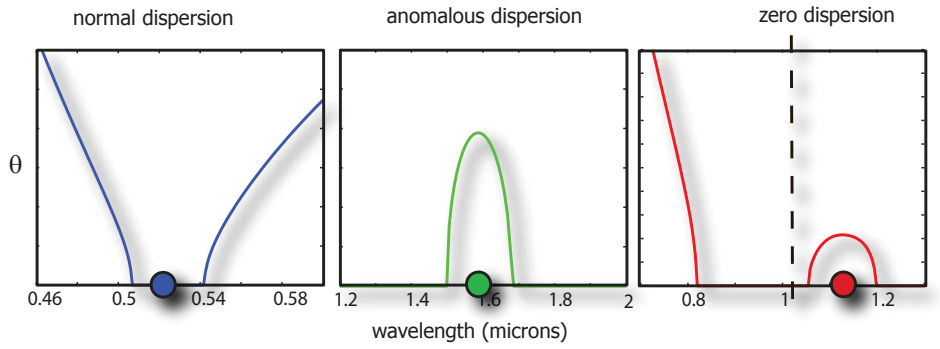

Fig. 2.5. (θ, λ) spectra in three different dispersion regimes, normal, anomalous and near to the zero-dispersion wavelength.

1. $1/6k_0'''(\omega-\omega_0)^3 \ll 1/2k_0''(\omega-\omega_0)^2$ and $1/2k_0''(\omega-\omega_0)^2 > 0$:
   in this case the spectrum will be symmetric and will exhibit hyperbolic X-like tails (X waves)
2. $1/6k_0'''(\omega-\omega_0)^3 \ll 1/2k_0''(\omega-\omega_0)^2$ and $1/2k_0''(\omega-\omega_0)^2 < 0$:
   in this case the spectrum will be symmetric and will exhibit an eliptical shape (O waves)
3. $1/6k_0'''(\omega-\omega_0)^3 \sim 1/2k_0''(\omega-\omega_0)^2$:
   independently of the sign of $d^2k/d\omega^2$ the spectrum will be asymmetric and will exhibit characteristics common to both X and O waves (Fish-waves)

In Fig.2.5 we show examples of the three dispersion-relation families. The graphs are calculated using the dispersion relation for water. Water has it's zero-dispersion wavelength at 1000 nm ([54]) so that at shorter wavelengths we have normal dispersion and at longer wavelengths anomalous dispersion. It is therefore possible to pass from one case (X, O or fish) to the other by simply changing the central wavelength of the pulse. We therefore have a clear one-to-one relation between the $k_\perp(\omega)$ spectrum and the near-field intensity profile of the conical wave. However it is important to realize that in order to guarantee stationarity it is not necessary to actually excite the full spectrum. This of course would even be impossible in the case of the X wave that has an unbounded spectrum. So, in reality, even small sections of the spectra shown in Fig.2.5 will still give stationary pulses and may be referred to using the same terminology (X or O waves) introduced here. We shall see later on that the most typical case encountered in experiments is that in which only one of the two hyperbolical tails of the X wave is excited. This "half" X wave is still stationary and all of the important physical properties of the full X wave are still present. So for all practical purposes, such a pulse

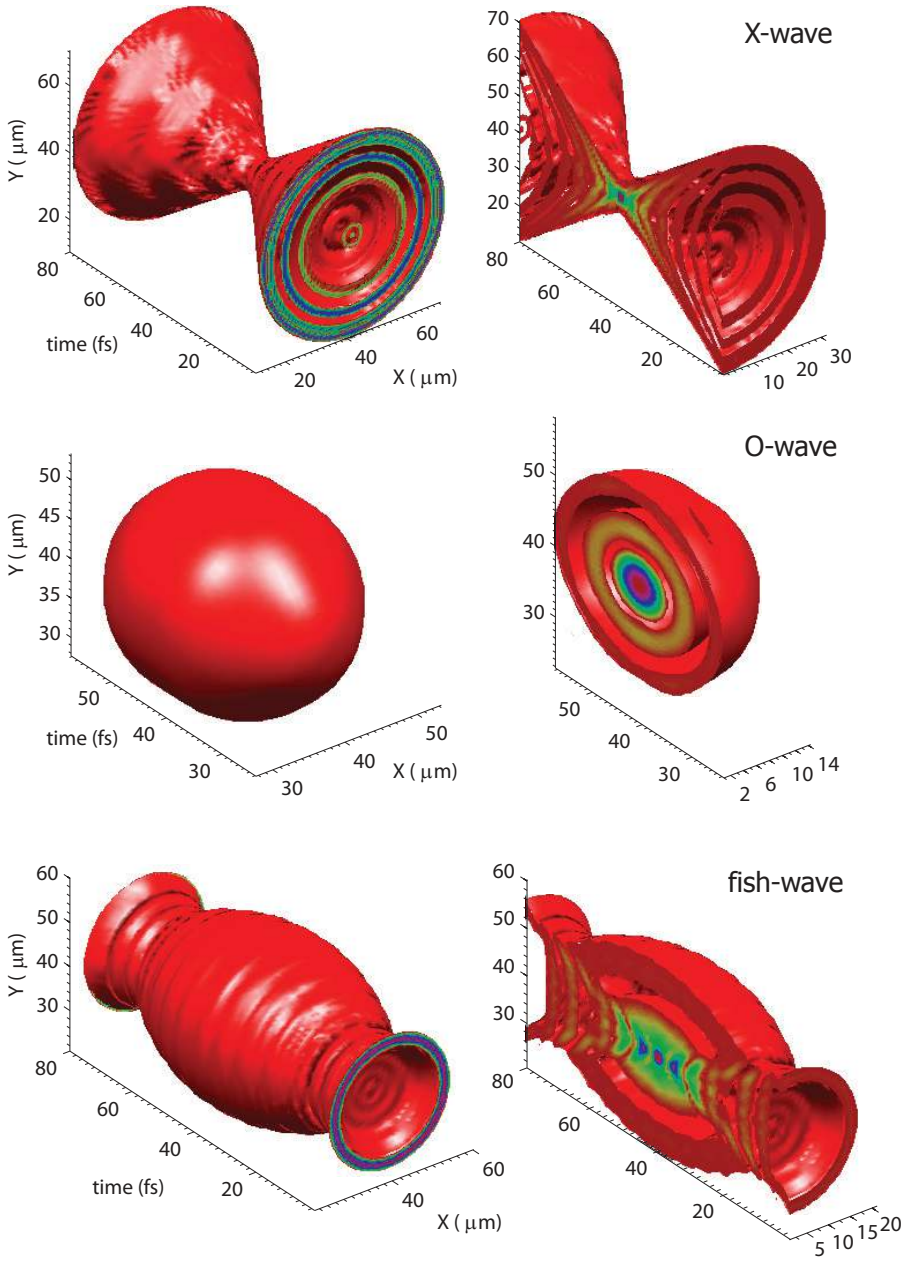

Fig. 2.6. Conical wave near-field profiles caculated for the cases of dominant normal dispersion (X waves), anomalous dispersion (O waves) and near to the zero-dispersion wavelength (fish waves). The graphs show the isocontour of the full volume and a cut-out showing the wave-packet interior intensity distribution.

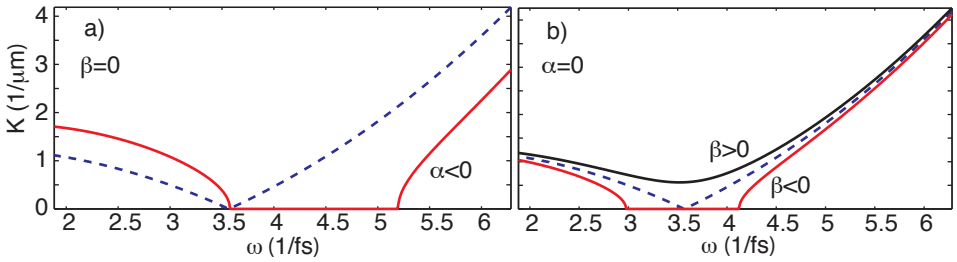

Fig. 2.7. Conical wave $(k_\perp, \omega)$ curves calculated using Eq.2.12. Parameters are $\omega_0 = 2\pi c n(\lambda_0)/\lambda_0$ with $\lambda_0 = 527$ nm with $n(\lambda)$ corresponding to water ([54]). Dashed lines are for $\alpha = 0$, $\beta = 0$. In a) $\alpha < 0$ and $\beta = 0$. In b) $\alpha = 0$ and the two curves correspond to $\beta > 0$ and $\beta < 0$.

is still an X wave.

Wave-equation stationary solutions

In Eq.2.14 we constructed the conical wave stationary pulse as a superposition of non-diffracting Bessel beams, each at a different frequency and chosen so that the angular distribution gives non-dispersive propagation (Eq.2.12). It is also possible to derive a similar $k_\perp(\omega)$ relation starting directly from the wave-equation. First lets simplify Eq.2.12. By Taylor expanding $k(\omega)$, performing the multiplications and keeping only terms up to second order in $\Omega = (\omega - \omega_0)$ we find

$$k_\perp = \sqrt{2k_0\left(\beta + \alpha\Omega + \frac{1}{2}k''\Omega^2\right)}. \tag{2.16}$$

This equation describes the dispersion relation of a polychromatic stationary conical wave within the paraxial approximation and under the assumption that only second order dispersion is relevant. This may also be obtained by noting that under the paraxial approximation and up to second order in dispersion, the propagation of narrowband pulses is ruled by the equation for the amplitude A

$$\frac{\partial A}{\partial z} = \frac{j}{2k_0}\nabla_\perp^2 A - j\frac{k_0''}{2}\frac{\partial^2 A}{\partial \tau^2}, \tag{2.17}$$

where z is the propagation direction, $t = t - k_0' z$ is the local time and $\nabla_\perp^2 \equiv \partial^2/\partial x^2 + \partial^2/\partial y^2$. Without going into too much detail here (see Ref.[55]) it can be shown that by substituting into the wave-equation Eq.2.17 the general form of a solution whose envelope is assumed to be stationary in

some reference frame, one finds a condition in the spectral domain that is identical to Eq.2.16 and the stationary envelope A is precisely that given in Eq.2.14.

Phase and group velocity

Let us now return to the $k_\perp(\omega)$ relation in Eq.2.13 and look a bit more deeply at the meaning of the two parameters, α and β. In Fig.2.7 we show the conical wave spectral curves calculated for water around a central wavelength $\lambda_0 = 527$ nm. The dispersion relation $n(\lambda)$ for water is taken from Eq.12 in Ref.[54] and shall be used extensively from hereon. This relation and the measurements provided in Ref.[54] give $k_0' = 4.5$ fs/μm, $k_0'' = 0.06$ fs^2/μm and $k_0''' = 0.007$ fs^3/μm near 500 nm. This implies that the third order dispersion may be neglected (as long as the spectrum does not extend too far) and the conical wave relation is that of an X wave. Fig.2.7(a) shows what happens when we keep $\beta = 0$ and we vary α. In this case we took $\alpha < 0$ and we see how the X wave curve shifts to higher frequencies and a gap appears between the two X-tails. As the absolute value of α increases so does the gap between the two tails while one of these always passes through ω_0. This situation describes very closely many typical experimental situations. We may define a carrier frequency as

$$\bar{\omega} = \frac{\int \omega I(\omega) d\omega}{\int I(\omega) d\omega}. \tag{2.18}$$

The phase and group velocities of the conical wave are then defined through the relations [55, 56]

$$v_z^g = \frac{1}{k'(\omega_0) - \alpha}, \tag{2.19}$$

$$v_z^\phi = \frac{\bar{\omega}}{k(\bar{\omega}) - \beta}. \tag{2.20}$$

Therefore, by tuning the values of the free parameters α and β we have the possibility to tune the phase and group velocity of the conical wave.
Let us know look briefly at the effect of the β parameter. Fig.2.7(b) shows the X wave curves for $\alpha = 0$ and $\beta > 0$ and $\beta < 0$. Both curves are centered at ω_0 so that their group velocity is not varied with respect to a standard Gaussian pulse centered at the same frequency but the phase velocity is either subluminal ($\beta < 0$) or superluminal ($\beta > 0$).
We underline once more the fact that conical waves may have either subluminal or even superluminal propagation velocities. We have seen that in the case of the electric-field X wave introduced by Lu and Greenleaf, the

phase and group velocities are equal to each other and always greater than c. However, the group and phase velocities in question refer only to the longitudinal components of the velocity, i.e. along the propagation direction. As we have already pointed out, even a plane wave propagating with a velocity v but at an angle θ with z will have $v_z = v/\cos\theta$ and, depending on the angle, this may be made larger than c. So this example too may seem to violate causality but, simply, it does not due to the fact that the causality relation does not apply strictly to (some component of) the group velocity but rather to the signal, or information, velocity. So the problem actually lies in the physical meaning that is often erroneously attributed to the group velocity, as originally pointed out by L. Brilloiun some years ago [57]. The group velocity, as weird as it may seem, can be greater than c, infinite or even negative while still retaining its meaning as the velocity of nearly undistorted pulse propagation (see also Ref.[58]).

Measuring the group velocity

Many of the results and diagnostic tools described here are based on pulse characterization in the Fourier $(k_\perp, \omega)$ space. One of the many unique features offered by this approach is that measurements performed in this domain allow direct access to the value of the group velocity of the conical wave packet (or in general of any pulse). Let us consider for example a situation in which we observe the spontaneous formation of a stationary wave-packet in normal dispersion, i.e. an X wave, and we want to determine its group velocity. We start from the measured $k_\perp(\omega)$ values: from these we may derive $k_z = \sqrt{k(\omega)^2 - k_\perp^2(\omega)}$ (using the material dispersion relation for $k(\omega)$). If we find a linear relation between k_z and ω then we may conclude that the spectrum is that of a stationary, or more precisely, non-dispersive wave-packet (see Eq.2.13). By taking the first derivative with respect to ω of this linear relation we recover the group velocity.
This method is very general, may be applied to a variety of cases (e.g. pulses of any shape and not necessarily conical waves) and is particularly indicated for situations in which we do not have the luxury of a fully formed X wave spectrum, so for example only one X-tail (or part of this) is excited.

2.2 Nonlinear conical waves

The discovery of a stationary state in a given physical system is never trivial and is of interest due not only to its fundamental implications but also due to possible, real-world applications. Conical waves are no exception in this sense. Yet, these particular wave-packets have an extra feature that renders them even more interesting: they are stationary not only in the linear but

also in the nonlinear regime. This is quite a unique property, i.e. they may be seen as a continuous family of wave-packets parametrized by the intensity (i.e. going from the linear to the nonlinear regime), whereas for example solitons (which are intrinsically nonlinear structures) exist only as discrete solutions to the propagation equation (their parameters such as peak intensity must satisfy specific relations). So the soliton has no linear analogue. Furthermore serious problems arise when we try to generalize the soliton concept to three dimensional systems. In real-world materials the same nonlinearities that allow balancing diffraction and dispersion will also kill the pulse. Indeed there is always an imaginary, absorbing, term associated to the real, self-focusing, nonlinearity and the intensities required to excite the full 3D soliton will lead to such high nonlinear absorption losses that there is no hope to actually observe its formation ([48]). Nonlinear conical waves, on the contrary, display remarkable features: they are stationary in both the linear and the nonlinear regime and their propagation, rather than hindered, may even be promoted and sustained by nonlinear losses.

2.2.1 Kerr nonlinearity and stationarity: the nonlinear X wave

The wave-equation Eq.2.17 is very similar to the nonlinear Schrödinger equation that we was derived in Chapter 1,

$$\frac{\partial A}{\partial z} = \frac{j}{2k_0}\nabla_\perp^2 A - j\frac{k_0''}{2}\frac{\partial^2 A}{\partial \tau^2} + \frac{k}{n_0}n_2|A|^2 A. \tag{2.21}$$

Indeed the two equations differ only due to the presence of the nonlinear term. In 2003 Conti et al. showed that the NLSE in normal dispersion has a stationary solution in the form of an X wave [59], the "nonlinear X wave" (NLXW). This finding in itself is important as it marks a distinct difference with respect to solitons. The extension of the concept of the soliton to the 3D realm was proposed in the nineties by Silberberg (the optical light bullet) [60] but this requires anomalous dispersion, large intensities and neglects the occurrence of losses. This is a serious limitation in many situations due to the fact that most materials exhibit normal dispersion in the wavelength regions (500-1000 nm) at which high power lasers are available. This has hindered somewhat a widespread application of soliton technology. Even in the case of optical fibers for which high power lasers at 1500 nm are now available and the coefficients of glass have been carefully measured, soliton transmission systems have still not made the expected technological impact. Conti also highlights a fundamental difference between the linear and nonlinear regimes: "NLXWs can be generated spontaneously at high intensity from conventional bell-shaped (in space and time) input beams through self-induced spectral reshaping triggered by conical emission."

This indeed is the first link that we have with laser pulse filamentation. In chapter 1 we saw that one of the main features of filamentation is conical emission, a spectral broadening that appears with different frequencies emitted at different angles. If these angles are such that the longitudinal component of the wavevector varies linearly with frequency then the pulse will be non-dispersive (Eq.2.13).
Conti actually performed his analysis not only for Kerr media but also for materials with a second order ($\chi^{(2)}$) nonlinearity finding the same results. Indeed the first verification of the spontaneous transformation from an input Gaussian pulse into a stationary X wave was obtained in a Lithium-Troborate (LBO) $\chi^{(2)}$ crystal [29]. So the existence and spontaneous formation of X wave states appears as a very general phenomenum and does not depend crucially on the type of nonlinearity involved. Conti et al. have even shown that the same physics may be extended to apparently completely different systems such as Bose-Einstein condensates [61].

2.2.2 Nonlinear losses and stationarity: the Unbalanced-Bessel beam

So far we have described the NLSE and noted that it has X-shaped stationary solution. However nonlinear losses, the number-one enemy of multidimensional optical solitons, were not included in this analysis. One of the most surprising features of nonlinear conical waves is that there is a class of such waves whose stationarity is sustained by a continuous refilling of the nonlinearly absorbed central spot with the energy supplied by the linear, conical tails [62].
This was shown starting from the so-called 2D+1 NLSE [2] with an extra term added that accounts for nonlinear losses [62] :

$$\frac{\partial A}{\partial z} = \frac{j}{2k_0}\nabla_\perp^2 A + \frac{k_0}{n_0} n_2 |A|^2 A - \frac{\beta^{(K)}}{2}|A|^{2K-2}A, \tag{2.22}$$

where $\beta^{(K)}$ is the nonlinear absorption coefficient and $K = 2, 3, \cdots$ indicates the number photons involved in this multiphoton process. The stationary solution to this equation may be found numerically but this solution also has an analytical formula that describes its asymptotic shape, i.e. far from the central peak:

[2] The "2D+1" term indicates that we are studying the evolution of a monochromatic beam so that the temporal envelope of the pulse is not considered. In other words, only the transverse (x,y) profile (thus "2D") is studied during propagation along the z direction (thus "+1"). In contrast the NLSE shown in Eq.2.21 accounts also for a non-uniform profile and may be indicated as the "3D+1 NLSE"

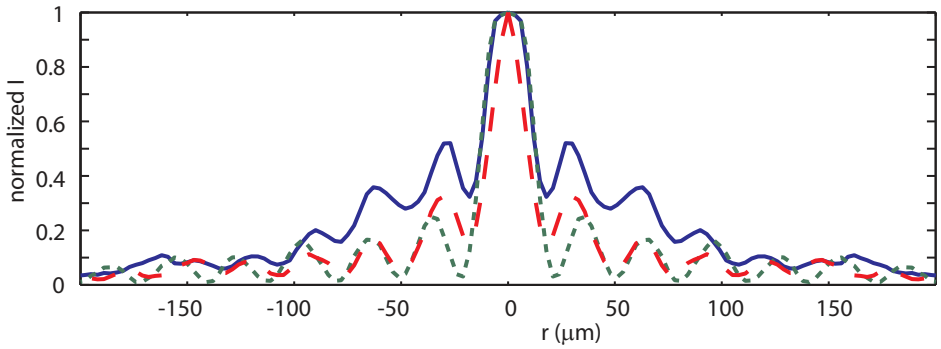

Fig. 2.8. Experimentally measured transformation of a linear Bessel beam (dotted green line) into a nonlinear UBB with increasing input energy, from 600 μJ (from red dashed line) to 1400 μJ (blue solid line). The Bessel beam transforms by shrinking in diameter and in reducing the contrast of the external oscillations.

$$A \simeq \frac{a_0}{2}[\alpha_{\text{out}} H_0^{(1)}(\sqrt{2k\delta}r) + \alpha_{\text{in}} H_0^{(2)}(\sqrt{2k\delta}r)]e^{-j\delta z}. \tag{2.23}$$

A is formed by two nondiffracting Hankel beams of the first and second kind, with the same cone angle $\theta = \sqrt{2\delta/k}$, but different weights, α_{out} and α_{in}. It is important to recall at this point the zero-order Bessel function may be written as a sum of a Hankel functions of the first and second order, as shown in Eq.2.23, with equal weights $\alpha_{out} = \alpha_{in}$ (and $\delta = 0$) and that $H_0^{(1)}(\theta)$ represents an outgoing wave propagating with an angle θ and originating from a source located at the Bessel peak while $H_0^{(2)}(\theta)$ is an incoming wave at an angle θ and disappearing in a sink in the same position of the source for $H_0^{(2)}$. The oscillations in the Bessel function may therefore be viewed as the interference between the incoming Hankel and the outgoing Hankel fields. So the meaning of Eq.2.23 is now clearer: by creating an unbalance between the two Hankel fields, e.g. $\alpha_{in} > \alpha_{out}$, we will have an incoming flux of power that may balance out losses that occur due to nonlinear absorption in the central peak. Clearly true stationarity, i.e. over an infinite distance, requires an infinite amount of energy in the unbalanced beam (UBB). The same argument applies also for a the standard balanced beam and the solution is the same in both cases and we have already noted that practical applications do not require stationarity in this strict sense but only over a certain distance so that the total required energy will be finite. Finally the parameter δ in Eq.2.23 accounts for the presence of the Kerr term in Eq.2.22 that will lead to an additional phase shift in the Hankel fields with respect to the linear case. So overall, if we compare the Bessel beam with the nonlinear-UBB we

should expect to note a reduced visibility of the radial oscillations due to the unbalancing of the incoming and outgoing waves and a compression of the rings and central peak due to the Kerr-induced phase-shift.
Fig.2.8 shows the experimentally measured transformation of a linear Bessel beam in presence of Kerr nonlinearity and nonlinear losses. The idea of the experiment was to try to excite the nonlinear UBB by starting from a beam profile as close as possible to the final state. The Bessel beam was therefore our obvious choice. We generated the Bessel beam starting from a Gaussian beam (527 nm central wavelength, 200 fs temporal duration) that was sent through an axicon (vertex angle = 175 deg). The Bessel beam was then passed through a 4 cm long cuvette filled with water. If the input energy is high enough then the Kerr nonlinearity and nonlinear losses will be excited. As can be seen in Fig.2.8 the input Bessel beam (dotted green line) undergoes a strong transformation with increasing input energy, from 600 μJ (from red dashed line) to 1400 μJ (blue solid line). Clearly the rings shrink in diameter (this is most clearly seen looking at the position of the first minimum along the r-axis) and lose contrast with an effect that increases with increasing energy. It therefore appears that indeed the strong nonlinear losses are inducing the balanced Bessel beam to unbalance the incoming and outgoing energy flows so as to counteract the energy losses that are occurring at the central, high intensity peak.

2.2.3 Nonlinear conical waves and filamentation

We have already pointed out the tight connection that exists between spontaneous evolution of an ultrashort Gaussian pulse in the presence of an optical nonlinearity and X waves. The NLS equation used to study the problem, Eq.2.21 is somewhat simpler that the equation that is frequently used to simulate numerically ultrashort laser pulse filamentation, Eq.1.31. This is due to the fact that the extremely high intensities reached during the filamentation process lead to a number of nonlinear processes such as plasma generation, nonlinear losses, Stimulated Raman Scattering that must be accounted for.
The connection between filamentation and conical waves was proposed for the first time in 2004 in two independent works by Dubietis and Kolesik. Dubities carried out a series of experiments in water ([63, 12]) showing that the filament propagates without any self-channeling mechanism [12], in contrast with the more popular model for filamentation in air [11]. Quoting Dubietis' own words: "the propagation of intense 200 fs pulses in water reveals light filaments not sustained by static balance between Kerr-induced self-focusing and plasma-induced defocusing. Numerical calculations outline the occurrence of a possible scenario where filaments appear because of spontaneous reshaping of the Gaussian input beam into a conical wave, driven by

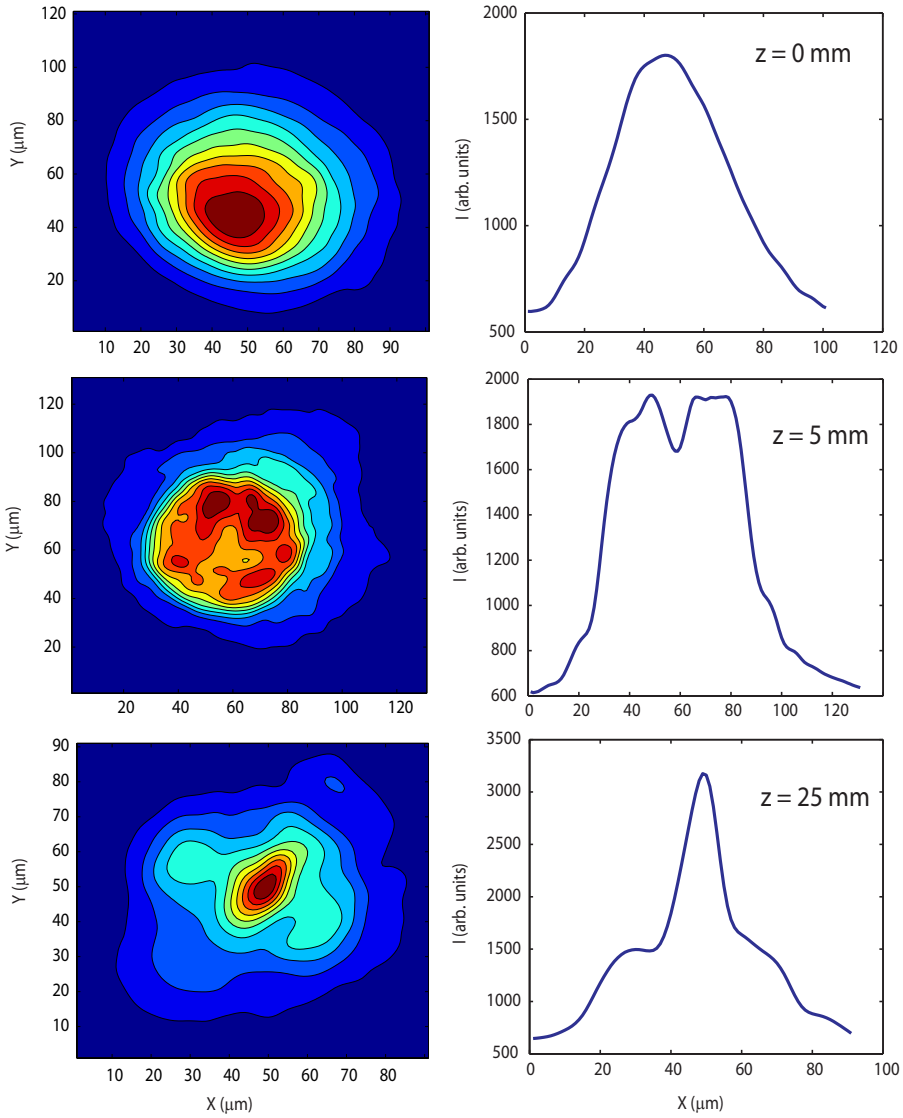

Fig. 2.9. Experimentally measured transformation of an input Gaussian transverse profile (full spatial profiles to the left, a single section along the beam center to the right). The input profile (z = 0 mm) is roughly Gaussian in shape but quickly transforms under the action of nonlinear losses (z = 5 mm) and exhibits a flat top. This flat top will then lead to the formation of rings (already visible in the z = 5 mm measurement). These rings will then focus down and form the filament (z = 25 mm).

the requirement of maximum localization, maximum stationarity, and minimum nonlinear losses". The experiment with which this was demonstrated is conceptually simple but extremely effective. In order to verify the guiding mechanism a filament was formed in water from an input Gaussian pulse focused to around 100 μm at ther input facet of the water cuvette. For input energies in the 2-5 μJ range the nonlinear focus will be situated roughly at about 1-2 cm from the input facet and a filament will thus form[3]. At this point Dubietis placed first a 55 μm pin-hole in the path of the filament so that only the central spike of the filament passes through. This, somewhat unexpectedely, caused the sudden death of the filament and the transmitted peak suffered strong diffraction. On the other hand, when a stopper was placed in the path of the filament so that all of the beam passed except for the central intense spike (recall that the central spike is surrounded by a much larger, low-intensity background) then the spike reformed nearly immediately and further propagation was practically identical to that of the unperturbed filament. This striking finding was explained by suggesting that the filament propagates in the form a conical wave so that energy is continuously flowing from the surrounding energy reservoir toward the central spike. As soon as the spike is removed the refilling mechanism will recreate it. If the reservoir is removed, then the central spike shall also disappear. In the same work the experiments were reproduced with a numerical model similar to Eq.1.31 in which all effects related to plasma generation were neglected and Kerr nonlinearity and nonlinear losses were the dominant nonlinear terms. It therefore appears that the conical wave, i.e. a central intense spike surrounded by a large background of light moving at an angle with respect to the propagation axis, may spontaneously appear starting from a Gaussian pulse, in the presence of strong, localized nonlinear losses. In order to see how this occurs let us first consider the effect of nonlinear losses on an intense Gaussian pulse.

Nonlinear losses will affect primarily the more intense parts of pulse, i.e. the higher the intensity the larger the losses will be. This will lead to a beam flattening due to the losses that cut away the more intense parts of the pulse. This flat-top structure will then, under the action of the Kerr nonlinearity, lead to self-focusing in the form of a ring [64]. A similar dynamics has been reported for super-Gaussian input beams that are also flat-top. The intense ring-shaped modulation will then further shrink and result in a very intense spike in the center of the beam, still surrounded by ring-shaped structures. Consequently, the formation of filaments can be interpreted as due to the

[3] Note that these working conditions, input Gaussian profile, 200 fs pulse duration (FWHM), 100 μm diameter (FWHM), 527 nm central wavelength, input energies 1-6 μJ are the same as those used in most of the experiments described in these pages

on-axis sink i.e. nonlinear losses leading to an inward energy flow from the surrounding reservoir. The evolution described here is shown in the experimental measurements of Fig.2.9. The beam transverse profile is measured at three different propagation distances for a filament forming in water. At z = 0 mm we see the (nearly) Gaussian input. At z = 5 mm we clearly see the effect of the nonlinear losses that have flattened the beam top and the Kerr nonlinearity has already induced an initial weak ring-shape. This will then self-focus and form the filament, shown at the output of the water sample (z = 25 mm).

Kolesik et al. gave the first clear description of filamentation in terms of spontaneously formed X waves [31]. In their simulations pulse splitting after the nonlinear focus is induced by group-velocity dispersion and each split pump pulse will lead to the formation of an X wave. Further propagation is characterized by the dynamical interaction of these X waves which may create a flux of energy toward the temporal slices between the two pulses and the subsequent reformation of a strong central peak. This may then in turn split once more and explain the cyclical dynamical replenishment of the central intensity peak. In other words, although the filamentation process is descibed on the basis stationary amplitude X wave profiles, the interaction and propagation of these under a common envelope actually leads to a highly dynamical process that keeps on "boiling" until it dies out.

So, summarizing, filament propagation in condensed media may be explained as the dynamical interaction and propagation of conical wave-packets that are spontaneously formed in the presence of strong nonlinear losses. Although this picture is somewhat different from the generally accepted model for filamentation in gases, the same mechanisms at play in condensed media are also present in air. Furthermore other effects, associated for example to plasma generation, may also give similar effects to those of nonlinear losses and in any case we should recall that the nonlinear X wave has been shown to be a stationary state to the NLSE (pure Kerr nonlinearity) [59]. It is therefore reasonable to expect to find evidence of spontaneous conical wave formation in all filaments, irrespectively of the media in which they are formed.

3

Ultrashort laser pulse diagnostics

The measurement and characterization of ultrashort optical pulses is an extremely important area of laser research. The whole idea of using ultrashort pulses is related to the fact that we are always trying to push our knowledge to the limits and we are interested in measuring ever shorter events of physical processes. But what is the point of all this if we aren't able to measure the pulses? This issue is not as trivial as it may seem. In order to measure some ultrashort event, such as a femtosecond laser pulse, we will need something that is even shorter. This can obviously be somewhat troublesome if the laser pulse is the shortest object that we have in the lab. The best we can do is try to measure the pulse using the pulse itself as a reference: starting from this idea the autocorrelation, cross-correlation and similar techniques, such as the frequency resolved optical gating (FROG) were invented. These are treated in great detail in Rick Trebino's book ([65]), the inventor of the FROG technique, and the reader should refer to this for more information. Here we will give an overview of some measurement techniques that rely on an extension of the standard cross-correlation measurement or on indirect detection of the pulse phase always following the mainstream idea that we are interested in a full 3D characterization. It would of course by much better if we could detect the three dimensional pulse phases directly. This is indeed possible although the measurements are usually somewhat more complicated than those shown here or, alternatively, require the use of non-obvious phase retrieval algorithms. Work is still proceeding in this complex and fascinating area and recently single shot, full 3D phase recovery measurement techniques have been proposed [66]. However retrieving the full 3D phase profile of very complex pulses appears to be *much* more difficult than retrieving the phase profile at just one single radial position of the pulse. So whilst FROG and similar techniques should be seriously considered if you want 1D phase information, we will try to propose alternative measurements that may give us the needed information in full 3D space without necessarily resorting to the full phase pattern.

3.1 Correlation techniques

Let us assume that we wish to characterize the temporal profile of a very short optical pulse. As we have pointed out this pulse will most probably be the shortest object in our lab and, if the pulse duration is in the picosecond or femtosecond range, there is no hope to measure it using for example a photodiode as the diode response and electronics cannot follow such fast intensity variations.
A widely used technique for 1D temporal characterization is the autocorrelation. The most common implementation of this is based on second-harmonic generation in a crystal that has $\chi^{(2)} \neq 0$ (see Eq.1.1). If we split the pulse under measurement in two, using for example a beam splitter, we may then recombine the two pulses in the crystal. If the two beams arrive at the crystal with slightly different angles then the crystal will produce a non-collinear signal at the second-harmonic (SH) frequency that will be emitted at an angle roughly half-way between the two input beams. The noncollinear SH will have an intensity (measured by a photodiode) given by

$$I_{\mathrm{SH}}(\tau) \propto \int_{-\infty}^{+\infty} I(t)I(t-\tau)dt, \tag{3.1}$$

where τ is the relative temporal delay between the two pulses. Therefore the SH signal is given by the correlation function, or self-convolution, of the pulse. So now we may retrieve the pulse temporal shape by finding the $I(t)$ profile whose correlation function is equal to the measured SH trace. Altough this seems very simple the method actually hides a number of traps, some serious, others a bit less, but they should nevertheless not be forgotten [65]. From an experimental point of view we must take care that a certain number of constraints are satisfied:

- the pulse widths w_0 at the crystal must be much smaller than the pulse duration $c \cdot t_0$. The risk of not respecting this limitation is that the measured autocorrelation trace will be lengthened due to a continued overlap of the two pulses along the pulse spatial wings. In order to avoid this we should also try to keep the angle between the two beams as small as possible (see Fig.3.1.)
- the SH conversion has a limited bandwidth due to the fact that each frequency will be perfectly phase-matched for a slightly different orientation of the crystal. If the bandwidth is very large not all of these components will be converted resulting in a modified (longer) autocorrelation trace. The temporal interpretation of this effect is based on the pulse and SH different group-velocities. In a long crystal the two pulses will separate more in time with respect to a shorter crystal. In other words this problem may be avoided by using shorter crystals.

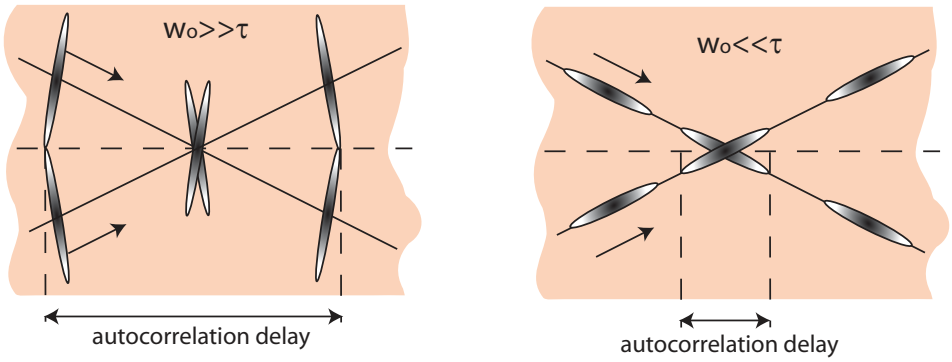

Fig. 3.1. Schematic picture of the autocorrelation obtained in the two cases $w_0 >> \tau$ and $w_0 << \tau$. The former will lead to overestimation of the pulse duration due to the large beam width. The latter will give the correct value for the pulse duration τ. The "autocorrelation delay" indicates the relative delay (between the two pulses) region for which a noncollinear SH signal will be measured at the crystal output.

A correct autocorrelation trace will always be symmetric and will give a direct indication of the pulse temporal structure of the pulse at some transverse coordinate, usually the pulse center at $r = 0$. However it is important to note that the best an autocorrelation can give is just an indication of the pulse structure and sometimes even the "indication" may be wrong. Trebino [65] lists a number of cases and shortcomings of the autocorrelation method, in particular a series of cases in which quite different pulses will give identical, or in any case experimentally indistinguishable, autocorrelation traces. So, for example, an autocorrelation trace may indicate how many peaks or pulses are present as long as the structure is not complicated and may be assumed as a combination of Gaussian (or similar) pulses. So some kind of guess is needed for the pulse shapes. Similarly we may have a simple pulse without any relevant structure (e.g. multiple peaks) and want to determine the pulse temporal duration. The root-mean-square (rms) width of a convolution $c(t) = f(t) * g(t)$ is given by $\tau^2_{rms-c} = \tau^2_{rms-f} + \tau^2_{rms-g}$ so that in the case of our self-convolution the autocorrelation trace rms width is $\sqrt{2}$ time the pulse intensity rms width[1]. This is very useful if we want the rms pulse width but usually we want the Full-Width-Half-Maximum (FWHM) or something similar. But in order to obtain such information we must once more make guess regarding the pulse shape. For example a Gaussian pulse will give an intensity autocorrelation trace that is $\sqrt{2}$ times wider, a $\mathrm{sech}(t)^2$

[1] The pulse rms width is defined as $\tau^2_{rms} = \langle t^2 \rangle - \langle t \rangle^2$ where $\langle t^n \rangle = \int t^n I(t) dt$.

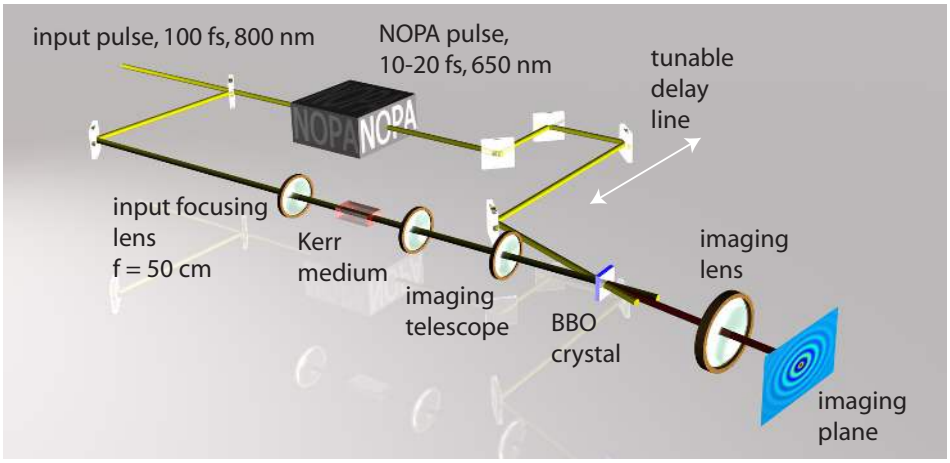

Fig. 3.2. Experimental layout for three-dimensional imaging of ultrashort laser pulses.

gives an autocorrelation that is 1.54 times wider and so on.
So the main message is that autocorrelation trace results should be treated carefully. Trebino gives an excellent review of what can and what cannot be said using autocorrelation traces and we won't go any further in this direction. However the main limitation we want to overcome is the reduced information due to the lack of any spatial resolution in standard autocorrelation traces. For example the autocorrelation method outlined above will not tell us if the pulse is characterized by a spatiotemporal coupling, i.e. if the pulse temporal profile depends on the transverse spatial coordinate. Of course we may repeat the autocorrelation, each time selecting a different portion of the pulse and then trying to recombine the data to obtain some kind of r, t map. But there is a more efficient way of doing this.

Three dimensional intensity mapping

The idea of the three dimensional (3D) intensity mapping technique is that by using a "gate" pulse that is much shorter than the pulse we want to characterize, we may perform a cross-correlation and, by keeping all the information also in the transverse spatial direction, we may reconstruct the full 3D (r, t) intensity profile. The idea is very simple: a very short gate pulse acts as a knife selecting single portions of the pulse at each delay so that, for a fixed delay, only the section of the pulse that is overlapped with the gate will be converted in frequency at the nonlinear crystal. By keeping the gate pulse very wide (with respect to the pulse we are characterizing) so that in the transverse spatial direction we may take it as practically constant, the

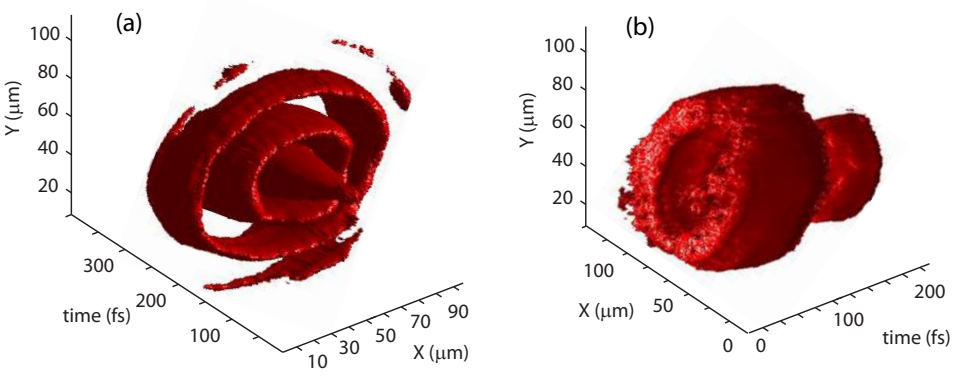

Fig. 3.3. Three dimensional intensity map of (a) a Bessel-Gauss pulse. and (b) of a spontaneously generated X wave in a crystal with second order nonlinearity (from Ref.[29]).

second harmonic or sum frequency signal generated by the nonlinear crystal will reproduce the pulse transverse intensity distribution. Ideally we would like our gate pulse to have a perfectly uniform spatial distribution and an infinitely short duration so that the sum-frequency signal will be

$$\begin{aligned} SF(x,y,\tau) &\propto \int_{-\infty}^{+\infty} F(x,y,t)G(x,y,t-\tau)dt \\ &= \int_{-\infty}^{+\infty} F(x,y,t)\delta(t-\tau)dt \\ &= F(x,y,\tau) \end{aligned} \tag{3.2}$$

where $F(x,y,t)$ is the three-dimensional laser pulse we want to characterize and $G(x,y,t)$ is the gate pulse. So the shorter the temporal duration of G and the more uniform it is along the transverse direction, the more precise the three-dimensional reconstruction will be.

From a practical point of view it is not always obvious that we will have access to pulses in our lab that are shorter than the ones we want to characterize. Usually the shortest pulse are those used in the experiments themselves. But this is not always the case. Is is possible to resort to pulse compression techniques for the gate pulse [67, 68], while some companies (e.g. Light Conversion Ltd., Vilnius, Lithuania) provide optical parametric amplifiers that give access to 10-20 fs pulses. The basic principle of operation of this Noncollinear Optical Parametric Amplifier (NOPA) relies on parametric amplification of chirped signal produced by supercontinuum generation in a transparent medium possessing third order nonlinearity. The non-collinear geometry is used due to the broad amplification bandwidth in the visible spectral range and, when pumped with a 100 fs Ti:Sapph laser pulse it will

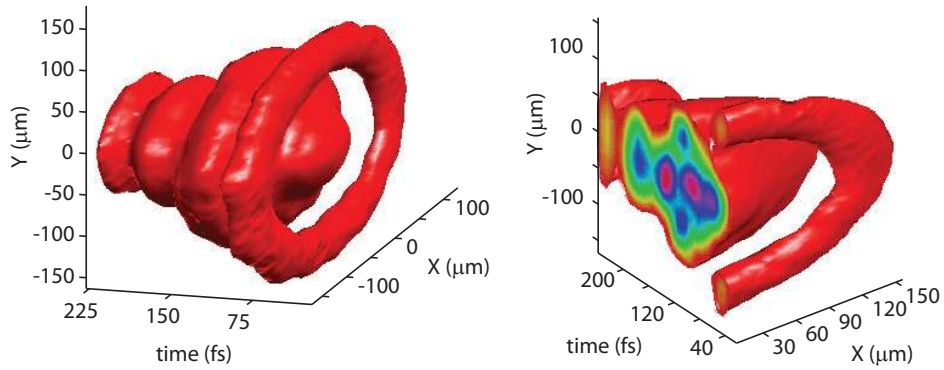

Fig. 3.4. 3D intensity map of a filamented laser pulse. The filament was induced with a 100 fs, 3.3 μJ laser pulse, focused to a 100 μm FWHM at the entrance of a 3 cm long water cell. The left-hand graph shows the full iso-surface plot at a level equal to 0.14 time the maximum intensity. The right-hand plot is the same but with a cut-through so as to highlight the internal intensity distribution.

give pulses with much lower energy with respect to the pump but with durations in the 10-20 fs range. So we may use part of the 100 fs pump pulse energy to perform our experiments and then use the 20 fs NOPA pulse to perform a 3D mapping of our pulse at the experiment output. Another option is to split our laser pulse into two before the experiment. One copy of the pulse will be used as the gate pulse while the other is stretched to a longer duration (e.g. by using a pair of gratings or, if the original pulse is short enough, by propagation in a dispersive medium such as glass). This stretched pulse may then be used for the experiment and later characterized using the shorter gate pulse.

As an example of the 3D mapping technique, in Fig.3.3(a) we show the 3D map of Bessel-Gauss pulse generated by an axicone. The figure shows an iso-surface volume map in which the radial oscillations are clearly visible. We may use the technique to measure more complicated pulses. The first experimental demonstration of the spontaneous formation of X waves was performed with this technique and allowed a direct visualization of the complicated bi-conical structure of the full three-dimensional X wave [29]. The X wave in question was generated in a crystal with a second order nonlinearity (Lithium Triborate, LBO) and the resulting X wave was particularly evident as shown in Fig.3.3(b). However, although spontaneous formation of X waves has been predicted also in Kerr media [59], in this case the resulting three-dimensional patterns are much more difficult to interpret. This is due to the fact that up to date the only regime in which the X waves appear

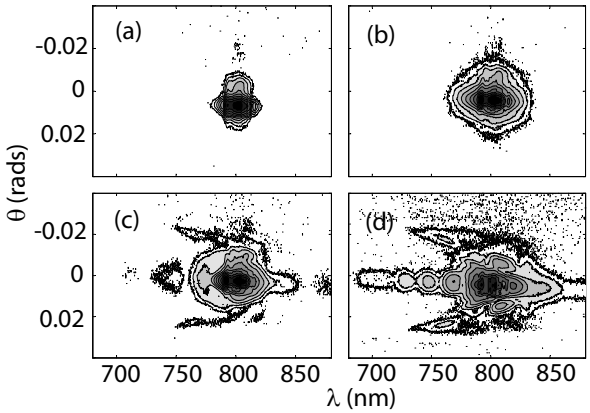

Fig. 3.5. Evolution of (θ, λ) spectrum of an 800 nm, 100 fs, laser pulse undergoing filamentation in the same conditions of Fig.3.4. (a) input spectrum, (b) after 1 cm propagation, (c) 2 cm propagation and (d) 3 cm propagation.

spontaneously in Kerr media is that of of ultrashort laser pulse filamentation. However filamentation will also lead to pulse splitting. We shall see that the whole pulse splitting process may actually be interpreted in terms of the spontaneous formation of X waves, so each split pulse is actually an X wave. This is also why filament 3D maps have proved difficult to interpret: the X-tails from each split pulse will overlap, create complicated interference patterns [69].

In Fig.3.4 we show a 3D map of an 800 nm, 100 fs, laser pulse that has undergone filamentation in 3 cm of water [69]. Although strong ring-shaped features are evident and give us an indication of the conical nature of the pulses, any actual X-shapes are actually quite difficult to see. Note the multiple peak structure, highlighted in the cut-out (right-hand graph), with each peak interfering with it's neighbors. Repeating the experiment numerically allows us to follow the evolution of the input Gaussian pulse with great detail. Such results from a numerical simulation are shown in Fig.1.10: the input Gaussian pulse splits in two and around each daughter pulse weak but clearly visible X-features develop. However the visibility of these features is clear in this simulation because we have the possibility to plot the data over a very large intensity range (in this case 6 decades). The best CCD cameras currently available will give the experimentalist at the most a 16 bit dynamic range, so only slightly more that four decades. The possibility to reveal low-intensity structures may be further reduced due to the sum-frequency process used for example in the 3D mapping measurement. So overall this implies that experimentally in some cases we may only observe the complicated central interference pattern in Fig.1.10 and completely

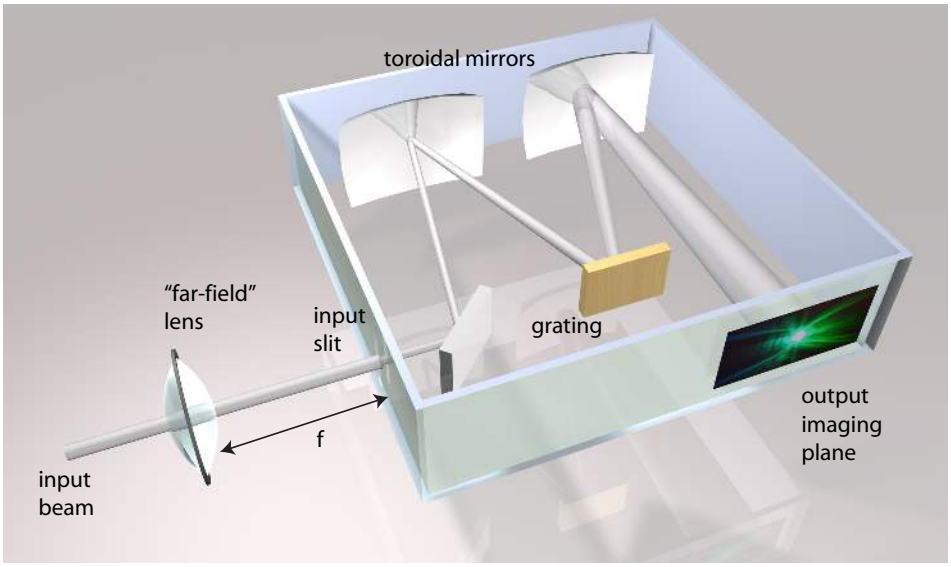

Fig. 3.6. Experimental setup used for measuring the Fourier (θ, λ) spectrum.

miss the weaker X-features. For this reason it is often convenient to resort to another measurement technique based on the measurement of the spectral far-field pattern $(k_\perp, \omega)$ (or, for the experimentalist (θ, λ)). Indeed these spectra are also X-shaped but now the X-features are much clearer and well-defined. So much so that measurements in (θ, λ) are particularly effective in revealing the presence and the specific features of X (or in general conical) waves. For example in Fig.3.5 we show the measured (θ, λ) spectrum evolution of corresponding the laser pulse in Fig.3.4 [69]. The spectrum shows clear off-axis radiation associated to the X wave that is well-separated from the on-axis part. As we shall see this allows a precise characterization of the X wave even in conditions in which the near-field may be extremely complicated.

3.2 Spectral techniques

The importance of the information contained in the Fourier spectrum $(k_\perp, \omega)$ was first pointed pointed out in experimental measurements of filaments in condensed media [70], but the same technique has also been adopted for the interpretation of numerical simulations and examined with a certain detail by Kolesik et al. [33]. The first far-field measurements bearing clear evidence of X wave formation are reported in Ref.[71] although the conical part of the

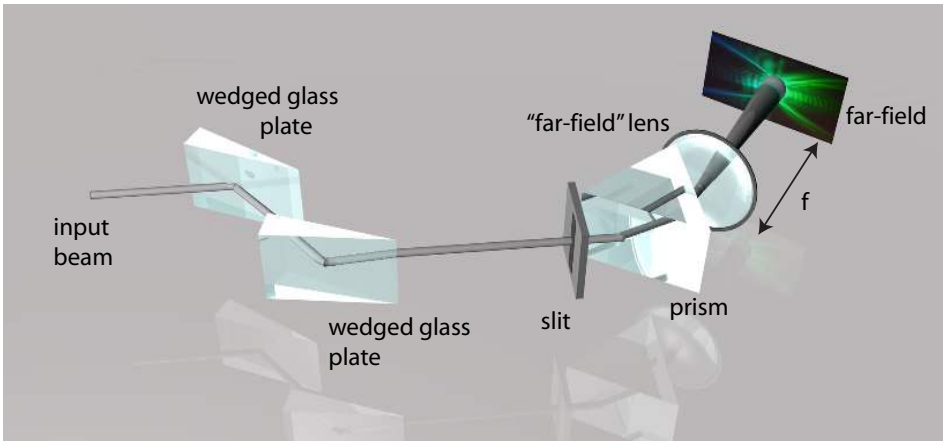

Fig. 3.7. "Short-cut" version of an experimental setup for measuring (θ, λ) spectra. The input beam is sent through a slit and then into a dispersive glass prism. The output is then passed through a lens. These three optical elements should be kept as close as possible. At a distance f from the lens one will have the (θ, λ) spectrum although the image may be blurred (due to diffraction from the slit) and the λ-axis needs to be carefully calibrated (e.g. using a fiber-coupled spectrometer) as the variation of λ along the horizontal axis is not linear and will depend on the specific prism used. In some cases it may be necessary to reduce the input pulse energy (e.g. if performing experiments with mJ pulses). This is done by taking the reflections from one or two wedged glass plates placed before the setup.

spectrum is not explicitly treated. Even earlier measurements of possible X wave patterns are shown in the second chapter of Alfano's book ([72]). Here the data were not meant to reproduce the full $(k_\perp, \omega)$ spectrum and only part of the conical features are visible.

Here we show how to go about measuring and understanding in the Fourier domain the spatiotemporal characteristics of complex ultrashort laser pulse filaments.

The measurement apparatus in itself is quite simple and is drawn in Fig.3.6. Assuming that we have a laser pulse generated by some kind of experiment, we may place a lens of focal length f at the output making sure to collect all of the light associated to the laser pulse (in particular the usually weak components that are propagating at large angles with respect to the propagation direction). At a distance f after the lens we have the so-called Fourier plane in which we find the spatial Fourier transform of our laser pulse, i.e. the pulse transverse (x, y) time-integrated intensity (fluence) distribution is transformed into it's transverse Fourier transform in (θ_x, θ_y) coordinates.

The idea is to now place the vertical input slit of an imaging spectrometer in the Fourier plane of the lens. The imaging spectrometer will reproduce the vertical spatial distribution (i.e. the θ_y distribution) at the instrument output (imaging) plane. In the horizontal direction the pulse will be Fourier transformed in the temporal domain. Therefore at the output plane of the spectrometer the horizontal axis will show the spectral distribution (in wavelength λ) while the vertical axis will correspond to the spatial Fourier transform (in angles θ). We may then place some kind of instrument that can record the full two-dimensional pattern such as film-based camera or a digital CCD camera. The wavelength scale may be easily calibrated by changing the central wavelength by $\Delta\lambda$ in the spectrometer and registering the number N of pixels on the CCD by which the central laser wavelength is shifted. In other words we determine the calibration factor $C_\lambda = \Delta\lambda/N$ nm/pixel. We may calibrate the vertical axis by using the relation $C_\theta = \Delta Y/f$ rads, where ΔY is the vertical size of the single CCD pixel[2].

Although the setup is very simple, some care should be taken in choosing and placing the "far-field" lens. It is important to try to avoid having an imaging plane that is too close to the far-field plane. For example we may have the output facet of our Kerr sample placed at 15 cm from the input of the lens. If we choose a focal length $f = 5$ cm then we will have the imaging plane located at a distance $d = 6.3$ cm which is rather close the far-field plane (located at a distance $f = 5$ cm). Such a situation may lead to some confusion between the (r, λ) and the (θ, λ) spectra. This may easily be avoided by choosing a lens with $f = 15$ cm so that $d = 37.5$ cm and the imaging and Fourier planes will be well-separated. However we do have another constraint and that is the size of the sensor (typically a CCD camera). Increasing f will lead to an increase in the vertical dimension of the spectrum $D_Y = f \cdot \theta$ and this may no longer fit into the sensitive region of the sensor. So a compromise must be found between the two requirements of a well resolved spectrum and the size of the CCD chip. Finally, it is also recommendable to use an achromat, i.e. a lens composed of more than one kind of glass so as to reduce chromatic aberrations and in any case to check the lens focal length at the laser central wavelength. Usually the lens is assigned a nominal focal length measured for example with He-Ne laser at 632 nm and large differences may be found at your actual working wavelength. As a last comment we note that although imaging spectrometers are already present in many laboratories and are commercially available for less that 6000 USD (just to name a few companies, Lot-Oriel, Acton, Roper, Andor

[2] We have described how to measure the (θ, λ) spectrum. This is analogous to the $(k_\perp, \omega)$ spectrum and the two spaces are related by the simple relation $\theta = k_\perp/k$ and $\lambda = \omega/(2\pi c)$. We shall therefore refer without distinction to one or the other.

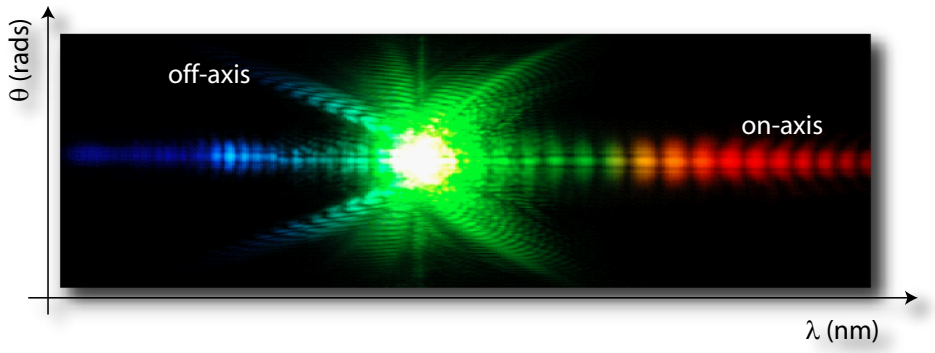

Fig. 3.8. Example of a measured far-field (θ, λ) spectrum. a 527 nm, 200 fs laser pulse has undergone filamentation in 5 cm of fused silica. The on-axis and off-axis components are indicated in the figure. The setup used is shown in Fig.3.6. The colors are real and were registered with a Nikon digital camera (D70).

etc.) it is possible to either fabricate our own imaging spectrometer using lens instead of toroidal mirrors or, alternatively, if you are really in a rush or short of optical components, a "poor mans" version may be obtained with just one lens and a glass prism. The layout is shown in Fig.3.7. The input beam is sent through a slit and then into the prism. The slit may be simply made from a piece of black paper with scissors: we do not want the slit to be too thin otherwise strong diffraction will severely reduce and blur the quality of the final spectrum. Although using a relatively wide slit will also reduce the resolution of the spectrum this is still better than having to cope with the slit diffraction pattern. The "far-field" lens is then simply placed directly after the prism and at a distance f from the lens we will have something similar to the (θ, λ) spectrum we would have from the imaging spectrometer. The vertical θ axis may be calibrated as before but the horizontal λ axis must be calibrated with more care (e.g. using a fiber-coupled spectrometer). In any case, even without calibration, this is a quick setup that will tell us a lot about the spectrum, for example the extent of the supercontinuum and the presence of red and/or blue shifted conical emission tails. An example were we may want to use such a setup at least at a preliminary stage is for measurements of optical filaments generated in air. Conical emission is not always visible in air filaments and sometimes appears only to be blue shifted with respect to the pump wavelength. Changing the input energy and focusing conditions will change the spectrum. Due to space limitations or other factors, a prism and a lens are much easier to move and realign over distances of 1-30 meters than the whole imaging spectrometer

setup. Furthermore the energies in such an experiment may be quite high ranging from a few to a few tens of milliJoules and we should be vary wary of sending such energies into our delicate (and costly) instruments. In any case energy in the pulse may be reduced by taking the reflection from one or more wedged glass plates as shown in Fig.3.7: this will also avoid any additional undesired nonlinear effects occurring within the glass prism.
In Fig.3.8 we show the (θ, λ) spectrum of a 527 nm, 200 fs, 3 μJ, laser pulse that has undergone filamentation in 5 cm of fused silica. The output of the imaging spectrometer was registered by removing the lens from a commercial digital camera (Nikon, D70) and placing the CCD directly in the output imaging plane. Using such a CCD has a number of advantages, such as the direct color information (if you are working in the visible range) with a certain aesthetic quality that is difficult to ignore, a logarithmic-like response so that the weaker features are readily visible and a reduced blooming in the saturated high-fluence zones. However if you are interested in performing quantitative fluence measurements then it is best to use scientific CCD cameras characterized by an accurate linear response, preferably with a 16 bit dynamic range in order to retain the visibility of the weaker features. Finally we note that in many cases it is extremely important to register only single-shot images. Averaging over many shots may give the impression of a greater readability of the weaker features but even small fluctuations in the input laser pulse energy may lead to large fluctuations in the output pulse profile. Therefore many of the features that we are now going to describe will be washed out by averaging over more than one laser pulse.
If we examine the spectrum we note straight away that there are two well distinguished features:

- a strong on-axis emission that extends over an extremely broad spectral range. This is usually referred to as the supercontinuum. We also note the well-defined interference fringes. Without going into too much detail here regarding the origin of the supercontinuum, the interference fringes may be interpreted as a result of pulse splitting [70]. Each split pulse carries a similar spectrum so that each spectral component at the spectrometer output is the superposition of two temporally shifted contributions, one from each pulse. The existence of such fringes tells us that the supercontinuum has a high temporal coherence and the fringe-spacing gives a direct measure of the temporal spacing between the split pulses, without having to perform any kind of correlation measurements. Pushing this idea a bit further, it is often possible to observe more than a single periodicity in the on-axis spectrum. Indeed multiple n periodicities will indicate the presence of n split pulses and the inverse of the periodicities will give the pulse temporal separations [70]

- a marked off-axis radiation, usually referred to as Conical Emission (CE). This part of the spectrum is clearly related to the conical-wave nature of the pulse and, as we will see, may provide a great amount of information on the filamentation process and on the spontaneous formation of the X waves. Other models have been proposed to explain CE. These may be divided into two groups depending on the main mechanism that is considered: Cerenkov-like emission [73, 74] and SPM in the presence of plasma defocusing [75, 76]. However these treat primarily the case of filaments in air, in which the CE is often only blue-shifted with respect to the pump pulse frequency and in the presence of strong plasma generation and neglect the role of dispersion. The X Wave model on the other hand establishes a strong link between the features of conical emission and the dispersion in the medium.

There is a further, very important property of (θ, λ) spectra of which we will make large use and that is the possibility, outlined in chapter 2, to derive the pulse group velocity directly from the measurement. A detailed recipe for this is as follows:

1. for each wavelength take the angle θ for which maximum intensity is observed
2. using the material Sellmeier (or similar) relations for $n(\omega)$ calculate $k = \omega n(\omega)/c$
3. find the longitudinal wavevector from $k_z = k\sqrt{1-\theta^2}$
4. the group velocity (along the propagation direction) may now be found from $v_g = d\omega/dk_z$

Care should be taken in deciding whether to use internal (i.e. within the material) or external angles. The measured spectrum will always give us the external angles as the Fourier lens is surrounded by air. Therefore, when deriving the group velocity of the pulse inside the sample the angles must be rescaled, $\theta = \theta(\lambda) = \theta_{\text{measured}}(\lambda)/n(\lambda)$.
Note that this method is very general and has nothing to do with conical waves. For example, a Gaussian pulse will give a maximum intensity angle of $\theta \sim 0$ for each frequency. Therefore this method will simply give us the material group velocity, $v_g = d\omega/dk$, as expected for a Gaussian pulse. In general this value will not be constant due to second or higher order dispersion so the peak velocity is usually identified with the group velocity calculated at the carrier frequency. In a similar fashion we can derive the group velocity of a tilted pulse and this will have a group velocity that is different from that of the Gaussian pulse (due to the pulse front tilt) but, similarly to the Gaussian pulse, it will suffer from dispersion.
If on the other hand our calculations gives us a group velocity that does not depend on frequency then we may conclude that the spectrum is that of a

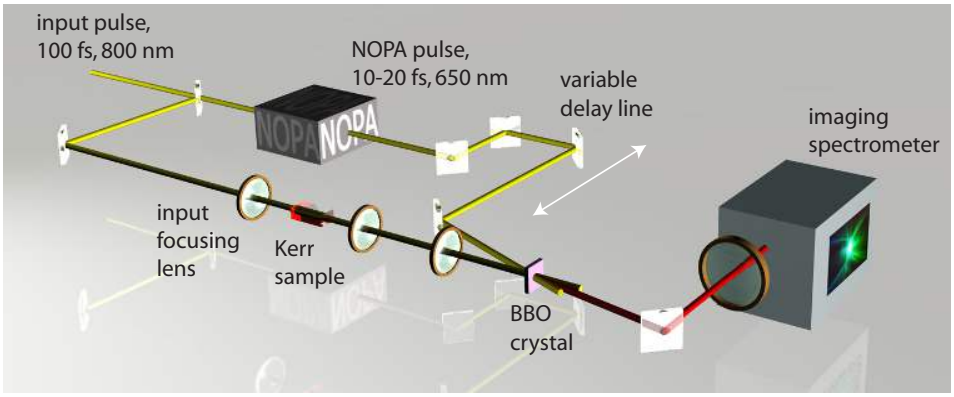

Fig. 3.9. Experimental layout for Gated Angular Spectrum (GAS) measurements.

stationary conical wave. If necessary we may now verify that the derived v_g value is correct by superimposing onto the measured spectrum the conical wave relation[3]

$$\theta = n(\lambda)\sqrt{\left[\frac{2\pi n(\lambda)}{\lambda}\right]^2 - k_z^2} \quad \text{with} \quad k_z = \frac{2\pi n(\lambda_0)}{\lambda_0} + \frac{1}{v_g}\left(\frac{2\pi c}{\lambda} - \frac{2\pi c}{\lambda_0}\right),$$

where λ_0 is the input pump wavelength.

3.3 Gated Angular Spectrum Measurements

In the previous section we showed how to measure the far-field (θ, λ) spectrum of a laser pulse. However we may want more. We may want to know for example exactly how the various frequencies are distributed inside our pulse as this would give us some insight into the underlying physical mechanisms that led to their formation. One possible approach would be to characterize the full 3D intensity and phase profile of the pulse and indeed such information would give us complete access to any physical quantity regarding the pulse shape that we may desire. Some recent progress has been made in characterizing the 3D patterns of laser pulses but the measurements are not always simple and become less so as the pulse becomes more complicated. Here we shall show how it is possible to retrieve temporally resolved spectra

[3] Note that, written in this form, the relation will give "external" angles (in air) as these are the angles that should be directly compared with the measurements.

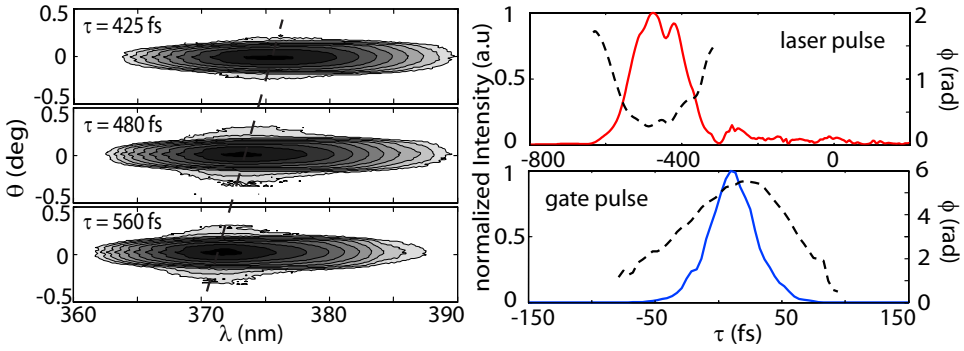

Fig. 3.10. GAS characterization of a 100 fs laser pulse. The left graphs show the measured (θ, λ) spectra for three different delays (between the laser and gate pulses). The dashed line shows the variation of the pulse frequency of delay, also known as first order chirp. The right hand graphs show the on-axis ($\theta = 0$) intensity (solid line) and phase (dashed line) profiles calculated using the FROG algorithm applied to the GAS data. The quadratic phase variation of the laser pulse confirms the pulse chirp measured directly by the GAS.

without the need to resort to phase measurements.

In Fig.3.9 we show the experimental layout for the so-called Gated Angular Spectrum (GAS) measurements. This layout is a mixture between the 3D mapping layout shown in Fig.3.2 and the (θ, λ) measurement. The idea is very simple: using the same setup as for 3D mapping we now remove the final imaging optics and instead use a lens to produce the spatial far field. This is then sent into the imaging spectrometer. The final result is a time resolved (θ, λ) spectrum that is reconstructed by simply changing the relative delay τ between the laser and the gate pulses and registering the (θ, λ) spectrum for each τ [77]. In the next chapter we shall see some measurements of optical filaments characterized using this technique and we shall see how the results give a clear connection between the on-axis and off-axis parts of the spectrum.

The measurement as described above is clearly very similar to FROG measurements only now we are measuring the full (θ, λ) spectrum at each delay and not just the frequency spectrum. Indeed, if we take only the data for $\theta = 0$ we may use the standard FROG retrieval algorithm and obtain the pulse phase profile at $r = 0$. Alternatively we could perform this last measurement but this time placing the "far-field" lens so that the spectrometer is now placed in the lens imaging plane, i.e. so as to measure the (r, λ) spectrum at each τ. By applying the FROG algorithm at different r we can obtain the *relative* phase profile at each r. However this is not sufficient

to reconstruct the full 3D phase profile due to the fact that we have no connection between the phases of different r slices. In other words we are missing the information that tells us how the phases at each r are related to each other. Nevertheless a great amount of information is already available in the GAS measurement and knowledge of the full space-time phase profile is not always necessary. We shall see in the next chapter an example of the GAS technique applied to a complicated laser pulse but as a simple example let us first look at the information that the GAS techniques gives us when applied to our laser pulse, just at the output of our laser. So the setup is basically the same as in Fig.3.9 but we have now removed the nonlinear Kerr medium. The results are shown in Fig.3.10. The left graphs show the (θ, λ) spectra as directly measured at the spectrometer output using a 16 bit CCD camera (Andor). Note that the wavelengths are centered around 370 nm: this is due to the fact that the laser pulse was centered at 800 nm, the gate pulse at 650 nm, so that the sum-frequency signal generated is in the ultraviolet region. The figure shows the spectra for three different relative delays between the laser pulse and the gate pulse. The first thing we note is a shift of the central frequency toward shorter wavelengths as the delay increases, i.e. the laser pulse has red-shifted wavelengths on the leading edge and blue shifted wavelengths on the trailing edge, indicating that our pulse is chirped. Our data also shows that the frequency varies linearly with delay so that we may assume that the dominant phase distortion is quadratic. In other words, if we assume the pulse has a Gaussian profile we may write the pulse phase terms as

$$e^{j\phi} = e^{-(1+j\alpha)t^2/\sigma_\tau^2} e^{-j(kz-\omega t)}, \tag{3.3}$$

where α is the chirp parameter. The instantaneous frequency of the pulse is then given by

$$\omega = \frac{d\phi}{d\tau} = \omega_0 - 2\alpha \frac{\tau}{\sigma_\tau^2}. \tag{3.4}$$

We thus obtain a relation for the chirp parameter

$$\alpha = \frac{\Delta\omega}{\Delta\tau} \frac{\sigma_\tau^2}{2}. \tag{3.5}$$

Using this last relation we evaluate α from Fig.3.10 as $\alpha = -1.39$. We may verify this result by performing a FROG measurement of the central part of the pulse. Actually the data already contains the information necessary for FROG phase retrieval if we consider only the central portion, around $\theta = 0$, of the pulse. The right hand graphs show the the retrieved intensity and phase profiles of both the laser and the gate pulses. As can be seen the phase of the laser pulse indeed shows a strong quadratic variation and the chirp parameter obtained by fitting this curve is $\alpha = -1.04$. The value

we obtained directly from the measurement is close to the FROG value yet there is a certain discrepancy. This is due to the fact that the gate pulse also has a very strong linear chirp and, although the pulse is much shorter than the laser pulse, only the FROG algorithm is able to retrieve in this case the true quantitative value. However the important feature of the GAS technique is not a quantitative analysis of pulse chirp along a certain portion of the pulse. As we have seen FROG is much better for this. We shall see in the next chapter that the GAS technique becomes really interesting when the pulse suffers from strong spatio-temporal coupling and therefore exhibits strong variations of the pulse shape and spectrum at different transverse spatial positions. FROG results in this case become questionable or in any case have a limited value.
As a final note we underline that gated spectral characterization of ultrashort laser pulses, i.e. characterization of the spectrum associated to specific time slices or temporal features in the wave-packet near-field, is a technique used in some numerical studies of super-continuum generated in optical fibers. An excellent review of this is given in ref.[78]. However to the best of our knowledge this technique has only been applied numerically and, more importantly, only the temporal spectrum is considered. This is due to the fact that all spatial effects are eliminated due to fiber guiding that imposes a certain transverse profile on the beams and that is not subject to (significant) modification even in the presence of large nonlinearities.

3.4 Measuring the coherence volume

As a last example of use of the imaging spectrometer let us consider the problem of measuring the coherence volume of a given pulse. The coherence properties of our laser pulse or in general of our light source are extremely important and lie at the basis of many applications. A detailed treatise of the statistical properties of light may be found in Refs.[79] and [80] while Ref.[81] gives a condensed yet complete and precise description of coherence properties.
Intuitively we understand coherence as the ability of our light beam to superimpose with a replica of itself and produce interference fringes. We can do this either in the (transverse) spatial domain and speak of spatial coherence or in the temporal domain, and speak of temporal coherence. However the coherence of a light source is actually a statistical property. That means that when we give a coherence time or size for our light source this refers to an average property of the light. A correct definition of (first order) coherence in terms of ensemble averages: the temporal coherence it is the half-width of the first-order correlation function of the electric field with mean frequency $\langle\omega\rangle$, $E(\boldsymbol{r},t) = A(\boldsymbol{r},t)\exp(j\langle\omega\rangle t - \phi(\boldsymbol{r},t))$ [81]

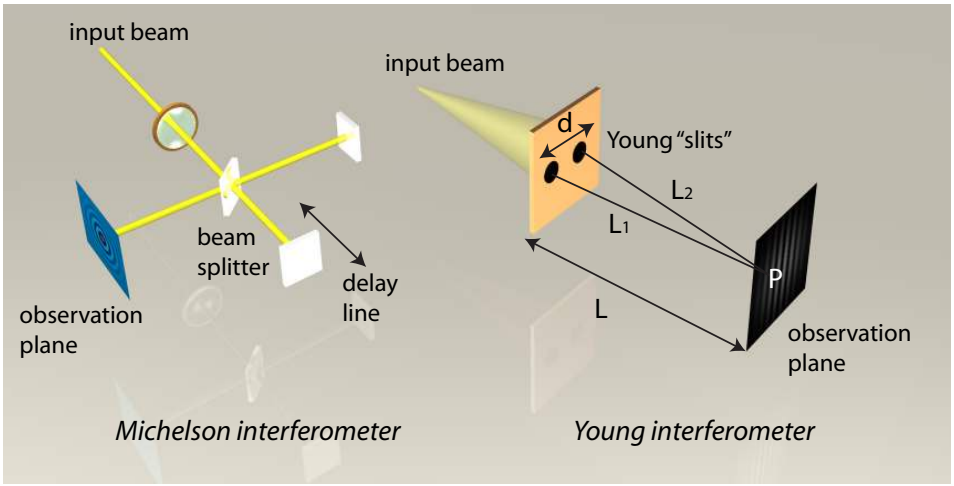

Fig. 3.11. Schematic layout of the Michelson and Young interferometers. In the Michelson interferometer coherence is tested by changing the temporal delay between the two interferometer arms. In the Young interferometer spatial coherence is tested by changing the distance d between the two slits.

$$\Gamma = \langle E(\boldsymbol{r}_1, t_1) E^*(\boldsymbol{r}_2, t_2) \rangle, \tag{3.6}$$

where the brackets "$\langle\rangle$" indicate the average over many replicas of the system (ensemble average). Eq.3.6 defines what is usually referred to as the mutual coherence function in the sense that it describes the coherence as a simultaneous function of both $\boldsymbol{r}$ and t and these may take any arbitrary value. We should therefore measure Γ and then we will be able to define the coherence volume $(\boldsymbol{r}, t)$ of our light source by taking the width at some point of the function e.g. at half maximum or $1/e$. Recalling that coherence manifests itself through interference the most common approach is to resort to some version of one of the two most famous interferometers, the Michelson and the Young interferometer (see Fig.3.11). Let us consider the case of the Young interferometer. In general we may normalize the correlation function Γ so as to obtain the so-called complex degree of coherence [4]

$$\gamma = \frac{\langle E(\boldsymbol{r}_1, t+\tau) E^*(\boldsymbol{r}_2, t) \rangle}{\sqrt{\langle E(\boldsymbol{r}_1, t) E^*(\boldsymbol{r}_1, t) \rangle \langle E(\boldsymbol{r}_2, t) E^*(\boldsymbol{r}_2, t) \rangle}} \tag{3.7}$$

[4] we substitute t_1 and t_2 with $t+\tau$ and t, i.e. we assume that the ensemble average depends only on the time difference τ and not on the actual time t. This is true for all those light fields that are stationary, i.e. their ensemble average is independent of time. Examples are a CW thermal light source or a laser that does not have amplitude fluctuations in time.

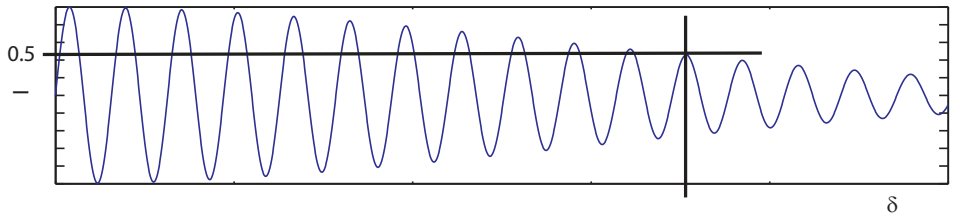

Fig. 3.12. Interference pattern intensity as a function of the generic variable δ, i.e. either the temporal delay τ in the Michelson interferometer or the spatial offset d between the Young slits.

and $\Gamma = \gamma\sqrt{\langle I(\boldsymbol{r}_1, t+\tau)\rangle\langle I(\boldsymbol{r}_2, t)\rangle}$. The electric field at a point P on the observation plane will be given by

$$E(\boldsymbol{r}_P, t) = a_1 E(\boldsymbol{r}_1, t+\tau) + a_2 E(\boldsymbol{r}_2, t), \tag{3.8}$$

where a_1 and a_2 account for the different field amplitudes due to diffraction from the slits placed at different points P_1 and P_2 and the time delay $\tau = L_2/c - L_1/c$. By taking the intensity at point P we find that the maximum and minimum values we expect to find are given by

$$I_{max} = \langle I_1\rangle + \langle I_2\rangle + 2\sqrt{\langle I_1\rangle\langle I_2\rangle}|\gamma|, \tag{3.9}$$

$$I_{min} = \langle I_1\rangle + \langle I_2\rangle - 2\sqrt{\langle I_1\rangle\langle I_2\rangle}|\gamma|. \tag{3.10}$$

In other words we will find an oscillating intensity distribution in the observation plane with max and min values given by these relations. The fringe visibility is thus given by

$$V_P = \frac{I_{max} - I_{min}}{I_{max} + I_{min}} = \frac{2\sqrt{\langle I_1\rangle\langle I_2\rangle}}{\langle I_1\rangle + \langle I_2\rangle}|\gamma(\boldsymbol{r}_1, \boldsymbol{r}_2, \tau)|. \tag{3.11}$$

This equation tells us that we may directly measure the mutual coherence of our light source with a Young interferometer by measuring the fringe visibility of the interference pattern. By moving the observation point P we are changing τ, i.e. we are gathering information about the temporal degree of coherence, and by varying $\boldsymbol{r}_1$ and $\boldsymbol{r}_2$ or the relative separation between the two slits we extend the information gathered also to the transverse spatial coordinate. So we have a conceptually very simple manner to measure γ. However the actual experimental implementation of this idea would be extremely tedious and difficult to perform accurately, mainly for two reasons:

1. in order to observe the interference pattern we will place the observation plane at a certain distance L from the slits and, due to the relatively fast

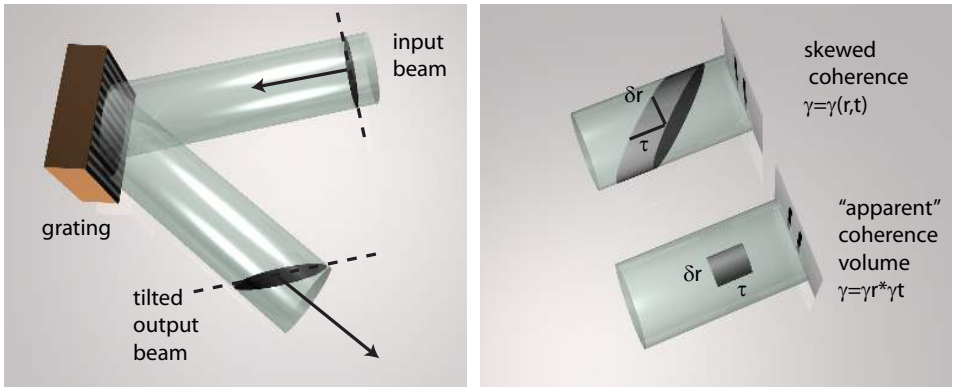

Fig. 3.13. Practical example of skewed coherence generated by reflection from a grating.

decay of light intensity moving away from the slits we will usually be in a situation such that $P << L$. Furthermore the separation d between the slits will typically be small in order to guarantee that we remain within the beam transverse dimension and that the diffraction patterns overlap on the observation screen. This implies that the maximum delay τ that we will be able to examine with this method will be of the order of $\tau \sim Pd/Lc$. For example if $d = 10$ μm, $L = 0.5$ cm and $P_{max} \sim 5$ mm then τ is limited to ~ 30 fs. This may prove to be acceptable for some cases (e.g. a light bulb has a coherence time of the order of 10 fs) but for many others it will be a strong limitation

2. the second issue is related to spatial characterization as Eq.3.11 tells us that we must repeat our measurements for many different values of $\boldsymbol{r}_1$ and $\boldsymbol{r}_2$. This implies having many different samples of slits, all with identical apertures but placed in different positions and repeating the measurement with each of these. Furthermore, the slits with a wider relative separation will require shifting the observation plane further away in order for the diffraction patterns from the two slits to overlap. This in turn leads to both a reduction in the overall intensity and a further limitation in both the the spatial and temporal interval over which the measurement is significant.

For these reasons among others, it is common to limit diagnostics to the temporal or the spatial domains separately. In other words we can measure the spatial degree of coherence by taking $L_2 = L_1$ and recording the intensity as a function of the slit separation or, equivalently, measure the temporal degree of coherence by using a Michelson interferometer and recording the intensity as a function of the temporal delay. Taking the widths at half

maximum of the envelopes of these two measurements will give us the spatial, γ_r, and temporal, γ_t, coherence values, respectively. The coherence volume could then be naively taken as the product $\gamma = \gamma_r \cdot \gamma_t$. However this last step is correct only if our light source is such that there is no space-time coupling, i.e. there is no dependence of the (ensemble averaged) temporal profile on the transverse spatial position. This is indeed true in many cases but a very simple example in which is not true is a white light or broadband source that has been reflected from a grating (see Fig.3.13). The pulse front will become tilted upon reflection from the grating so that the coherence volume will become skewed in space-time coordinates. Trying to measure the temporal coherence with a Michelson interferometer and the spatial coherence with a Young interferometer, in other words treating space and time separately, will lead to a coherence function $\gamma(\boldsymbol{r}, t)$ that is not skewed and considerably smaller than the true function. Note that in general the Young interferometer is able to distinguish between the two cases of a cylindrical-like coherence volume and a skewed volume. In the former case the interference maximum P will be along the slit axis while in the latter case it will be shifted at an angle. Referring to Fig.3.14, this may easily be seen by evaluating the interference maximum position as the point P for which the optical path difference ΔL goes to zero. We consider two cases, one in which the wave fronts are tilted at an angle θ and another in which we simply have plane waves propagating at an angle θ with respect to the slit axis:

$$\Delta L_{tilt} = L_2 - L_1 - d\tan(\theta),$$
$$\Delta L_{angled} = L_2 - L_1 - d\sin(\theta).$$

So for example, if L = 20 mm, d = 30 μm and $\theta = 0$ deg then we will obviously have maximum interference at $x = 0$ on the observation plane. But if $\theta = 30$ deg, the tilted wave will give a maximum at $x = 14$ mm. However some confusion may arise due to the fact that a measured value of $x = 14$ mm is also compatible with the interference maximum expected for a simple plane wave incident (with no tilt) at a $\theta = 35$ deg angle with respect to the slit axis. So the Young interferometer will not be able to actually distinguish between these two cases unless a full coherence volume measurement is performed.

The Wiener-Khintchine Theorem

Let us now consider a system that is stationary, i.e. the amplitude of the function $f(t)$ does not change with time and is ergodic, i.e. such that the ensemble average may be substituted by a temporal average

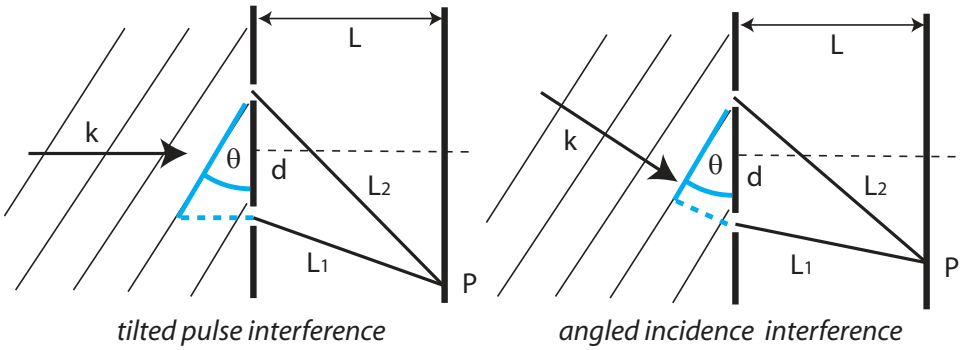

Fig. 3.14. Young interference scheme for tilted waves and angled incidence of plane waves.

$$\langle f(t)\rangle = \lim_{T\to\infty}\frac{1}{T}\int_{-T/2}^{+T/2} f(t)dt. \tag{3.12}$$

In other words, the replicas of our system are obtained by integrating in time due to the fact that the system itself evolves in such a way as to spontaneously cover all possible replicas. Under such conditions the temporal autocorrelation function, defined as

$$\tilde{\Gamma}(\tau) = \lim_{T\to\infty}\frac{1}{T}\int_{-T/2}^{+T/2} f(t+\tau)f(t)dt. \tag{3.13}$$

is equal to the autocorrelation function $\Gamma(\tau)$, i.e. the time autocorrelation functions of all sample functions are equal to each other and are also equal to the statistical autocorrelation function. It is therefore pointless to distinguish between the two autocorrelation functions for such processes. We may now introduce the Wiener-Kintchine theorem that states simply that the autocorrelation function and the power spectral density S form a Fourier Transform pair ([80]). Here the spectral power density is understood as defined for a random process

$$S(\omega) = \lim_{T\to\infty}\frac{\langle f(\omega)f^*(\omega)\rangle}{T}. \tag{3.14}$$

Therefore, taking the function f as the electric field, the Wiener-Kintchine theorem tells us that the correlation function Γ is obtained from the Fourier transform of the *ensemble averaged* spectral density:

$$\Gamma(\tau) = FT[\langle S(\omega)\rangle]. \tag{3.15}$$

This relation may be generalized to include also the spatial variable x and taking the two-dimensional $(k_\perp, \omega)$ Fourier transform

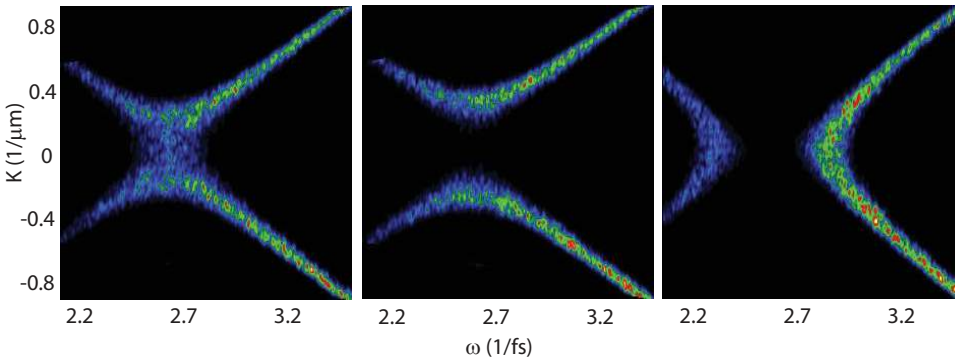

Fig. 3.15. Experimentally measured super-fluorescence spectra (converted from (θ, λ) to $(k_\perp, \omega)$) generated in a BBO crystal with the setup shown in Fig.3.16, for three slightly different phase-matching conditions.

$$\Gamma(x, \tau) = FT[\langle S(k_\perp, \omega)\rangle]. \tag{3.16}$$

In other words, we may recover the correlation function by measuring the $(k_\perp, \omega)$ spectrum averaged over many replicas of our system (e.g. over many pulses for a pulsed laser). We may therefore combine the (θ, λ) measurement as described above with the analysis suggested by the two-dimensional generalization of the Wiener-Kintchine theorem so that we have an extremely efficient and non-ambiguous coherence volume measurement technique. In order to prove the validity of this measurement technique we show a characterization of the coherence volume of the so called super-fluorescence signal generated via parametric down conversion in a crystal with second order nonlinearity ([82]).

Super-fluorescence coherence

Super-fluorescence is a spontaneous manifestation of parametric down conversion that is observed in crystals with large second order nonlinearity ($\chi^{(2)}$) such as Beta-Barium-Borate (BBO) or Lithium Triborate (LBO). By pumping with an intense laser pulse with frequency ω a wide-bandwidth signal is produced around $\omega/2$. This signal is typically observed as colored conical emission so that different frequencies are emitted at different angles with angles and frequencies depending on the specific phase-matching conditions in the crystal (see for example Ref.[83] for more details on this topic). The intensity distribution follows the phase-matching curves which in turn are determined by the material dispersion properties. Indeed the parametric gain is described by $\exp(2g(k_\perp, \Delta\omega)z)$. Within the slowly-varying envelope approximation, the growth rate reduces to

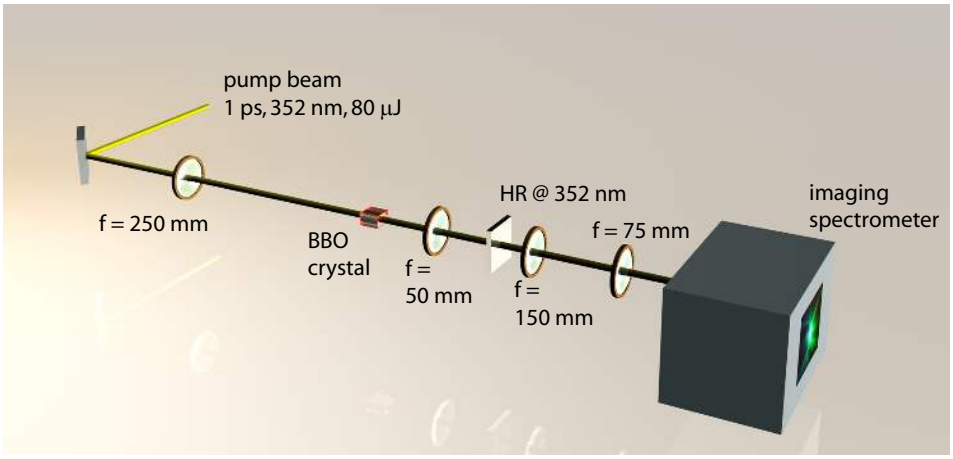

Fig. 3.16. Experimental layout used to measure the (θ, λ) spectrum of the super-fluorescence generated in a BBO crystal pumped by a 352 nm pulse.

$g(k_\perp, \Delta\omega) = (\sigma^2/4k_0^2 - (k''\Delta\omega^2/2 - k_\perp/2k_0)^2)^{1/2}$ ([82]) so that the spectrum exhibits a hyperbolic structure, i.e., the locus (θ, λ) of the peak gain is X-shaped. In Fig.3.15 we show three different measurements of the super-fluorescence (θ, λ) spectrum generated in LBO in three different phase-matching conditions (controlled by the crystal temperature). As expected the intensity is distributed along X-shaped curves. Also note how the spectra show a marked speckle pattern. This is a result of the parametric amplification generating the super-fluorescence signal by which a signal at ω generates so-called signal and idler waves at $\omega/2 + \delta\omega$ and $\omega/2 - \delta\omega$, respectively. The initial seed for the signal idler waves is given by zero-point quantum fluctuations and the speckle pattern is a direct manifestation of the random phases that characterize the quantum noise. In other words the super-fluorescence signal appears to be made of many different "modes" each with a different phase. In a similar fashion the white light emitted from a light bulb is considered as composed of many temporal modes with temporal coherence of the order of 10 fs that may be measured with a Michelson interferometer.

Following the recipe dictated by the Wiener-Kintchine theorem we use the setup shown in Fig.3.16 to measure the super-fluorescence (θ, λ) spectrum which is averaged over many pulse shots (the ensemble average). The result of this measurement is shown in Fig.3.17. By taking the two-dimensional Fourier transform we obtain the coherence volume that is clearly X-shaped, i.e. skewed along non-trivial space-time trajectories [82]. The far-right panel in Fig.3.17 also shows the experimental intensity pattern obtained by measuring the interference from the same field but with a double-slit Young interferometer. As described above, the skewed coherence trajectories lead

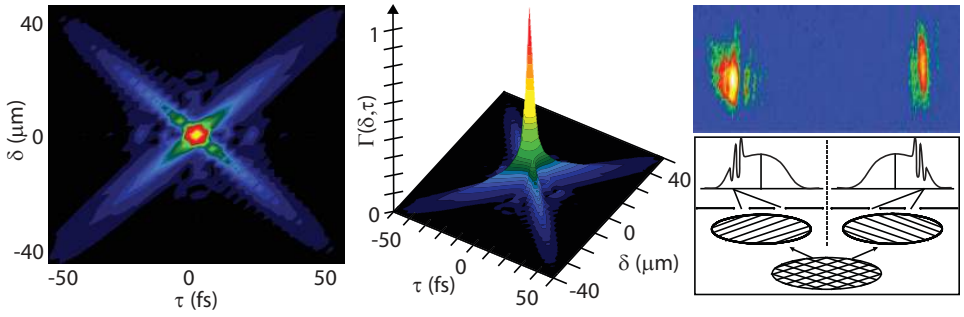

Fig. 3.17. Correlation function measurement of BBO super-fluorescence generated and measured using the setup in Fig.3.16. the central and far-left panels are different representations of the same X-shaped correlation function. The far-right panel shows the super-fluorescence pulse characterized using a Young interferometer: the two off-axis interference peaks, indicating skewed coherence, are clearly visible.

to the appearance of off-axis interference peaks but no further information, such as the actual shape of the correlation function, may be determined from this single Young measurement.
Let us stress the general relevance of X shaped coherence by underlining that it constitutes the natural state of coherence for all nonlinear systems whose governing equations exhibit a space-time hyperbolic structure. X-coherence is thus expected to arise in any multidimensional optical system involving nonlinear wave propagation in normal dispersion. A typical example is the modulational instability of plane waves propagating in cubic, $\chi^{(3)}$, nonlinear Kerr media (see Fig.1.3).

3.5 Seeing the light

In all the experimental layouts shown in these pages the final experimentally relevant quantity is recorded on some kind of two dimensional imaging hardware, basically a two dimensional array of photodetectors. Indeed the experiments described in this chapter are the result of the search to find the best way to visualize information of the laser pulse, that is an intrinsically three dimensional, projected onto the two dimensions of the photodetector array. Furthermore the photodetector array will transform the light wave into an electric signal which will then be processed by standard electronics and therefore lead to a serious limitation to the shortest temporal event that may be directly revealed. A fast single photodetector may have a response time of about 100-10 ps but for a two dimensional array we will be lim-

ited to the 1 ms range, in the best case. We have already seen that these limitations may be circumvented by using gated measurements in which it is the light pulse itself that determines the temporal resolution but in any case the photodetector will not measure directly the intensity profile, i.e. the instantaneous space-time energy content, of an ultrashort laser pulse. Here we will briefly overview the information that our photodetector array will give us and how we should choose the instrument in order to optimize this information.

3.5.1 CCD and CMOS cameras

Two dimensional photodetector arrays are commonly available in the form of Charge-Coupled Devices (CCD's) or Complementary Metal-Oxide Semiconductor (CMOS) arrays. Both devices perform the basic operation of transforming light signals into electronic signals. The incoming photons are absorbed by the sensor and the energy is then released in the form of electric charge. The main difference between the two sensors is the way in which the electric charge is then read from the array. A CCD transports the charge across the chip and reads it at one corner of the array. An analog-to-digital converter (ADC) then turns each pixel's value into a digital value by measuring the amount of charge at each photo-site and converting that measurement to binary form. On the other hand CMOS devices use several transistors at each pixel to amplify and move the charge using traditional wires. The CMOS signal is digital, so it needs no ADC. Due to technological limitations these differences lead to some practical issues:
1) CCD sensors create high-quality, low-noise images. CMOS sensors are generally more susceptible to noise.
2) Because each pixel on a CMOS sensor has several transistors located next to it, the light sensitivity of a CMOS chip is lower. Many of the photons hit the transistors instead of the photodiode.
3) CMOS sensors traditionally consume little power and roughly 100 times less than conventional CCDs.
4) CCD sensors have been mass produced for a longer period of time, the technology is more advanced and cheaper. They therefore tend to have higher quality pixels, and more of them.
Even if CCDs are by far the most widespread sensors, it is quite common to find CMOS technology applied to the sensors used in commercial digital cameras and that therefore make the most of a much longer battery life. Furthermore mass production has concentrated solely on a single material platform, silicon. Silicon is the preferred material for the microprocessor industry and this is the main reason for the excellent quality of silicon-based CCD sensors. Fortunately the silicon absorption band-gap is located around 1000 nm so that all higher energy (shorter wavelength) photons will

be absorbed and transformed into electrons. The sensitivity at 400-700 nm wavelengths is usually quite high but some applications require high sensitivity in the infrared region where silicon is transparent. Other materials must therefore be used, Aluminum-Gallium Arsenide (AlGaAs) for example guarantees high sensitivity in the 1000-1700 nm range. Using such materials in turn implies that there is no longer any technological advantage in the CCD configuration and indeed these infrared detectors are typically CMOS.

3.5.2 Color

The single pixels that make up our CCD or CMOS array are color blind. All they do is simply count the number of (photo-)electrons generated by the absorbed photons. Color information must therefore be obtained by separating light into its three major red, green and blue (RGB) components, for example with a prism or selective filters, and then using a separate sensor for each of the three color channels. Note that standard color emulsion films convey color information in this same way: the film is composed of three different layers, each one sensitive only to one of the three RGB channels. Alternatively a much cheaper approach may adopted by which the sensor is only one but each single pixel is covered by a wavelength selective filter so that the pixels are sensitive exclusively only to red, green or blue light. The most common pattern of filters is the "Bayer" filter pattern. This pattern alternates a row of red and green filters with a row of blue and green filters. Therefore the pixels are not evenly divided and there are as many green pixels as there are blue and red combined. This is because the human eye is not equally sensitive to all three colors and it is necessary to include more information from the green pixels in order to create an image that the eye will perceive as a true color.

3.5.3 Energy measurement

The color CCD's considered in the previous section suffer from a severe limitation due to the fact that the color response imposed on the sensor is studied in order to mimic the color responsivity of the human eye. The response will therefore typically be strongly nonlinear with a logarithmic-like dependence of the output current on the incident light fluence and maximum sensitivity at green wavelengths. This may represent a serious problem if quantitative energy measurements are to be made. In this case a scientific CCD with linear response should be used. Such cameras may exhibit a direct proportionality between incident light fluence and generated photoelectrons with a large 16 bit dynamic range and are ideal for many applications. However care must still be taken in comparing experimental and numerical spectra.

Photo-counts and fluence

The single photo-sites or pixels of our CCD will give a direct indication of the total number of photons in our beam. A pixel with 100% conversion efficiency will convert every single photon with an energy $\hbar\omega$ that lies above the material band-gap (e.g. 1.1 eV for silicon) into an electron. These electrons are often referred to as photoelectrons in order to distinguish them from thermal electrons, that is electrons that are generated by thermal fluctuations and are thus a source of noise and not correlated in any way to the optical beam we are measuring. However the photoelectron does not carry any information regarding the actual energy of the optical photon that generated it and we should therefore bear in mind that the quantity we are actually measuring with our CCD is not directly the beam fluence (time-integrated intensity). This is usually of little importance but if we perform spectral measurements and we really are interested in the fluence distribution then we should multiply the photo-count distribution by $\hbar\omega = \hbar 2\pi c/\lambda$. So this will give a variation along the λ axis of the measured signal that in many cases (e.g. large spectral extent) may become important.
Note also that in this discussion we assumed a 100% quantum efficiency (conversion efficiency from photons to electrons) at all wavelengths. This was just an approximation in order to simplify the discussion but we must now bear in mind that typical silicon CCD responsivities are peaked around 700 nm with maximum values of the order of 80-90%. This value decreases smoothly to about 10% around 300 nm and more abruptly to zero at 1100 nm. Each CCD will have a specific quantum efficiency curve that depends on construction details and the actual fluence values are retrieved only after normalizing for this specific curve.

Coordinate transformation

Most of the experimental methods described in this chapter are based on (θ, λ) measurements and so far we have always assumed that the information contained in the $(k_\perp, \omega)$ spectrum is identical to that contained in the (θ, λ) spectrum. This is indeed true however there may be cases in which we may want to compare at a quantitative level the numerically simulated spectra, that will typically be in $(k_\perp, \omega)$ coordinates, with experimental spectra, that will typically be in (θ, λ) coordinates. The axes of these spectra are related by the simple relations $k_\perp = \theta k$ and $\omega = 2\pi c/\lambda$. However care should be taken in accounting for how the spectral power. The total energy contained in the spectrum is given by

$$E = \iint S(k_\perp, \omega) dk_\perp d\omega = \iint S(\theta, \lambda) d\theta d\lambda. \tag{3.17}$$

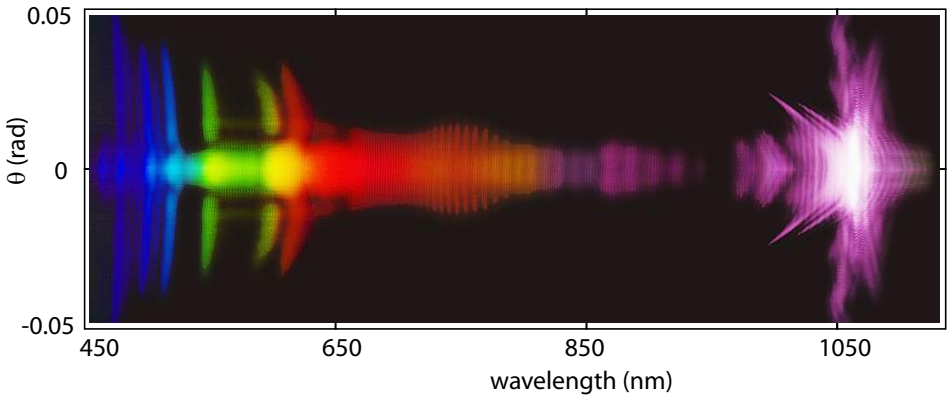

Fig. 3.18. Experimentally measured (θ, λ) to $(k_\perp, \omega)$ spectrum of a filament generated from a 1055 nm input pump and recorded with a modified (extended spectral range) digital photocamera (Nikon D70). The input energy was 40 μJ and the Kerr medium was a 15 cm bar of fused silica.

Using the relations to transform from $k_\perp, \omega$ to θ, λ we find

$$\begin{aligned}\iint S(k_\perp,\omega)dk_\perp d\omega &= \iint S(k_\perp,\omega)\frac{2\pi}{\lambda}d\theta\frac{2\pi c}{\lambda^2}d\lambda \\ &= \iint S(k_\perp,\omega)\frac{\omega^3}{2\pi c^2}d\theta d\lambda \\ &= \iint S(\theta,\lambda)d\theta d\lambda \\ \Rightarrow S(\theta,\lambda) &= S(k_\perp,\omega)\frac{\omega^3}{2\pi c^2}. \end{aligned} \tag{3.18}$$

So we see that the fluence should be multiplied by ω^3 in passing to (θ, λ) coordinates.
In conclusion, when comparing experimental (θ, λ) measurements (recorded with a CCD) with numerically calculated $(k_\perp, \omega)$ spectra three different correction factors must be accounted for: i) renormalization to the quantum efficiency curve of the CCD camera to account for non uniform spectral sensitivity, ii) the transformation of photo-counts into fluence (that scales as $1/\lambda$ or ω) and, iii) the rescaling induced by the change of coordinates (that scales as ω^3).

3.5.4 Digital camera or "scientific" CCD?

So the question arises, should we use a linear-response scientific CCD or a reflex digital camera? The answer clearly depends on the final use we

intend to make of our data. Quantitative comparison of the spectral power density between numerically simulated spectra and measurements (or even between different measurements) requires use of a linearized CCD. However we may often be interested more on the *shape* of the spectrum in (θ, λ) space rather than in the actual value of the spectral power. In this case using a more common digital camera does have some positive aspects. We briefly comment on some of these issues:

- Linearized silicon CCD cameras are purposely studied for scientific applications. The responsivity or quantum efficiency is usually high and may reach typical values of the order of 80% or more in the 700-800 nm range. For certain applications with low light levels higher responsivities may be required and are obtained using so called back-illuminated sensors. These differ from standard CCD chips in that the incoming light under measurement arrives on the sensor from the rear side, i.e. opposite to that where the electronic wiring resides. The silicon chip is thinned down so that the generated photoelectrons are still collected by the electronics. Note that although efficiencies of the order of 95% or more may be attained with such cameras it is important to ensure that the thinned CCD chip is treated in order to avoid annoying Fabry-Perot cavity effects between the front and rear silicon faces. This effect will be more important at wavelengths that depend on the actual thickness of the silicon chip but usually manifests itself in the 700-1000 nm range.
  Digital cameras on the other hand typically have a much lower quantum efficiency, in the order of 10-40%. Furthermore the camera response is not linear but logarithmic-like. The response is purposely studied so as to mimic to a certain extent the logarithmic response of the human eye and that of standard emulsion films used in photography. For the same reason the peak sensitivity of these cameras is centered at green wavelengths, close to 500 nm.
- This brings us to the issue of color. Although color information is often superfluous in scientific measurements we cannot avoid the fact that the world is colored: by adding color to our data, although this may be repetition of data that is already present (if we are using a spectrometer) we are effectively adding an extra dimension to our graph. However care must be taken. We have already pointed out that color digital cameras are studied so as to reproduce colors as seen by the eye and this implies that the sensitivity of the CCD chip is artificially limited so as to be relatively insensitive to the near-infrared (700-1100 nm) range. This is rather unfortunate as most common lasers are operated at 800 nm. However a very simple cure for this problem is available: the spectral range is actually limited by a simple filter that is placed on top of the CCD chip by the manufacturer. By taking the camera apart this filter may be

easily removed and substituted with a clear fused silica plate thus restoring the full spectral range up to 1100 nm. From personal experience I can say that this operation is most easily done with Nikon cameras as the filter is removed by releasing four screws. The same operation with Canon cameras is slightly more messy due to the fact that the filter is glued on. Detailed instructions and the possibility to buy the substitute clear glass window (or even have this done for you) may be found at http://www.lifepixel.com.

- Blooming is the technical term used to describe the spilling of photoelectrons from highly saturated photo-sites to surrounding pixels. Therefore highly saturated areas in the image will bloom and the saturation, seen as a completely white spot, will spread and cover areas of the image that would otherwise contain useful information. This problem is partly solved and greatly reduced in commercial color cameras by creating an inactive region around each pixel that will collect and drain the excess photoelectrons. Professional CCD dealers (e.g. Kodak) will give a specification to the amount of blooming suppression which may even be of the order of 8 bits.
- Last but not least one should finally decide what to use also based on the available budget. A good 16 bit dynamic range, cooled scientific CCD camera with a relatively large $\sim$1x3 cm^2 chip will cost something in the 15000 euro range (complete with imaging software). A professional color CCD back, with a much larger 2x3 cm^2 chip, 16 bit dynamic range can be bought for roughly the same money. The advantages of the scientific CCD are that these CCD's usually come ready to be attached to your spectrometer, they are linear and have a higher sensitivity. On the down side you have no color information, bad blooming effects and a smaller chip. A good compromise is to have both a scientific CCD and a less expensive prosumer digital camera such as the Nikon D200 or D80 (Canon and other brands have similar cameras) that costs less than 2000 euro. The chip size is about 1.6x2.4 cm and dynamic range is 8-12 bits (depending on how you save the image) but the quality and ease of use is still excellent. All spectra shown in these pages were taken either with a 16 bit Andor DV420 (scientific CCD) or with Nikon D70 (color digital camera). An example of the kind of spectrum that can be registered using a Nikon D70 (with extended spectral sensitivity) is shown in Fig.3.18. The input pump was a 1 ps, 1055 nm wavelength pulse forming a filament in 15 cm of fused silica. The formation of X waves at the pump wavelength can be clearly seen along with the huge spectral extension into the 400 nm region. The conical (off-axis) features in the 600-400 nm region correspond each to a different X wave generated through multiple splitting events (here a total of 6 can be observed).

This concludes that chapter on diagnostics and measurement techniques. In the next chapters these will be used to study the details of ultrashort laser pulse filamentation dynamics.

4

Modeling filamentation and conical wave propagation.

This chapter is dedicated to a detailed description of the propagation equation used to simulate numerically filamentation and conical pulse propagation as briefly hinted in Chapter 1 (see Eqs.1.31 and 1.32). Alongside the description of the model itself we shall lay out the basic method to be followed in writing an efficient code based on these equations.

4.1 Model for ultrashort laser pulse propagation

Among the numerical tools developed to investigate the generation of conical waves by filamentation, a propagation code was used which allows simulations of a nonlinear envelope equation including various physical effects as source terms. The model describes the forward propagation of the envelope of the laser field with carrier frequency ω_0 and wavenumber $k_0 = k(\omega_0)$. It takes into account the effects of diffraction, group velocity dispersion, Kerr self-focusing with a possible delayed Raman contribution, nonlinear losses and optical shock formation. Let $\mathcal{E}$ denote the envelope $\mathcal{E}(r,t,z)$ in case of cylindrical symmetry around the propagation axis, or $\mathcal{E}(x,y,t,z)$ when no symmetry is assumed. The propagation equation then reads:

$$\mathcal{K}\frac{\partial \mathcal{E}}{\partial z} = \frac{i}{2}\left[\Delta_\perp \mathcal{E} + \mathcal{D}(\mathcal{E})\right] + k_0\left[(T^2 N_{\mathrm{Kerr}}(\mathcal{E}) + T N_{\mathrm{NLL}}(\mathcal{E}) + N_{\mathrm{Plasma}}(\rho,\mathcal{E})\right] \tag{4.1}$$

where $\Delta_\perp \equiv \partial_r^2 + (1/r)\partial_r$ for cylindrically symmetric beams or $\Delta_\perp \equiv \partial_x^2 + \partial_y^2$ otherwise, $\mathcal{D}$ denotes the operator accounting for all dispersive terms, $N_{\mathrm{Kerr}}(\mathcal{E})$ and $N_{\mathrm{NLL}}(\mathcal{E})$ denote the nonlinear source terms associated with the optical Kerr effect and nonlinear losses, $N_{\mathrm{Plasma}}(\rho,\mathcal{E})$ denotes those associated with plasma effects, $T \equiv 1 + i\omega_0^{-1}\partial/\partial t$ and $\mathcal{K} \equiv k_0 + ik_0'\partial/\partial_t$. The operator $\mathcal{D}$ can be readily expressed only in the spectral domain. Let the Fourier transform associated with the temporal coordinate t be defined by:

$$\hat{E}(r,\omega,z) = \int_{-\infty}^{+\infty} E(r,t,z)\mathrm{e}^{-i\omega t}dt \tag{4.2}$$

A useful expression of $\mathcal{D}(\mathcal{E})$ is then obtained in the spectral domain:

$$\widehat{\mathcal{D}(\mathcal{E})} \equiv (k^2(\omega) - \hat{\mathcal{K}}^2)\hat{\mathcal{E}}, \tag{4.3}$$

where $\hat{\mathcal{K}} = k_0 + k_0'(\omega - \omega_0)$. It can be readily seen by a small $\omega - \omega_0$ expansion that: $(k^2(\omega) - \hat{\mathcal{K}}^2)/2\hat{\mathcal{K}} \simeq k_0''(\omega - \omega_0)^2/2 + k_0'''(\omega - \omega_0)^3/6 + \cdots$, which shows that the second term in the rhs of Eq.4.1 accounts for GVD at second and higher-orders. Since Eq.4.1 accounts for space-time focusing and self-steepening of the pulse described by operators $\mathcal{K}$ and T, the model is virtually not limited by the slowly varying envelope approximation (along the temporal direction) which is standard for equations of the nonlinear Schrödinger type [28]. Single cycle pulses are modeled properly by Eq.4.1.

4.1.1 Derivation of the propagation equation

We briefly recall the derivation of Eq.4.1 and specify the approximations made. In this section only, t and z will refer to time and the propagation distance in the laboratory frame while τ and ζ will refer to these quantities in the frame of the propagating pulse. From Maxwell equations and constitutive equations for the medium, the vector wave equation governing the evolution of the laser pulse in a transparent nonlinear medium reads:

$$\begin{aligned}\nabla^2\mathbf{E} - \nabla(\nabla\cdot\mathbf{E}) - \frac{1}{c^2}\frac{\partial^2}{\partial t^2}\int_{-\infty}^{t} n^2(r,t-t')\mathbf{E}(r,t',z)dt' = \\ = \mu_0\left(\frac{\partial^2\mathbf{P}_{\rm nl}}{\partial t^2} + \frac{\partial\mathbf{J}_{\rm p}}{\partial t}\right)\end{aligned} \tag{4.4}$$

where $n^2(\omega) = 1 + \epsilon_0\chi^{(1)}(\omega)$ is the linear index of refraction due to vacuum and bound electrons, $\chi^{(1)}$ is the linear susceptibility, $\mathbf{P}_{\rm nl}$ is the nonlinear polarization associated with bound electrons, $\mathbf{J}_{\rm p}$ is the plasma current density associated with the free electrons [9]. Several successive approximations are made to derive Eq.4.1, specified here with the terms they allow us to neglect:

First, the electric field is assumed to remain linearly polarized along a direction $\mathbf{e}_x$ transverse to the propagation axis. Thus, $\mathbf{E} = E\mathbf{e}_x$, the term $\nabla(\nabla\cdot\mathbf{E})$ can be neglected and Eq.4.4 can be rewritten in a scalar form.

$$\Delta_\perp E + \frac{\partial^2 E}{\partial z^2} - \frac{1}{c^2}\frac{\partial^2}{\partial t^2}\int_{-\infty}^{t} n^2(r,t-t')\mathrm{E}(r,t',z)dt' = \mu_0\left(\frac{\partial^2\mathrm{P}_{\rm nl}}{\partial t^2} + \frac{\partial\mathrm{J}_{\rm p}}{\partial t}\right) \tag{4.5}$$

Second, we consider first the linear part of the wave equation (4.5):

$$(\nabla_\perp^2 + \partial_z^2)E(r,t,z) - \frac{1}{c^2}\partial_t^2\int_{-\infty}^{t} dt' n^2(r,t-t')E(r,t',z) = 0 \tag{4.6}$$

The laser field is rewritten by using the carrier wave and envelope:

$$E(r,t,z) = \frac{1}{2}\mathcal{E}(r,t,z)\exp[i(k_0 z - \omega_0 t)] + \text{c.}c. \tag{4.7}$$

Note than at this stage, no approximation is made regarding the shortness of the pulse duration compared to the cycle duration $2\pi\omega_0^{-1}$. In the Fourier domain, the propagation equation of the envelope then reads as:

$$(\nabla_\perp^2 + \partial_z^2 + 2ik_0\partial_z - k_0^2)\hat{\mathcal{E}} + k^2(\omega)\hat{\mathcal{E}} = 0, \tag{4.8}$$

which we rewrite in the temporal domain by using Eq.4.3:

$$(\nabla_\perp^2 + \partial_z^2 + 2ik_0\partial_z - k_0^2)\mathcal{E} + (\mathcal{D} + \mathcal{K}^2)\mathcal{E} = 0. \tag{4.9}$$

Third, for numerical convenience, we will rewrite propagation equations in the reference frame of the laser pulse: $\tau = t - k_0' z, \zeta = z$; the first order derivatives along t and z read as: $\partial_z = \partial_\zeta - k_0'\partial_\tau$, $\partial_t = \partial_\tau$; by introducing these expression in Eq.4.9, the linear terms in the propagation equation are expressed as:

$$(\nabla_\perp^2 + \partial_\zeta^2 - 2k_0'\partial_\tau\partial_\zeta + k_0'^2\partial_\tau^2 + 2ik_0\partial_\zeta - 2ik_0k_0'\partial_\tau - k_0^2)\mathcal{E} + (\mathcal{D}+\mathcal{K}^2)\mathcal{E} = 0. \tag{4.10}$$

After simplification of the 4th, 6th 7th and 9th terms in Eq.4.10, we otain:

$$(\nabla_\perp^2 + \partial_\zeta^2 + 2i\mathcal{K}\partial_\zeta)\mathcal{E} + \mathcal{D}\mathcal{E} = 0. \tag{4.11}$$

The last step to retrieve Eq.4.1 consists in the slowly varying envelope approximation along the longitudinal direction ζ: $\partial_\zeta^2 \ll k_0\partial_\zeta$, allowing us to neglect the second order derivative; this yields the linear part of Eq.4.1.

By applying the envelope decomposition to the nonlinear polarization and current, it is finally possible to reintroduce the nonlinear terms:

$$2i\mathcal{K}\partial_\zeta\mathcal{E} + \nabla_\perp^2\mathcal{E} + \mathcal{D}\mathcal{E} = \mu_0\left(-\omega_0^2 T^2\mathcal{P}_{\text{nl}} - i\omega_0 T\mathcal{J}_{\text{p}}\right), \tag{4.12}$$

where $\mathcal{P}_{\text{nl}}$ represents the Kerr term and $\mathcal{J}_{\text{p}}$ includes both nonlinear losses and the plasma contribution in Eq.4.1.

$$2ik_0 N_{\text{Kerr}} = -\mu_0\omega_0^2\mathcal{P}_{\text{nl}} \tag{4.13}$$

$$2ik_0(TN_{\text{NLL}} + N_{\text{Plasma}}) = -\mu_0 i\omega_0 T\mathcal{J}_{\text{p}} \tag{4.14}$$

4.1.2 Initial pulse

Initial conditions must be given to start the propagation. Without loss of generality, the field distribution $\mathcal{E}(r,t,z=0)$ can be arbitrary; however, the output field of a laser is usually modeled as a Gaussian beam and pulse

$$\mathcal{E}(r,t,0) = \sqrt{I_0}\exp\left[-\frac{r^2}{w_0^2} - i\frac{kr^2}{2f} - \frac{t^2}{t_p^2} - iCt^2\right]. \tag{4.15}$$

with beam width w_0, temporal half width t_p, input peak intensity I_0, input peak power $P_{\text{in}} = \pi w_0^2 I_0/2$ and energy $E_{\text{in}} = P_{\text{in}} t_p \sqrt{\pi/2}$. When the beam is focused, the curvature radius f of the beam and the focusing distance d are related by the relation:

$$f = d + z_f^2/d, \tag{4.16}$$

where $z_f = k_0 w_f^2/2$ denotes the Rayleigh length associated with the beam waist w_f and

$$w_f \equiv \frac{w_0}{\sqrt{1 + z_0^2/f^2}}, \tag{4.17}$$

where $z_0 = k_0 w_0^2/2$ denotes the Rayleigh length associated with the beam width w_0.

When the pulse is chirped, the chirp coefficient C is linked to the minimal pulse duration t_m obtained by propagation of a pulse of duration t_p in a dispersive medium characterized only by second order dispersion k_0'':

$$t_m = \frac{t_p}{\sqrt{1 + C^2 t_p^4}} \tag{4.18}$$

4.1.3 Nonlinear terms

The nonlinear polarization $\mathbf{P}_{\text{nl}}$ reads at the dominant third order for a centro-symmetric medium:

$$\mathbf{P}_{\text{nl}} \equiv \epsilon_0 \chi^{(3)} |\mathbf{E}|^2 \mathbf{E} \tag{4.19}$$

The corresponding envelope reads:

$$\mathcal{P}_{\text{nl}} \equiv \epsilon_0 \chi^{(3)} \frac{3}{4} |\mathcal{E}|^2 \mathcal{E} \tag{4.20}$$

By introducing in Eq.4.20 the nonlinear index coefficient $n_2 \equiv 3\chi^{(3)}/4\epsilon_0 c n_0^2$, and by introducing the result in Eq.4.13, an expression is obtained for the Kerr term (for an intantaneous response of the medium) [1]:

$$N_{\text{Kerr}} = i\frac{\omega_0}{c} n_2 |\mathcal{E}|^2 \mathcal{E}, \tag{4.21}$$

[1] Note that we are defining the nonlinear index in a slightly different way with respect to Chapter 1. Although the approach shown in Chapter 1 is formally correct, the most common definition and use of units are those used here.

where $n_2|\mathcal{E}|^2$ is assumed to be dimensionless, i.e. a factor $\epsilon_0 c n_0/2$ was canceled in the unit conversion and $|\mathcal{E}|^2$ was assumed to be expressed in W/cm^2.

The optical Kerr effect includes in general the electronic contribution which is nearly instantaneous and a delayed component of fraction α, due to stimulated molecular Raman scattering. The Kerr term therefore reads as

$$N_{\text{Kerr}}(\mathcal{E}) = \\ i\frac{\omega_0}{c} n_2 \left((1-\alpha)|\mathcal{E}(r,t,z)|^2 + \alpha \int_{-\infty}^{t} \mathcal{R}(t-\tau)|\mathcal{E}(r,\tau,z)|^2 d\tau \right) \mathcal{E}\,, \quad (4.22)$$

The function $\mathcal{R}(t)$ mimics the molecular response with a characteristic time Γ^{-1} and frequency ω_R:

$$\mathcal{R}(t) = \mathcal{R}_0 \exp(-\Gamma t) \sin \omega_R t \quad (4.23)$$

where $\mathcal{R}_0 = (\Gamma^2 + \omega_R^2)/\omega_R$.

Nonlinear losses describe multiphoton processes of order K:

$$N_{\text{NLL}}(\mathcal{E}) = -\frac{\beta_K}{2}|\mathcal{E}|^{2K-2}\mathcal{E}. \quad (4.24)$$

Equation 4.24 is found by introducing a current J_{NLL} such that $\mathbf{J}\cdot\mathbf{E} = K\hbar\omega_0\sigma_K|\mathcal{E}|^{2K}\rho_{at}$

Finally, when the pulse is so intense that it ionizes the medium, the plasma term

$$N_{\text{Plasma}}(\rho) = -\frac{\sigma}{2}(1+i\omega\tau_{\text{c}})\rho\mathcal{E}, \quad (4.25)$$

where ρ denotes the electron density accounts for plasma absorption (real part) and plasma defocusing (imaginary part). Equation 4.25 depends on frequency ω both directly and through $\sigma(\omega)$ so that it is in principle exact only in the Fourier domain, i.e. by replacing $\rho\mathcal{E}$ by $\widehat{\rho\mathcal{E}}$. It follows from the evolution equation for the plasma current density:

$$\frac{\partial \mathbf{J}_{\text{p}}}{\partial t} + \frac{\mathbf{J}_{\text{p}}}{\tau_c} = \frac{e^2}{m_e}\rho\mathbf{E}, \quad (4.26)$$

where τ_{c} is the electron collision time. Solving Eq.4.26 in the Fourier domain yields:

$$\hat{\mathbf{J}}_{\text{p}} = \frac{e^2\tau_c}{m_e}\frac{1+i\omega\tau_c}{1+\omega^2\tau_c^2}\widehat{\rho E} \quad (4.27)$$

As retrieved from (4.27), The cross section σ for inverse Bremsstrahlung follows the Drude model [84] and reads:

$$\sigma(\omega) = \frac{k_0}{n_0^2\rho_{\text{c}}}\frac{\omega\tau_{\text{c}}}{(1+\omega^2\tau_{\text{c}}^2)} \quad (4.28)$$

where $\rho_c \equiv \epsilon_0 m_e \omega_0^2/e^2$, the critical plasma density above which the plasma becomes opaque. Equation 4.25 is finally found by introducing Eq.4.27 into Eq.4.14.

The evolution of the electron density ρ entering in Eq.4.25 is governed by:

$$\frac{\partial \rho}{\partial t} = \frac{\beta_K}{K\hbar\omega_0}|\mathcal{E}|^{2K} + \frac{\sigma}{U_i}\rho|\mathcal{E}|^2, \tag{4.29}$$

which describes the generation of the plasma by multiphoton ionization (first term on the rhs) and avalanche with rate $(\sigma/U_i)|\mathcal{E}|^2$.

In the often encountered limit of large collision times $\tau_c \gg \omega_0^{-1}$, the defocusing term in (4.25) can be expressed as a function of the critical plasma density ρ_c beyond which the plasma becomes opaque $\sigma\omega_0\tau_c\rho \simeq k_0\rho/n_0^2\rho_c$.

4.2 Numerical implementation of the nonlinear envelope equation

We will describe the method used to build step by step the general numerical tool allowing us to perform numerical resolution of Eq.4.1. To this aim, we first reduce Eq.4.1 to the simplest case of linear propagation under the effect of diffraction only, which constitutes the basis of the propagation code. Other physical effects will then be added one after another in a way that extends the generality and validity of the numerical tool which can be built without increasing too much its complexity.

4.2.1 Diffraction

Diffraction occurs in all media and even in vacuum. It is described by the paraxial equation

$$\frac{\partial \mathcal{E}}{\partial z} = \frac{i}{2k_0}\Delta_\perp \mathcal{E} \tag{4.30}$$

We start by describing beam propagation so that $\mathcal{E}$ is assumed to depend only on the transverse variable r and the evolution variable z. We will describe first of all a simple but efficient scheme; we therefore discretize the radial axis for a box of finite size r_{max} by using a uniform grid $r_j = j\Delta r$ of $N_\perp$ steps Δr. Similarly, we will describe the propagation over a distance z_{max} by making steps $z_n = n\Delta z$ of constant size Δz. Let E_j^n denote $\mathcal{E}(r_j, z_n)$ A standard scheme to perform numerical simulations of equations having the same structure as Eq.4.30 is the Crank-Nicolson scheme. It is an implicit, second order inconditionally stable numerical scheme. Below, Δ_j denotes the discretized diffraction operator defined as

$$\Delta_j E_j^n \equiv E_{j-1}^n - 2E_j^n + E_{j+1}^n + \frac{1}{2j}(E_{j+1}^n - E_{j-1}^n) \tag{4.31}$$

and formally represented as a tridiagonal matrix

$$\Delta_j E_j^n = \begin{pmatrix} -2 & * & 0 & \cdots & \cdots & 0 & 0 \\ u_1 & -2 & v_1 & 0 & \cdots & 0 & 0 \\ 0 & \ddots & \ddots & \ddots & 0 & 0 & 0 \\ 0 & 0 & u_j & -2 & v_j & 0 & 0 \\ 0 & 0 & 0 & \ddots & \ddots & \ddots & 0 \\ 0 & \cdots & \cdots & 0 & u_{N_\perp-1} & -2 & v_{N_\perp-1} \\ 0 & \cdots & \cdots & \cdots & 0 & u_{N_\perp} & -2 \end{pmatrix} \begin{pmatrix} E_0^n \\ E_1^n \\ \vdots \\ E_j^n \\ \vdots \\ \vdots \\ E_{N_\perp}^n \end{pmatrix}$$

where $u_j = 1 - 1/2j$ and $v_j = 1 + 1/2j$. The first line is undefined at this stage but the first and last lines will be replaced as indicated below for taking into account boundary conditions.

The Crank-Nicolson sheme reads as

$$E_j^{n+1} - E_j^n = i\frac{\delta}{2}(\Delta_j E_j^{n+1} + \Delta_j E_j^n) \tag{4.32}$$

where $\delta = \Delta z/2k_0(\Delta r)^2$. The solution of (4.32) reads as

$$E_j^{n+1} = (1 - i\frac{\delta}{2}\Delta_j)^{-1}(1 + i\frac{\delta}{2}\Delta_j)E_j^n \tag{4.33}$$

and requires multiplication of the tridiagonal complex matrix $L_+ = 1 + i(\delta/2)\Delta_j$ by the vector E_j^n and the inversion of the tridiagonal complex matrix $L_- = 1 - i(\delta/2)\Delta_j$.

$$L_+ E_j^n = \begin{pmatrix} 0 & 0 & 0 & 0 & 0 \\ \ddots & \ddots & \ddots & 0 & 0 \\ 0 & \frac{i\delta}{2}u_j & 1 - i\delta & \frac{i\delta}{2}v_j & 0 \\ 0 & 0 & \ddots & \ddots & \ddots \\ 0 & 0 & 0 & 0 & 0 \end{pmatrix} \begin{pmatrix} E_0^n \\ \vdots \\ E_j^n \\ \vdots \\ E_{N_\perp}^n \end{pmatrix}$$

$$L_- E_j^n = \begin{pmatrix} 1 & -1 & 0 & 0 & 0 \\ \ddots & \ddots & \ddots & 0 & 0 \\ 0 & -\frac{i\delta}{2}u_j & 1 + i\delta & -\frac{i\delta}{2}v_j & 0 \\ 0 & 0 & \ddots & \ddots & \ddots \\ 0 & 0 & 0 & 0 & 1 \end{pmatrix} \begin{pmatrix} E_0^n \\ \vdots \\ E_j^n \\ \vdots \\ E_{N_\perp}^n \end{pmatrix}$$

The different steps to build a very simple propagation code for simulations of Eq.4.30 are therefore the following:

- 1- definition of the initial data, laser and medium parameter, e.g., beam width w_0, focusing length f, etc.

- 2- definition of grids and quantities useful for the propagation over one step but which are z invariant.
  - r-grid: $r_j = j\Delta r$, for $j = 0, \cdots, N_\perp$
  - matrix $L_+ = 1 + i(\delta/2)\Delta_j$
  - matrix $L_- = 1 - i(\delta/2)\Delta_j$
  - definition of boundary conditions: $\partial\mathcal{E}/\partial r = 0$ at $r = 0$ and $\mathcal{E} = 0$ at $r = r_{max}$. This is achieved by changing all elements on the first and last lines of L_+ into zero and by setting the first line of L_- to $(1; -1; 0; \cdots; 0)$ and its last line to $(1; 0; 0; \cdots; 0)$. Boundary layers are usually added to ensure tranparent boundary conditions as indicated in the separate section below.
  - calculation of the inverse L_-^{-1}
  - calculation of the product $L = L_-^{-1}L_+$
- 3- definition of the initial field, e.g., for a Gaussian beam $\mathcal{E}(r, z = 0) = \mathcal{E}_0 \exp(-r^2/w_0^2 - ik_0 r^2/2f)$
  $E_j^0 = \mathcal{E}(r_j, z = 0)$
- 4- loop on propagation steps with diagnostics each M steps:

outer loop:	$k = 0, \ldots, K_{max}$		
	inner loop:	$m = 1, \ldots, M$	
		$n = kM + m$	
		$E_j^n = LE_j^{n-1}$	
		perform type 1 diagnostics	
	end inner loop		
	perform type 2 diagnostics		
end outer loop			

Steps 1 to 3 correspond to the initialization of the propagation. Step 4 constitutes the bulk of the scheme; it is centered around one propagation step following Eq.4.33, the core of the scheme. Two types of diagnostics are indicated (they are specified below) to separate the fast diagnostics consuming few time or memory, thus performed at each step, from those needing longer times or larger computer ressources.

4.2.2 Diffraction and nonlinear terms

We consider now the model including simple nonlinear terms such as the instantaneous part of the optical Kerr effect and nonlinear losses

$$\frac{\partial\mathcal{E}}{\partial z} = \frac{i}{2k}\Delta_\perp\mathcal{E} + i\frac{\omega_0}{c}n_2|\mathcal{E}|^2\mathcal{E} - \frac{\beta_K}{2}|\mathcal{E}|^{2K-2}\mathcal{E} \tag{4.34}$$

In order to extend the Crank-Nicolson sheme to Eq.4.34, we use the Dufort-Frankel scheme which is an explicit scheme working in general for all type of nonlinear terms. The advantage of this scheme lies in the fact that it preserves the second order accuracy of the Crank-Nicolson sheme and allows faster calculation of the right hand side in Eq.4.34 without resorting to a completely implicit scheme which would need implementation of predictor-corrector routines and of a large number of matrix inversions.

It reads as

$$E_j^{n+1} - E_j^n = i\frac{\delta}{2}(\Delta_j E_j^{n+1} + \Delta_j E_j^n) + \frac{3}{2}N_j^n - \frac{1}{2}N_j^{n-1}, \tag{4.35}$$

where

$$N_j^n \equiv N(E_j^n) = \Delta z \left\{ i\frac{\omega_0}{c} n_2 |E_j^n|^2 E_j^n - \frac{\beta_K}{2}|E_j^n|^{2K-2} E_j^n \right\}. \tag{4.36}$$

Equation 4.35 allows us to express the vector E_j^{n+1} as a function of previously obtained fields E_j^n and E_j^{n-1}:

$$E_j^{n+1} = (L_-)^{-1}[L_+ E_j^n + \frac{3}{2}N(E_j^n) - \frac{1}{2}N(E_j^{n-1})] \tag{4.37}$$

It is no longer necessary to compute and store the product $L_-^{-1}L_+$ in the initialization step 2. Only the 4th step in the numerical scheme indicated above must be modified as:

- 4- loop on propagation steps with diagnostics each M steps:

outer loop:
$k = 0, \ldots, K_{max}$
  inner loop:
  $m = 1, \ldots, M$
    $n = kM + m$
    calculate and store vector N_j^{n-1} (loop $j, \cdots, N_\perp$)
    calculate $V_j^{n-1} = L_+ E_j^{n-1}$ (projuct matrix-vector)
    add $S_j^{n-1} = V_j^{n-1} + (3N_j^{n-1} - N_j^{n-2})/2$ (sum of vectors)
    $E_j^n = L_-^{-1} S_j^{n-1}$ (product matrix-vector)
    perform type 1 diagnostics
  end inner loop
  perform type 2 diagnostics
end outer loop

The overall stability of the scheme depends on the nonlinear terms, so that a control of the step size Δz may be necessary in contrast to the unconditionally stable Crank-Nicolson scheme; however, the stability constraint

associated with nonlinearity (for example $\Delta z \ll c/\omega_0 n_2 I_{max}$ for the Kerr term) is not so drastic as that for the description of diffraction with an explicit scheme ($\Delta z \leq k_0(\Delta r)^2$) [85].

4.2.3 Inclusion of dispersion, space-time focusing and self-steepening

For a pulse, we need to introduce one more dimension, the temporal coordinate, discretized as $t_l = t_0 + l\Delta t$. By working in the corresponding spectral domain $\omega_l = \omega_0 + l\Delta\omega$, it is actually possible to extend the previous numerical scheme easily so as to include simultaneously the effects of dispersion, space-time focusing and self-steepening. Note that in this section, the index l will refer to either discrete times or discrete frequencies, depending on whether the quantity we consider belongs to the temporal or the spectral domain. Equation 4.1 rewritten in the spectral domain reads:

$$\hat{\mathcal{K}}\frac{\partial\hat{\mathcal{E}}}{\partial z} = \frac{i}{2}\left[\Delta_\perp\hat{\mathcal{E}} + \hat{\mathcal{D}}\hat{\mathcal{E}}\right] + \\ + k_0\left[(\hat{T}^2\hat{N}_{\mathrm{Kerr}}(\mathcal{E}) + \hat{T}\hat{N}_{\mathrm{NLL}}(\mathcal{E}) + \hat{N}_{\mathrm{Plasma}}(\rho,\mathcal{E})\right]. \quad (4.38)$$

Let ω_l, $\hat{\mathcal{K}}_l$, $\hat{\mathcal{D}}_l$ and $\hat{T}_l$ denote $\omega_0 + l\Delta\omega$, $\hat{\mathcal{K}}(\omega_l)$, $\hat{\mathcal{D}}(\omega_l)$ and $\hat{T}(\omega_l)$, respectively.

The numerical scheme extending Eq.4.35 and corresponding to Eq.4.38 reads:

$$\hat{E}^{n+1}_{j,l} - \hat{E}^n_{j,l} = i\frac{\delta_l}{2}(\Delta_j\hat{E}^{n+1}_{j,l} + \Delta_j\hat{E}^n_{j,l}) + \\ + i\frac{d_l}{2}(\hat{E}^{n+1}_{j,l} + \hat{E}^n_{j,l}) + \frac{3}{2}\hat{N}^n_{j,l} - \frac{1}{2}\hat{N}^{n-1}_{j,l} \quad (4.39)$$

where

$$\delta_l = \frac{\delta}{\hat{\mathcal{K}}_l} = \frac{\Delta z}{2(\Delta r)^2\hat{\mathcal{K}}_l} \quad (4.40)$$

$$d_l = \frac{\Delta z\hat{\mathcal{D}}_l}{2\hat{\mathcal{K}}_l} \quad (4.41)$$

$$\hat{N}^n_{j,l} \equiv \hat{N}(E^n_{j,l},\rho^n_{j,l}) = \\ \frac{k_0\Delta z}{\hat{\mathcal{K}}_l}\left\{\hat{T}_l^2\hat{N}_{\mathrm{Kerr}}(E^n_{j,l}) + \hat{T}_l\hat{N}_{\mathrm{NLL}}(E^n_{j,l}) + \hat{N}_{\mathrm{Plasma}}(E^n_{j,l},\rho^n_{j,l})\right\} \quad (4.42)$$

The solution to equation (4.39) represents one step along the propagation direction and reads as:

$$\hat{E}_{j,l}^{n+1} = (L_{-,l})^{-1}[L_{+,l}\hat{E}_{j,l}^{n} + \frac{3}{2}\hat{N}_{j,l}^{n} - \frac{1}{2}\hat{N}_{j,l}^{n-1}] \tag{4.43}$$

where $L_{-,l} \equiv 1 - i(\delta_l/2)\Delta_j - i(d_l/2)$, $L_{+,l} \equiv 1 + i(\delta_l/2)\Delta_j + i(d_l/2)$. With respect to previous expressions of L_- and L_+, the matrices $L_{-,l}$ and $L_{+,l}$ are different only by the frequency dependence of δ_l terms issued from space time focusing and by an additional term d_l on the diagonal, issued from dispersion. As for L_- and L_+, the matrices $L_{-,l}$ and $L_{+,l}$ operate on vectors representing transverse profiles (described by index j) of the Fourier components $\hat{E}_{j,l}$ for the envelope, corresponding to the fixed frequency ω_l; in other words, Eq.4.43 allows us to apply the standard Crank-Nicolson scheme to each frequency component l of the envelope spectrum, thus performing one step from $E_{j,l}^{n}$ at distance n to $E_{j,l}^{n+1}$ at distance $n+1$. This step must be inserted within a loop on frequencies (l).

Depending on the need to save either memory or simulation time, matrices $L_{-,l}$ and $L_{+,l}$ may be either precomputed (to minimize simulation time, in which case the additional amount of memory used corresponds to the size of a $14*N_\perp*N_\omega$ table of real numbers, seven diagonals of real numbers being needed to describe $L_{-,l}$ and $L_{+,l}$) or recomputed at each step (to minimize memory usage). In the second option, step 2 of the scheme is simplified since only the minimal set of frequency dependent tables required to reconstruct $L_{-,l}$ and $L_{+,l}$ in step 4 must be precomputed. The changes in steps 1 to 4 read:

- 1- definition of the initial data, laser and medium parameter; in particular everything needed to properly define the dispersion relation in the medium, Raman-Kerr parameters, ionization rates, etc.
- 2- definition of grids and quantities useful for the propagation over one step but which are z invariant.
  - r-grid: $r_j = j\Delta r$, for $j = 0, \cdots, N_\perp$
  - ω-grid: $\omega_l = \omega_0 + (l - N_\omega/2)2\pi/N_\omega\Delta t$, for $l = 1, \cdots, N_\omega$
  - calculation and storage of the one dimensional tables: $\hat{\mathcal{K}}_l$, $\hat{\mathcal{D}}_l$ and $\hat{T}_l$, $\hat{T}_l^2$, d_l, δ_l
- 3- definition of the initial field, e.g., for Gaussian profiles of the beam and pulse

$$\mathcal{E}(r,t,z=0) = \mathcal{E}_0 \exp\left(-\frac{r^2}{w_0^2} - \frac{t^2}{t_p^2} - i\frac{k_0 r^2}{2f} - iCt^2\right)$$

  $E_{j,l}^0 = \mathcal{E}(r_j, t_l, z=0)$
- 4- loop on propagation steps with diagnostics each M steps:

```
outer loop:
k = 0, ..., K_max
  inner loop:
  m = 1, ..., M
    n = kM + m
    calculate electron density ρ_{j,l}^{n-1}                          (solve N_⊥ o.d.e.s (4.29) j = 0, ··· , N_⊥)
    calculate Raman-Kerr term Q_{j,l}^{n-1} = Q_i(r_j, t_l, z_{n-1})  (solve N_⊥ o.d.e.s (4.44) j = 0, ··· , N_⊥)
    calculate and store tables:
      N_Kerr(E_{j,l}^{n-1}), N_NLL(E_{j,l}^{n-1}), N_Plasma(E_{j,l}^{n-1})   (double loop j = 0, ··· , N_⊥; l = 1, ··· , N_ω)
    Fourier transform the above tables and E_{j,l}^{n-1} as well      (any FFT routine)
    calculate and store table N_{j,l}^{n-1} from Eq.4.42              (multiplication by T̂_l/K̂_l or T̂_l^2/K̂_l and sum)
    loop on frequencies
    l = 1, ··· , N_ω
      calculate L_{+,l}, L_{-,l}                                      (tridiagonal complex matrices)
      calculate L_{-,l}^{-1}                                          (matrix inversion)
      calculate V_{j,l}^{n-1} = L_{+,l} Ê_{j,l}^{n-1}                 (projuct matrix-vector)
      add S_{j,l}^{n-1} = V_{j,l}^{n-1} + (3N̂_{j,l}^{n-1} − N̂_{j,l}^{n-2})/2   (sum of vectors)
      Ê_{j,l}^{n} = L_-^{-1} S_{j,l}^{n-1}                            (product matrix-vector)
    end loop on frequencies (l)
    inverse Fourier transform Ê_{j,l}^{n} → E_{j,l}^{n}
    store E_{j,l}^{n}
    perform type 1 diagnostics
  end inner loop (m)
  perform type 2 diagnostics
end outer loop (k)
```

Step 4 still constitutes the bulk of the scheme. It is evident that efficiency of the code is enhanced if all unnecessarily repetitive calculations are avoided. These concern loops including multiplications by factors which do not vary with the loop index. For example it is clear that a single table must represent the quantity $k_0 \Delta z \hat{T}_l^2/\mathcal{K}_l$ in front of the nonlinear Kerr term in (4.42) so that the calculation of the first term in $N_{j,l}^{n-1}$ needs multiplication by only one factor, although we have kept all for clarity. Constant factors can also usually be removed via renormalization of the discretized equations. As a general rule, the efficiency of a code must be optimized by a careful count of all operations appearing in inbricated loops and an attempt to minimize them. For example, all matrix-vector operations performed on with tridiagonal matrices must be implemented so as to avoid unnecessary multiplication and sum of zeros. This can be achieved by using compact matrix storage for the non-nil diagonals only, as discussed in [85].

4.2.4 Calculation of the Raman-Kerr and plasma contributions

The inclusion in the numerical scheme of the Raman-Kerr contribution is formally equivalent to that of the plasma. Thus we limit the analysis to the Raman-Kerr term. We indicate two possibilities to achieve this task.

- 1- Resolution of an ordinary differential equation: Assuming that the envelope $\mathcal{E}(r,t,z)$ is known at a given propagation distance z, both the electron density $\rho(r,t,z)$ and the Raman-Kerr contribution $Q_i(r,t,z) = \int_{-\infty}^{t} \mathcal{R}_0 \exp[-\Gamma(t-\tau)] \sin[\omega_R(t-\tau)] |\mathcal{E}(r,\tau,z)|^2 d\tau$ are solutions to a non-homogeneous o.d.e. that involves $\mathcal{E}(r,t,z)$ as a source term. The temporal profiles $\rho(r,t,z)$ and $Q_i(r,t,z)$ are indeed obtained for each fixed

spatial coordinate (r, z) by solving Eq.4.29 for ρ with boundary condition $\rho(-\infty) = \rho_0 \ll \rho_{at}$ and Eq.4.44:

$$\frac{\partial^2 Q_i}{\partial t^2} + 2\Gamma\frac{\partial Q_i}{\partial t} + (\omega_R^2 + \Gamma^2)Q_i = (\omega_R^2 + \Gamma^2)|\mathcal{E}(r,t,z)|^2, \tag{4.44}$$

for Q_i with boundary conditions $\partial Q_i/\partial t(-\infty) = 0$ and $Q_i(-\infty) = 0$. These tasks can be done by any o.d.e. solver based on, e.g., the Runge-Kutta scheme [85].

- 2 - Direct resolution. An explicit formulation satisfying Eq.4.44 exists for the Raman-Kerr response (the electron density, solution to Eq.4.29 admits a similar and simpler explicit formulation):

$$Q_i(r,t,z) = \int_{-\infty}^{t} \mathcal{R}_0 \exp[-\Gamma(t-\tau)]\sin[\omega_R(t-\tau)]|\mathcal{E}(r,\tau,z)|^2 d\tau \tag{4.45}$$

which can be rewritten as the imaginary part of

$$Q(r,t,z) = \mathcal{R}_0\left\{\mathrm{e}^{-\Gamma t + i\omega_R t}\int_{-\infty}^{t}\mathrm{e}^{\Gamma\tau - i\omega_R\tau}|\mathcal{E}(r,\tau,z)|^2 d\tau\right\} \tag{4.46}$$

A numerical scheme to compute Eq.4.46 is obtained by using a trapezoidal evaluation of the integral term:

$$\begin{aligned} Q(r,t+\Delta t,z) &= \mathrm{e}^{(-\Gamma+i\omega_R)\Delta t}Q(r,t,z) + \\ \frac{\Delta t}{2}&\left[|\mathcal{E}(r,t+\Delta t,z)|^2 + \mathrm{e}^{(-\Gamma+i\omega_R)\Delta t}|\mathcal{E}(r,t,z)|^2\right] \end{aligned} \tag{4.47}$$

Discretization of this scheme leads to an expression allowing the calculation of the temporal profiles for the complex Raman-Kerr response $Q(r,t,z)$ at each fixed spatial position (r,z).

$$Q^n_{j,l+1} = \left\{\mathrm{e}^{(-\Gamma+i\omega_R)dt}Q^n_{j,l} + \frac{\Delta t}{2}[|E^n_{j,l+1}|^2 + \mathrm{e}^{(-\Gamma+i\omega_R)dt}|E^n_{j,l}|^2]\right\} \tag{4.48}$$

from which $Q_i(r,t,z) \equiv \mathrm{Im}(Q^n_{j,l})$ is obtained. Scheme (4.48) must be inserted within an outer loop on j (transverse coordinate) and an inner loop on l (time).

4.2.5 Nonuniform grids

When dealing with phenomena such as filamentation for which beams shrink in the transverse diffraction plane and remain confined in a tiny part of the numerical box, one might wish to increase locally the resolution while avoiding an excessive increase of the number of grid points (and so, of the simulation time). A solution to this issue consists in using non uniform

grids with a large number of points in the regions where the beam or pulse becomes intense, narrow or short, and a more tenuous density of grid points in less intense regions. As an example, we may consider self-focusing of a cylindrically symmetric, initially collimated beam. Typically, an input beam of full width at half maximum of a few hundreds of microns will self-focus in a transparent solid down to a few microns so that close to the axis $r = 0$, a fine discretization is necessary to proceed the simulation beyond the nonlinear focus.

In this case, it is convenient to use a mapping between the physical space (say with coordinate r, but the scheme can be applied to all coordinates) and the computational space (with coordinate R). The physical and the computational coordinates are linked by a relation:

$$r = f(R),$$

where f denotes the mapping function. The propagation equation to be solved involves partial derivatives with respect to physical coordinates. Below, we give the corresponding terms as functions of the computational coordinates and an example of mapping function and its derivatives. The first and second order derivatives with respect to r read:

$$\frac{\partial}{\partial r} = \frac{1}{f'(R)}\frac{\partial}{\partial R}, \qquad \frac{\partial^2}{\partial r^2} = \frac{1}{f'^2(R)}\left(\frac{\partial^2}{\partial R^2} - \frac{f''}{f'}\frac{\partial}{\partial R}\right),$$

and the transverse Laplacian operator which describes diffraction then reads as

$$\frac{\partial^2}{\partial r^2} + \frac{1}{r}\frac{\partial}{\partial r} = F(R)\frac{\partial^2}{\partial R^2} + G(R)\frac{\partial}{\partial R} \quad \text{with} \quad F(R) = \frac{1}{f'^2(R)} \quad \text{and} \quad G(R) = \left(\frac{1}{ff'} - \frac{f''}{f'^3}\right)$$

In order to use non-uniform grids with the same numerical schemes as described above, the computational axis R can be discretized by using a uniform grid $R_j = j\Delta R$ and the only change in the scheme then concerns the coefficients in the tridiagonal matrices Δ_j, L_- and L_+ which must take account of $F_j \equiv F(R_j)$, $G_j = G(R_j)$, $u_j = F_j - G_j$ and $v_j = F_j + G_j$:

$$\Delta_j E_j^n = \begin{pmatrix} * & * & 0 & \cdots & \cdots & 0 & 0 \\ u_1 & -2F_1 & v_1 & 0 & \cdots & 0 & 0 \\ 0 & \ddots & \ddots & \ddots & 0 & 0 & 0 \\ 0 & 0 & u_j & -2F_j & v_j & 0 & 0 \\ 0 & 0 & 0 & \ddots & \ddots & \ddots & 0 \\ 0 & \cdots & \cdots & 0 & u_{N_\perp-1} & -2F_{N_\perp-1} & v_{N_\perp-1} \\ 0 & \cdots & \cdots & \cdots & 0 & u_{N_\perp} & -2F_{N_\perp} \end{pmatrix} \begin{pmatrix} E_0^n \\ E_1^n \\ \vdots \\ E_j^n \\ \vdots \\ \vdots \\ E_{N_\perp}^n \end{pmatrix}$$

Finally, a convenient mapping function must be chosen. For the above mentioned example of self-focusing followed by filamentation, we found it convenient to use the mapping

$$f(R) = r_{max}\frac{(R/w_0 - 1 + \exp(-3R/R_{max}))}{R_{max}/w_0 - 1 + \exp(-3)}$$

which concentrates all the more the grid points around $r = 0$ as R_{max} approaches $3w_0$.

4.2.6 Boundary conditions

In order to avoid artifacts due to reflections at the boundaries of the numerical box, we added boundary layers close to the boundaries where the fields must vanish. These boundary layers are designed to either act as 'sponges' and absorb outgoing fields, or as 'perfectly matched layers' reducing the reflection coefficient ideally to zero. The reader is referred to Ref. [86] for theoretical and numerical details concerning perfectly matched layers. The use of this type of boundary condition works quite well for simulations of beam propagation, filaments and X-waves based on Eq.4.1.

As for boundary layers of the sponge type, the idea is to model a physical absorption process described by:

$$\frac{\partial \mathcal{E}}{\partial z} = -2\sigma h(r)\mathcal{E},$$

where 2σ denotes the maximum absorption coefficient and $h(r)$, a function increasing from zero to one over the width of the boundary layer $r_0 < r < r_{max}$; thus absorption occurs only in the boundary layer; for example $h(r) = (r - r_0)^2/(r_{max} - r_0)^2$ for $r \geq r_0$ and $h(r) = 0$ otherwise. Let j_0 denote the first integer such that $h(r_{j_0}) > 0$. In order to mimic absorbing boundary layers in the above schemes, it is sufficient to modify the diagonals of L_+ and L_- for terms $j_0 \leq j < N_\perp$ as: $\mathrm{diag}(L_+) \rightarrow \mathrm{diag}(L_+) - \sigma h_j$ and $\mathrm{diag}(L_-) \rightarrow \mathrm{diag}(L_-) + \sigma h_j$ where $h_j \equiv h(r_j)$. The last line $j = N_\perp$ must be kept unchanged as it corresponds to the condition at the bouundary of the numerical box.

4.2.7 Diagnostics

Simulations in 2+1 dimensions (i.e, r, t and z) involve a large volume of data. It is neither possible, nor useful, to record the complex field in all dimensions at each propagation step. This is the reason why we defined two types of diagnostics:

type 1: diagnostics that can been applied at each propagation step to find a well defined quantity, the storage of which costs a small amount of memory,

e.g. peak intensity $I_{max}(z = z_0)$, fluence distribution $F(r, z = z_0)$, full-width at half maximum of the fluence $D_{FWHM}(z = z_0)$, on-axis temporal profile $I(r = 0, t, z = z_0)$, etc

type 2: diagnostics which use a large amount of memory such as fields depending on all coordinates of the numerical grids at a given distance, e.g., $I(r, t, z_0)$, $\rho(r, t, z_0)$, far-fields $I(k_\perp, \omega, z = z_0)$, etc.

As indicated in the schemes above, the code performs type 1 diagnostics at each propagation step and type 2 diagnostics each M propagation steps. For each type of diagnostics, the results are saved in files for postprocessing and visualization.

4.2.8 Tests

Before performing any simulation in a physical situation of interest, a test of the tool was made so as to check the implementation of each physical effect separately with respect to known analytical solutions. In particular, provided the resolution is sufficient, the above schemes were checked to reproduce correctly the following phenomena:

- Diffraction of a Gaussian beam $\mathcal{E}(r, z = 0) = \mathcal{E}_0 \exp(-r^2/w_0^2)$:

$$\mathcal{E}(r, z) = \mathcal{E}_0 \frac{w_0}{w(z)} \exp(-\frac{r^2}{w^2(z)} - i\frac{k_0 r^2}{2F(z)}), \tag{4.49}$$

  where

$$w(z) = w_0\sqrt{1 + z^2/z_0^2} \tag{4.50}$$

$$F(z) = z(1 + z_0^2/z^2) \tag{4.51}$$

  with $z_0 = k_0 w_0^2/2$.
- (De)focusing of a Gaussian beam by a lens: $\mathcal{E}(r, z = 0) = \mathcal{E}_0 \exp(-r^2/w_0^2 - ik_0 r^2/2f)$: The envelope $\mathcal{E}(r, z)$ is given be Eq.4.49, but expressions for $w(z)$ and $F(z)$ are changed into:

$$w(z) = w_0\sqrt{1 + \frac{z^2}{z_0^2} - 2\frac{zd}{z_0^2}} \tag{4.52}$$

$$F(z) = (z - d)(1 + z_f^2/(z - d)^2) \tag{4.53}$$

  with $z_f = k_0 w_f^2/2$. The waist at focus is $w_f = w_0/\sqrt{1 + z_0^2/f^2}$ and is obtained at $z = d \equiv z_f z_0/f$.
- Dispersion of a Gaussian pulse $\mathcal{E}(t, z = 0) = \mathcal{E}_0 \exp(-t^2/t_p^2)$:

$$\mathcal{E}(t, z) = \mathcal{E}_0\sqrt{\frac{t_p}{\tau(z)}} \exp(-\frac{t^2}{\tau^2(z)} - iC_p(z)t^2), \tag{4.54}$$

where

$$\tau(z) = t_p\sqrt{1 + z^2/z_d^2} \tag{4.55}$$

$$C_p(z) = \frac{z_d}{t_p^2 z(1 + z_d^2/z^2)} \tag{4.56}$$

where $z_d = t_p^2/2k_0''$.

- Compression of a chirped Gaussian pulse $\mathcal{E}(t, z = 0) = \mathcal{E}_0 \exp(-t^2/t_p^2 - iCt^2)$: The envelope $\mathcal{E}(t, z)$ reads as Eq.4.54 but the pulse duration and chirp are expressed as

$$\tau(z) = t_p\sqrt{\left(1 + Ct_p^2\frac{z}{z_d}\right)^2 + \frac{z^2}{z_d^2}} \tag{4.57}$$

$$C_p(z) = \frac{z_d}{t_p^2((z - z_m)(1 + z_d^2/(z - z_m)^2)} \tag{4.58}$$

where $z_d \equiv t_p^2/2k_0''$. For negative chirps, the minimum pulse duration $t_m = t_p/\sqrt{1 + C^2t_p^4}$ is reached at $z_m = |C|z_d/(1 + C^2t_p^4)$.

- Self-focusing of a beam with power above the critical power for self-focusing, for an instantaneous optical Kerr effect. For a collimated Gaussian beam of power P_{in}, the self-focusing (collapse) distance follows [16].

$$z_c = \frac{0.367 z_0}{\sqrt{[(P_{\rm in}/P_{\rm cr})^{1/2} - 0.852]^2 - 0.0219}} \tag{4.59}$$

- Test of nonlinear losses with a plane wave. The intensity of the plane wave should follow:

$$I(z) = \frac{I_0}{(1 + (K - 1)\beta_K I_0^{K-1} z)^{1/K-1}} \tag{4.60}$$

- Test of spectral broadening by self phase modulation
- Test of ionization and the Raman-Kerr response by comparison of the direct method with the Runge-Kutta integration of o.d.e.s (4.29) or (4.44).
- Test of the stationarity of X-waves

For more complicated cases modeling a physical situation, the reliability of the results must be checked by doubling the numbers of steps in space r and time t while halving the respective step-sizes Δr and Δt. The propagation step Δz must also be decreased until no significant change in the results is observed. Finally, trustworthy results are also not significantly affected by an increase of the size of the numerical boxes (at constant resolution).

5

Ultrashort laser pulse filamentation and conical waves

Maybe the most surprising and incredible feature of laser pulser filamentation in Kerr media is the drastic reshaping of the pulse. Many models have been proposed to explain this reshaping. A brief overview of some of these was given in the first chapter but here we will inverstigate in some depth the implications and predictions of the X wave model. The assumption lying at the basis of this model is that the intensity and spectral reshaping of the pulse is driven by nonlinear interactions that will redistribute the energy of the pulse. This energy redistribution may be interpreted as a spontaneous evolution of the laser pulse toward some stationary state so that further propagation will not strongly affect it. Viewed from a slightly different perspective, spatial and temporal self-phase modulation will increase the spectrum and distort the pulse but all spectral components that are not stationary will be lost (due to dispersion and diffraction) during long distance propagation. This idea may be better appreciated through a comparison with standard Gaussian pulse optics. Table 5.1 is clearly not meant by any

Table 5.1. Comparison between standard laser optics based on Gaussian pulses and filament optics interpreted in terms of conical wave packets.

	Standard LASER physics	Filament physics
Stationary state	Gaussian pulse	Conical wave
coupling	r and t are decoupled	r and t are coupled
approximation	pulse is rarely a true Gaussian but the approximation works	the pulse is probably never a true conical wave
description	Gaussian pulses are easily treated in both (r, t) and (θ, λ)	Conical waves and filaments are best treated in (θ, λ)

means to be a complete or exhaustive overview of standard laser optics but simply a loose summary of some of the assumptions that lie at the basis of everyday reasoning in the lab. Our laser pulse will be generated by some laser, usually a quite complicated laser, that will reshape the light within the cavity in both spectrum (time) and angles (space) and the final result is usually a pulse that has a Gaussian-like profile both in time and space. Exceptions of course do exist, some lasers have a temporal profile that is closer to a sech(t) function, but this is not the point. The point is that we then treat and model propagation of this pulse as if it were a Gaussian pulse, ignoring the fact that we do not have infinitely extending tails or some extra noise or amplitude modulations. Yet the approximation works very well and leads, in most cases, to a deep understanding of the physics and gives the possibility to make precise predictions of what may happen in different circumstances. With filaments we may highlight similar features. It has been shown that an optical pulse in the presence of a Kerr nonlinearity and normal group velocity dispersion may assume a stationary state, the nonlinear X wave (i.e. a conical wave packet) [59]. So, in a similar fashion to what happens in a laser cavity, we may expect the input pulse to spontaneously evolve toward a stationary state and that, under these conditions, we may be able to describe the pulse propagation as if it where a conical wave. In this chapter we shall first show that the (θ, λ) spectra of ultrashort laser pulse filaments may be precisely described and reproduced using stationary conical wave $\theta(\lambda)$ relations (e.g. eqs. 2.12,2.13). In the normal group velocity dispersion regime the measured spectra bear evidence of the spontaneous formation of X waves, and passing into the anomalous group velocity dispersion regime the spectra change accordingly and show evidence of O wave and Fish wave formation. We shall then procede to treat the filament pulses in normal dispersion as X waves: by approximating the conical wave $\theta(\lambda)$ relation to second order in dispersion it is possible to analytically derive a series of results that lead to the conclusion that pulse splitting, an ever-present effect in filamentation, is the result of a phase matched parametric interaction between the input pump and the spontaneous X waves. The group velocity of the split X waves (and therefore their particular shape) depends directly on the pump peak intensity. This analysis will also open the question as to whether the single X wave is the result of a phase matched nonlinear process (or in other words, modulational instability) and the compatibility of such a process with the requirement of stationarity, which the conical waves obey.

5.1 Evidence of X wave formation in filament spectra

We start our analysis by studying filament formation in the normal group velocity dispersion (GVD) regime in condensed media. There are various rea-

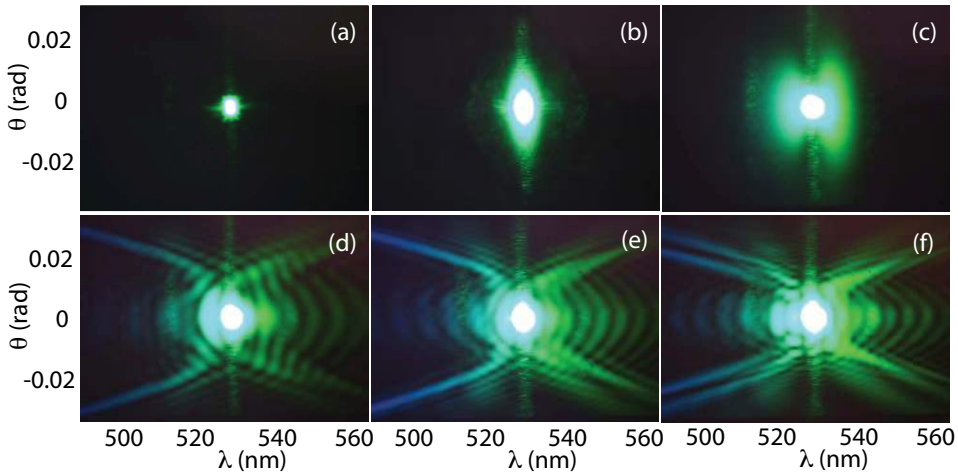

Fig. 5.1. Measured filament spectra for increasing input energy from (a) 0.5 μJ, (b), (c) and (d) from 1.3 to 1.5 μJ, (e) 2 μJ and (f) 5 μJ.

sons for this choice but the main motivation lies in the fact that filaments in condensed media such as water or fused silica occur in the *cm* range, and not tens of meters as in gases. Furthermore these materials are transparent at readily available wavelengths (in our case 527 nm) for femtosecond laser sources and at these wavelengths most condensed media exhibit normal GVD. The experimental layout used for theses experiments is shown in Fig.1.7 where the Kerr medium is a glass cell filled with pure water. The input laser pulse is generated by a Nd:glass laser system (Twinkle, Light Conversion Ltd., Vilnius, Lithuania) that operates at a fundamental wavelength of 1055 nm with pulse of 1 ps duration, FWHM. Frequency doubling with a particular configuration studied so as to also compress the pulse gives us pulses at 527 nm with a duration FWHM of 200 fs and energy in the 4 mJ range. This pulse is then strongly attenuated and the final energy is varied from 1 to 6 μJ using a polarization rotator in combination either with a polarization selective mirror or a Glan-Taylor polarizing cube. This range of energies in combination with a focusing $f = 50$ cm (so that the collimated beam diameter at the sample input facet is of the order of ~ 100 μm) gives stable, single filaments in 2-4 cm of water. Lower energies do not give rise to filaments and higher energies lead to local breakdown inside the sample or to multiple filamentation, all effects that give confused and non optimal spectra. Fig.5.1 shows the measured (θ, λ) with increasing input energy. In (a) we have the input Gaussian pulse. Increasing the energy so that the pulse is above the self-focusing critical power without actually forming a filament in the 3 *cm* water sample we observe first a large increase in the

spatial (i.e. angular) spectrum (b) followed by a strong space-time reshaping (c). This reshaping is related to both self-focusing (leading to an increase of the spatial frequencies) and self-phase modulation (leading to an increase in the temporal spectrum). These two effects occur simultaneously and are tightly connected to each other so that at different angles we observe different spectra. This is the spectral counterpart of spatiotemporal coupling. The spectrum in (c) is taken just before the nonlinear focus of the self-focusing pulse: this propagation regime is characterized not only by a spatial but also by a temporal compression of the input pulse (see the first four graphs in Fig.1.8). This may seem in contrast with the fact that ultrashort pulses in a dispersive medium should actually spread in time, yet the temporal compression is the result of this initial space-time focusing stage: the most intense part of the pulse, located at the very center of the Gaussian profile, will suffer the strongest reshaping. It will self-focus more efficiently than the rest of the surrounding pulse, increasing further the peak intensity. Measuring the FWHM of this intensity peak will therefore result in a temporally compressed pulse that is, however, surrounded by a large background that has not yet focused. Increasing the pump energy leads, with a very abrupt transition, to the formation of a relatively stable (from shot to shot and for increasing energy) structure in the spectrum dominated by two features: a marked conical emission (spectrum at $\theta \neq 0$ rads) and an axial ($\theta \sim 0$ rads) emission. The axial emission in the case of water is often somewhat weaker than that observed in other media, for example fused silica (see for example Fig.3.8 or 3.18), but still shows the same common features. Increasing even further the input energy gives similar features in the spectrum although with some additional features such as multiple split conical emission tails.

At this point we may make use of the technique described in detail in chapter three and derive the group velocities of the pulses associated to the measured conical emission tails.

Analyzing the complete series of spectra summarized in Fig.5.1 gives the group velocity values shown in Fig.5.2(a). The circles give the averaged (over all frequencies) group velocity and the error bars indicate the mean standard deviation. The standard deviations are always of the order of 0.1% indicating that the group velocity is indeed practically constant. There is only a single pump energy value (1.4 μJ) for which the error bars are relatively large ($\sim 2\%$), indicating that here the group velocity is not so constant. We shall return to this issue later on when considering the pulse dynamics at the nonlinear focus and for the moment we shall concentrate on the propagation after this point. Fig.5.2(a) not only tells us that the spectra are well represented by stationary conical waves (the small error bars indicate that k_z is a linear function of ω) but it also tells us that the pump pulse is splitting into two pulses propagating with opposite group velocities (in the moving frame

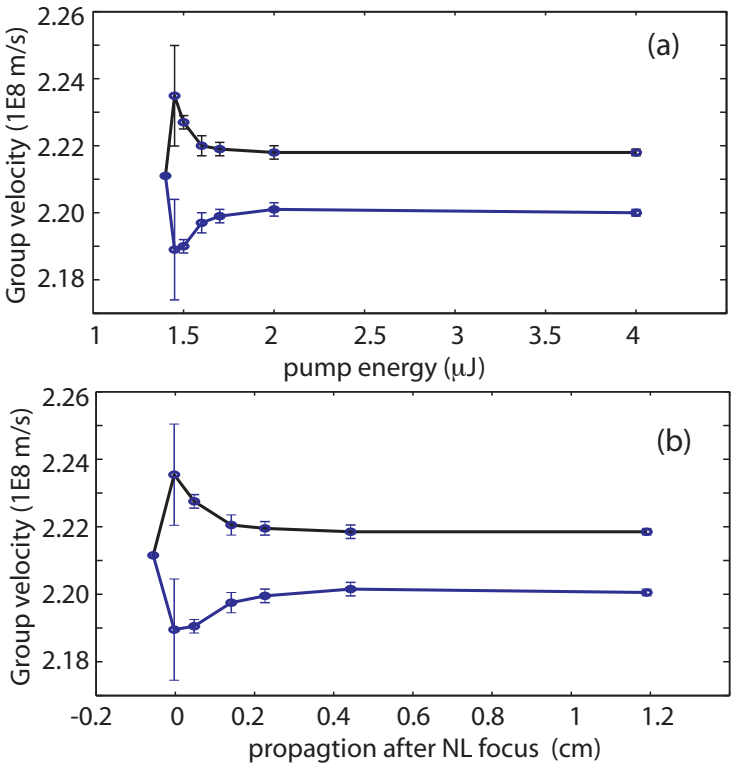

Fig. 5.2. Group velocity, derived from the spectra shown in Fig.5.1 of the spontaneously formed X waves with varying input energy (a) and versus the propagation distance after the nonlinear focus estimated using Eq.1.29 (b)

of the input pulse). The blue shifted conical emission tails correspond to a superluminal pulse, the red-shifted tails to a subluminal pulse. So the conical emission is intimately connected to the intensity peak splitting that occurs during filamentation. This is a natural consequence of the spontaneous formation of conical waves: the conical emission or off-axis propagating waves create an interference pattern that is seen as an intensity peak that travels at group velocity that depends not on the pulse carrier frequency (as in standard Gaussian pulses) but on the particular pulse shape (i.e. through the α parameter in eqs. 2.12,2.13). It is possible to graph the same data as a function of the propagation distance after the nonlinear focus. The overall sample length is fixed at 3 cm but increasing the input energy leads to a shift of the nonlinear focus toward the laser as described by Eq.1.29. Therefore increasing the pump energy has a very similar effect to that of increasing the effective filament propagation length inside the Kerr medium. The nonlinear focus is defined as the point at which the pulse reaches its highest intensity

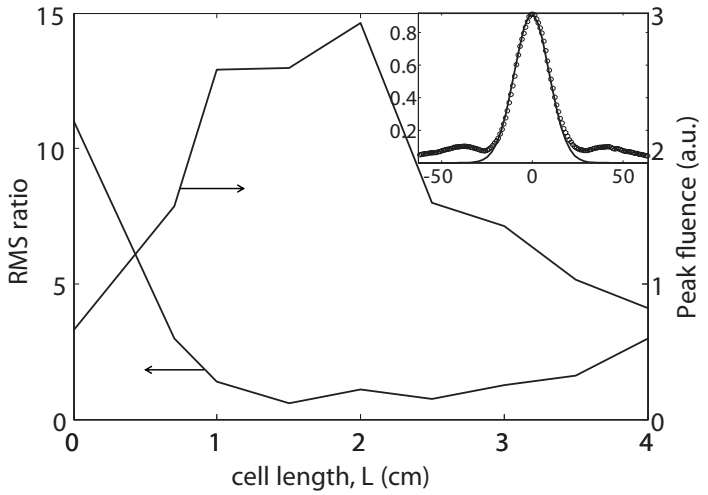

Fig. 5.3. Left axis: Ratio between the root-mean-squared deviations of the measured near field profiles with respect to Townes and Gaussian profiles. Right axis: peak intensity in arbitrary units. The inset shows the measured near field profile at L=3 cm.

and therefore is most likely to give the largest variation in the pulse spectrum. We therefore estimate the position of the nonlinear focus to coincide with the 3 cm sample length for an input energy of $E = 1.45$ μJ and then evaluate the filament length that will vary proportionally to $1/\sqrt{E}$. The result is shown in Fig.5.2(b) that highlights two different regimes:

1. just after the nonlinear focus, characterized by a strong pulse reshaping process, and
2. far from the nonlinear focus, characterized by a smoother propagation during which the spectrum hardly changes indicating a relaxation toward linear propagation.

We have not yet mentioned what happens just before the nonlinear focus. This issue has been studied in detail for example by Moll et al.[24] who showed that an input Gaussian pulse will self-focus and spontaneously transform into what is known as the Townes profile. This profile was first reported in Ref.[6] and was discovered as the stationary state of the nonlinear Schrödinger equation and indeed was proposed ([6]) as the possible candidate to explain the apparent stationary-like propagation of optical filaments. However it is now known that the Townes profile is stationary but also unstable against perturbations. This means that the slightest perturbation will either push the pulse toward catastrophic collapse (eventually arrested by

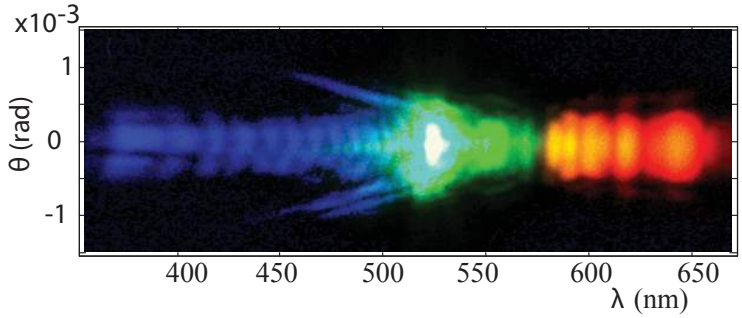

Fig. 5.4. Experimentally measured X wave spectrum generated in a 10 m filament in air.

nonlinear saturating mechanisms) or toward diffraction. Nevertheless Moll et al. have shown that the initial spatial contraction stage of the input pulse is dominated by a spatial reshaping into the Townes profile. This may also be confirmed by simply measuring the near-field fluence profiles of filaments versus propagation distance. One may try to fit the measured profiles with Gaussian and Townes profiles and then compare the "goodness" of these fits, for example by taking the ratio of the root mean square deviation (or standard deviation) of the data points from the fitting curve for the Townes and Gaussian profiles. A value below 1 indicates a good fit to the Townes profiles, a large value indicates a good fit to the Gaussian curve. Fig.5.3 shows such a result obtained with a 200 fs, 527 nm focused into water. The great advantage of using water is that by properly building the cell we can easily change the propagation length, even in very small steps. As can be seen, the RMS ratio indicated in the graph starts off very large, indicating a good fit with a Gaussian profile as expected as this is how we chose our input pulse. Propagation inside the Kerr medium leads to a reshaping into Townes profile indicated by the RMS ratio that falls below 1. At the same time the pulse intensity also reaches its maximum value, indicating that we are at the nonlinear focus. After this point the RMS ratio increases again however this does not actually correspond to retransformation back into a Gaussian pulse but rather into a pulse shape that is neither Gaussian nor Townes. The inset in Fig.5.3 shows a near-field profile taken for L=3 cm and clearly shows how the central peak has developed side wings thus explaining the poor fit with Gaussian or Townes profiles. In other words the instability of the pulse unavoidably leads to a reshaping that we may tentatively associate to the spectral reshaping observed at the nonlinear focus, i.e. precisely to the point at which the catastrophic collapse is blocked.
All this leads us to a loose picture of the filamentation dynamics in which the input pulse self focuses toward a Townes state. The instability of this state

manifests itself at the nonlinear focus and, after an initial but very quickly evolving process, leads to the spontaneous formation of conical waves that split in time and relax toward a linear propagation regime. An important feature of these results is the strong pulse splitting that seems to occur in practically all media and under a broad range of input conditions indicating that is a very robust and general feature.
Before going into more detail in the pulse splitting dynamics it is interesting to note that we may verify that the spectra correspond to conical waves by fitting directly the maximum intensity profiles using the two parameter curves described by eqs. 2.12,2.13. In certain situations it is possible to simplify further this analysis by fitting with a curve that actually has no free parameters [87] . Indeed if we consider the Taylor expansion of the $k(\omega)$ relation (Eq 2.15) some materials and for some wavelength ranges satisfy the conditions $1/6k_0'''(\omega-\omega_0)^3 << 1/2k_0''(\omega-\omega_0)^2$ and $1/2k_0''(\omega-\omega_0)^2 > 0$. In this case the conical wave spectrum will exhibit hyperbolic X-like tails, corresponding to what are usually referred to as X waves and will be symmetric. This, for example, is precisely the case for water with a pump wavelength of 527 nm and over a relatively large 100-200 nm spectral range. Under such conditions the X waves are well described by Eq.2.16: asymptotically, i.e. for large frequency shifts Ω and angles, this relation may be approximated by $k_\perp = \sqrt{k_0 k''}\Omega$. Therefore in order to check if the spectrum corresponds to that of an X wave it is sufficient to verify that the X tail $k_\perp$ (far from the pulse center) depends linearly on frequency and with a slope that is determined by the second order dispersion. This method is particularly convenient (when applicable) due to the fact that often the central region is saturated and the spectral details are not visible. As an example consider the spectrum shown in fig.5.1(e): the slope of the X tails is 1.01 ± 0.1 fs/μm which is in excellent agreement with the expected slope (for an X wave), 0.94 fs/μm. As a further example consider fig.5.4. This shows an experimentally measured spectrum generated from a 10 m long filament in air. The filament was first reflected from a wedged glass plate so as to reduce its intensity and then sent into a home made imaging spectrometer. The slope of the tails is found to be 1.5 ± 0.2 fs/μrad which is very close to the value 1.68 fs/μrad predicted using parameters for air given in ref.[88].

5.2 Normal, anomalous and zero group velocity dispersion

Most filamentation experiments are conducted in the normal group velocity dispersion regime. This is due simply to the large availability of ultrashort laser pulse in the visible or near infrared range and to the fact that experiments are usually carried out in highly transparent materials, a feature that

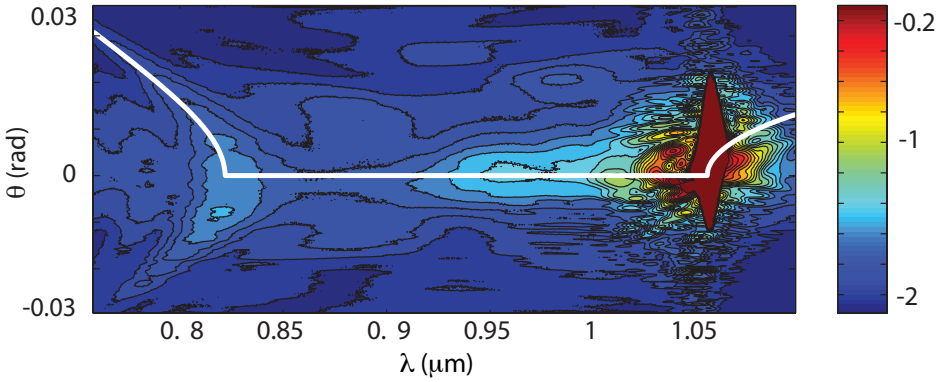

Fig. 5.5. Experimentally measured filament spectra generated with a 200 fs input pulse in water centered at 1055 nm. Input energy is $E = 15$ μJ.

is usually (but not always) connected to the presence of normal GVD. But of course one may ask how the spectra and conical waves are modified when passing into the anomalous dispersion regime. We have seen in chapter 2 that in anomalous GVD the stationary conical wave takes the form of the O wave and close to the zero GVD point it takes the form of the Fish wave. Experimentally this may be verified by measuring the spectra for various wavelengths [89]. The input wavelength was tuned from the near UV region into the near IR: in water the zero GVD wavelength is 1000 nm and a clear transition from X shaped spectra toward O shaped spectra is observed thus confirming the prediction based on the hypothesis that the filamentation process is characterized by the spontaneous formation of conical waves.

At this point one may object that the same dependence may be assumed looking at the modulational instability profiles predicted for a plane wave in the presence of Kerr nonlinearity. Fig.1.3 shows precisely a growth in the (θ, λ) spectrum that is X shaped in normal GVD and O shaped in anomalous GVD [53]. However there are important differences between the two models, differences that finally favor the conical wave model. Indeed when we speak of modulational instability we are referring to an energy transfer from the high intensity pump wave to the unstable modes. This energy transfer occurs through a phase-matched nonlinear interaction (Four Wave Mixing for Kerr nonlinearity) which in turn implies that only even terms (k'', k'''', ...) will play a role in defining the final shape of the spectrum. All odd terms (k', k''', ...) will cancel out in the energy and momentum conservation relations resulting in perfectly symmetric spectra regardless of the pump wavelength [90, 91]. Yet we know that close to the zero GVD wavelength third order dispersion becomes important and may dominate the dispersion landscape, severely distorting the conical wave spectrum that assumes half-X or Fish

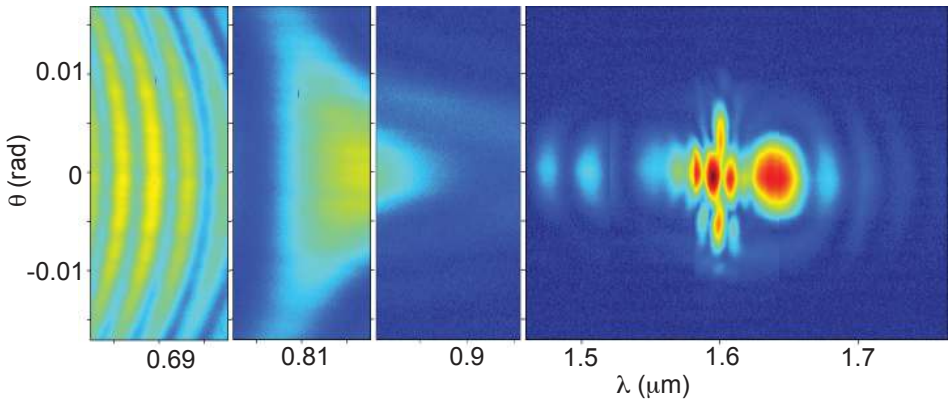

Fig. 5.6. Experimentally measured filament spectra generated with a 200 fs input pulse in fused silica centered at 1600 nm. Input energy is $E = 15$ μJ.

like profiles, as shown in chapter 2. Fig.5.5 shows an experimentally measured spectrum produced by a filament in a 3 cm long water cell with a pump pulse of 200 fs, 1055 nm central wavelength and 15 μJ input energy [53]. This input energy is rather large if compared to measurements performed to similar experiments at 527 nm. Indeed water exhibits a very strong linear absorption peak around 1100-1200 nm that is therefore partly compensated by the large input energy. The spectrum clearly shows a strongly asymmetric shape with an O-like feature in the anomalous dispersion region (above 1000 nm) and a hyperbolic tail near 800 nm in the normal dispersion region. These features constitute what we call the "Fish" spectrum.

Fish waves and soliton fission in optical fibers.

It is important to realize that the features in the Fish spectrum do not correspond to distinct pulses in the near field but rather are the manifestation of a single pulse. This may be checked for example by performing numerical simulations that reproduce the experimental spectrum and by then performing a Gated Angular Spectrum characterization: although the near field profile is quite complicated, in correspondence to the temporal slice at the main intensity peak the spectrum shows the full Fish shape (i.e. hyperbolic tail and O-like head), i.e. the full Fish spectrum may be identified with a single peak in the near field (the solid white line in the figure shows the best fit obtained using the conical wave relation that matches the overall features). This finding is in strong contrast with similar features observed in optical fibers [78]. In fibers extended supercontinuum generation is obtained by pumping close to the zero-GVD wavelength. This process is characterized

by soliton fission (in the anomalous GVD region) and by the formation of a blue-shifted dispersion wave. Leaving aside the specific names used for fibers (e.g. solitons, dispersion waves) or in bulk (Fish waves) the physics appear to be quite similar: in both cases pulse splitting is observed in the anomalous GVD region along with a strong energy transfer to a specific blue-shifted wavelength in the normal GVD region. This similarity becomes even stronger if we note that the equation describing the resonant transfer of energy from the soliton at frequency ω_s, to the dispersive wave at frequency ω_{dw}, is given by [78]

$$-\beta(\omega_{dw}) + \beta(\omega_s) + \frac{\omega_{dw} - \omega_s}{v_{gs}} + \Delta\beta_{NL} = 0, \tag{5.1}$$

where β is the effective fiber mode wave-vector, v_{gs} is the soliton group velocity and the last term is a nonlinear correction to the soliton wave-vector. This equation may be reinterpreted as the 1D version of the more general Three-Wave-Mixing equation (Eq.1.35) or of the conical wave relation (Eq.1.33), where the soliton plays the role of the pump pulse. In the full 3D case the nonlinear correction term in Eq.5.1 may be neglected due to the fact the wave-vectors are no longer constrained along the propagation direction and are aligned along conical surfaces so that the nonlinear phase-shift will not accumulate. In other words, what we identify as the blue-shifted tail of a Fish wave is referred to as a dispersion wave in fiber physics. However this is where we find a difference between the two cases: in the full 3D system the conical nature of the wave-packets will sustain the existence of localized and stationary peaks. Near the zero-GVD wavelength, the spectrum associated to these peaks is constituted by the full Fish spectrum, i.e. a red-shifted O-like feature with a blue-shifted hyperbolic tail. On the other hand, if we limit the physical dimensions of the system to 1D as in a fiber then no conical-like propagation is possible: a solitary red-shifted peak is still observed but this is no longer stationary and splits into a series of first order solitons (soliton fission). Furthermore the blue-shifted peak is no longer part of an extended conical emission and therefore behaves simply as a dispersive wave and will propagate with a delay with respect to the red-shifted solitons forming a separate, temporally broadened pulse [78].
Fig.5.5 is relative to water but fig.5.6 shows the measured spectrum of a filament generated in fused silica glass [53]. Zero GVD is close to 1290 nm and the pump was chosen at 1600 nm, i.e. apparently well into the anomalous dispersion region. However at these wavelengths for glass the condition $1/6k_0'''(\omega-\omega_0)^3 << 1/2k_0''(\omega-\omega_0)^2$ is not satisfied even for relatively small frequency shifts. In any case it is clear from the measurement that the spectrum is reaching well into the normal GVD region and a clear Fish-shape is observed. This confirms that our interpretation may be extended to any

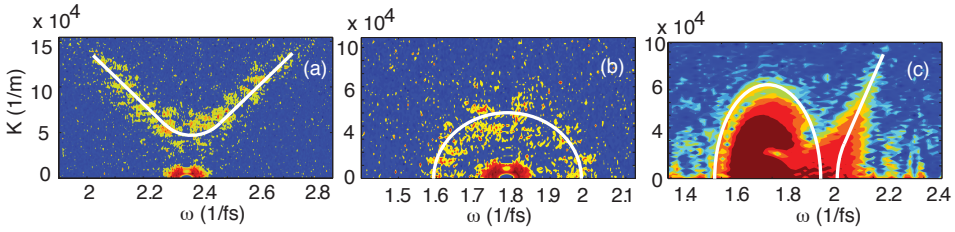

Fig. 5.7. Numerically simulated spectra of white noise amplified by a long (200 fs) and wide ($r = 1$ mm) super-gaussian pump pulse in normal GVD (a) and anomalous GVD (b). Independently of the pump frequency noise is amplified along symmetric regions in the spectrum. Close to the zero GVD frequency and with a short (20 fs) and small ($r = 50$ μm) pulse white noise is amplified with an asymmetric Fish-like profile. The white lines are a guide for the eye.

medium but is also highlights the fact that great care should be taken in distinguishing between normal and anomalous GVD. More often than not it is necessary to consider the full dispersion landscape and this is neither normal nor anomalous. Overall we could conclude that X and O waves are simply a partial manifestation (due to limited spectral bandwidth) of the more general Fish waves.

Fish waves and Modulational Instability

We now compare the measured spectra and predictions based on the X wave model with those given by modulational instability theory. Generally speaking the energy redistribution leading to the formation of Fish waves occurs through some kind of phase or nearly phase matched process so why are the spectra not symmetric? The answer lies in the fact that modulational instability analysis is valid only if performed on stationary states, which in the case shown in Fig.1.3 are plane and monochromatic waves. Yet self focusing and in general filamentation leads to a very tightly focused intensity peak, a condition that may be very far from the plane wave case so that the amplified spectrum may be very different. In order to verify this we performed numerical simulations based on the nonlinear Schrödinger equation. The input beam was taken as a gaussian pulse with a 200 fs duration (that may still be roughly considered as monochromatic) and with a radius of 1 mm (that may be considered as a plane wave). The peak intensity of this pulse was chosen to be very high and was superimposed on a background of low intensity, white (in frequency and angles) noise. Figures. 5.7(a) and (b) show the spectrum after a few mm of propagation, a distance sufficient

to start to amplify the white noise without inducing any significant distortion on the pump pulse. In normal GVD the noise is clearly amplified along a hyperbolic-like symmetrical surface that then becomes elliptical in anomalous GVD, exactly as predicted by modulational instability theory. However fig.5.7(c) shows exactly the same simulation with a very short 20 fs and very small $r = 50$ μm pulse and the amplified noise clearly shows a strongly asymmetric and Fish-like shape. This would apparently imply that energy transfer from the pump pulse to the amplified spectral components is occurring with a violation of the phase matching constraints. The tightly focused pulse has a large spatial spectrum so that, although the longitudinal components of the wave-vectors must satisfy momentum conservation, the transverse components are allowed a certain indetermination $\Delta k \sim 1/r$. A similar reasoning may be applied also to the energy conservation constraint. In other words, it is the tight spatial and temporal localization of the pulse at the nonlinear focus and within the filament that allows a departure from strict phase-matching and the formation of asymmetric spectra that correspond to stationary conical waves.

5.3 Pulse splitting and X wave formation

Filamentation is therefore characterized by a relaxation toward a stationary or combination of stationary conical waves. What remains to be explained is what determines the particular conical mode observed in the spectrum and if there is any connection with pulse splitting. The principal candidate for explaining the spectral reshaping and redistribution of energy within the pulse is Four Wave Mixing. This is the lowest order nonlinear process that will occur in a kerr medium and will certainly occur at the intensities reached within the filament (of the order of TW/cm^2 in condensed media). Although this may seem relatively obvious it is not so obvious how the Four Wave Mixing process should be treated (or if it may be treated) analytically. The standard approach based on a phase matching requirement between plane and monochromatic waves will not give useful results: the phase matching curves will be symmetric an essentially identical to the maximum gain curves for modulational instability. An alternative is to treat the Four Wave Mixing process bearing in mind that the generated wave modes are not plane waves but rather X waves. In other words the phase matching condition should be applied between two tightly localized pump waves with a signal and idler X wave. In order to do this we may take the simplified conical relation Eq.2.16. This equation may in turn be written in a slightly different form that is slightly easier to treat analytically:

$$K_\perp(\Omega) = \sqrt{k_0 k_0''(\Omega - \bar{\Omega})^2 + 2k_0\bar{\beta}}. \tag{5.2}$$

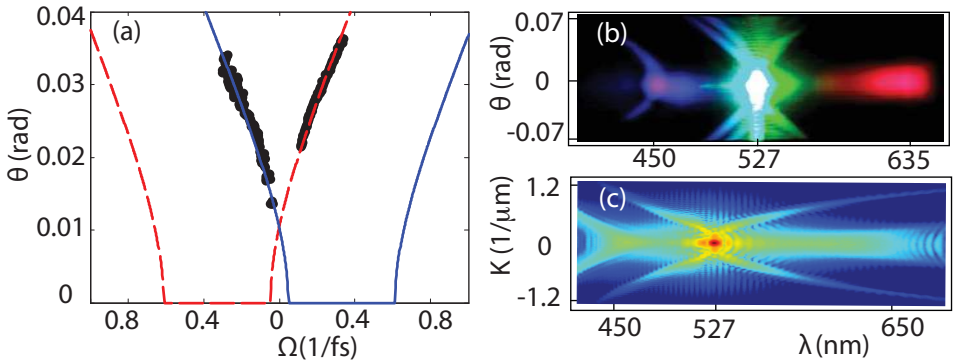

Fig. 5.8. (a) full circles give the measured (θ, Ω) maximum intensity distribution for conical emission generated by 527 nm, 2 μJ, 200 fs laser pulse in 3 cm of water. (b) measured (θ, λ) spectrum using a low resolution grating so as to capture a large spectral range in a single shot. The X tails originating at 450 nm and 635 nm are clearly visible. (c) numerical simulation showing the same features as in (b).

$\bar{\Omega}$ and $\bar{\beta}$ are free parameters: $\bar{\Omega}$ is the X wave central frequency and $\bar{\beta}$ is a correction to the wave-vector. Within the approximation of a symmetrically (with respect to $\bar{\Omega}$) excited X wave, the phase and group velocities are given by [56]

$$v_p = \frac{\omega_0 + \bar{\Omega}}{k(\omega_0 + \bar{\Omega}) - \bar{\beta}}, \tag{5.3}$$

$$v_g = \frac{1}{k'(\omega_0 + \bar{\Omega})}. \tag{5.4}$$

Two X waves with opposite and equal group velocities in the moving reference frame of the input pulse will split with a group velocity mismatch (GVM) given by

$$GVM = \frac{1}{v_g^{(1)}} - \frac{1}{v_g^{(2)}} = 2k_0''|\bar{\Omega}|, \tag{5.5}$$

where we have used

$$v_g^{(1,2)} = \frac{1}{k'(\omega_0 + \bar{\Omega})} \sim \frac{1}{k_0' \pm k_0''|\bar{\Omega}|}. \tag{5.6}$$

Phase matching is now imposed between the two degenerate localized pump waves and the signal and idler X waves: energy conservation gives $\bar{\Omega}_s = -\bar{\Omega}_i$ and momentum conservation gives $2k = k_s + k_i$ where the X wave signal and idler X wave-vectors are given by $k_{s,i} = k(\omega_0 + \bar{\Omega}_{s,i}) - \bar{\beta}_{s,i}$. The pump

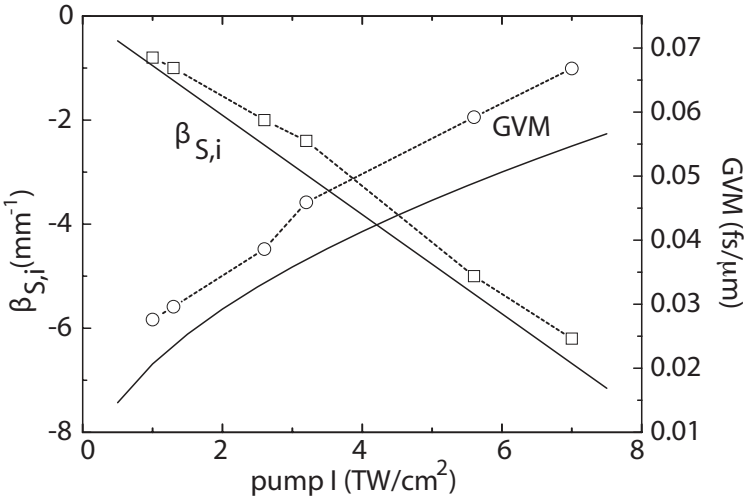

Fig. 5.9. Dotted curves and symbols show the $\bar{\beta}$ and GVM values obtained from numerical simulations. Each point represents a separate simulation: the peak intensity was controlled by varying the nonlinear absorption coefficient. Solid lines show the predicted values using analytical relations, eqs.5.8 and 5.9.

wave-vector $k = k_0 + \Delta k$ is corrected by a positive (in self focusing media) nonlinear phase shift term Δk that accounts for the self induced nonlinear phase shift. Although the pump is localized rendering a proper evaluation of the nonlinear correction somewhat complicated we may tentatively approximate this term taking the plane wave value $\Delta k = \omega_0 n_2 I/2c$. The nonlinear correction is not included in the weak signal and idler X waves due to the fact that the conical nature of the X waves implies that energy does not flow axially but rather along a conical surface therefore preventing pump-induced phase accumulation to take place. Using the Taylor expansion $k(\omega_0 + \bar{\Omega}_{s,i}) \cong k_0 + k_0' \bar{\Omega}_{s,i} + k_0'' \bar{\Omega}_{s,i}^2/2$ the phase matching constraint leads to

$$\bar{\beta}_s + \bar{\beta}_i - k_0'' \bar{\Omega}_{s,i}^2 = -2\Delta k. \tag{5.7}$$

Recalling that $\bar{\beta}$ and $\bar{\Omega}$ are free parameters we realize that there are an infinite number of X waves that satisfy this relation. Among all possible couples we should however choose those whose spectra cross the pump spectrum, located around $\Omega = 0$, $K_\perp = 0$ as these are the most energetically favored since they will not need to grow from noise but from the more effective pump self-phase modulation. This condition together with Eq.5.2 leads to $\bar{\beta}_{s,i} = -k_0'' \bar{\Omega}_{s,i}^2/2$. We therefore finally find the conditions for the X wave parameters:

$$\bar{\beta}_{s,i} = \frac{\omega_0 n_2 I}{2c} \tag{5.8}$$

$$\bar{\Omega}_{s,i} = \pm\sqrt{\frac{\omega_0 n_2 I}{c k_0''}}. \tag{5.9}$$

So the signal and idler X wave frequency shifts will be symmetrical with respect to the pump and will have frequency gaps given by $2|\bar{\Omega}_{s,i}|$. Equation 5.9 also predicts a dependence of the conical emission structure on the pump peak intensity I. We have already seen that when third order and higher terms are negligible in the material dispersion relation the conical emission spectrum will have a constant slope dictated by k_0''. The remaining spectral features such as the curvature close to the pump, the presence of a frequency gap and the entity of this gap are given by Eq.5.9.

Fig.5.8(a) shows the (θ, Ω) points of maximum spectral intensity for the spectrum shown in Fig.5.1(e). The solid and dashed lines give the best fits obtained with the X wave relation Eq.5.2 and parameters $\bar{\beta}_s = \bar{\beta}_i = -2.2$ mm^{-1} and $\bar{\Omega}_{s,i} = \pm 0.33$ fs^{-1}. As predicted by the simple analytical treatment given above we do indeed find that the signal and idler X waves have equal $\bar{\beta}$ and opposite $\bar{\Omega}$. These fits and the theory predict the existence of conical emission tails at relatively large frequency shifts. Repeating the measurements with a low resolution grating so as to acquire the spectrum over a large spectral range while maintaining the possibility to do this in single shot, such features may be indeed be observed. Fig.5.8(b) and (c) show an experimental spectrum and a numerically calculated profile that clearly show the expected X wave features, thus confirming the validity of this approach.

Eqs.5.8 and 5.9 also predict a clear dependence on the peak intensity reached within the filament. The solid lines shown in Fig.5.9 give the predicted $\bar{\beta}$ and GVM$= 2k_0''|\bar{\Omega}_{s,i}| = 2\sqrt{k_0'' \omega_0 n_2 I/c}$ with $n_2 = 1.6 \times 10^{-16}$ cm^2/W. These curves allows us to derive a peak intensity value within the measured filament of ~ 1.2 TW/cm^2. This is in close agreement with the peak intensities found in numerical simulations. More importantly, we may verify the model by comparing the analytical relations with those found in numerical simulations. The great advantage of numerical simulations is that we may easily track not only the output spectrum but also the peak intensity within the filament. We therefore performed a series of simulations all with identical input conditions (matching the experiment) with the sole exception of the nonlinear absorption. In water at 527 nm $K = 3$ (three photon absorption) and by varying the nonlinear absorption coefficient $\beta^{(3)}$ in the range 1.2×10^{-23} - 8×10^{-25} cm^3/W^2 the peak intensity reached within the filament varies from 1 to 7 TW/cm^2. Obviously we do not have the possibility to observe a similar variation in experiments: it is not possible to artificially vary the nonlinear absorption coefficient without physically changing

material (and therefore all other parameters) and increasing the input energy does not necessarily lead to a significant increase in peak intensity in the filament. Fitting the numerically simulated spectra with Eq.5.2 we may therefore track the variation of $\bar{\beta}$ and $\bar{\Omega}$ versus intensity. The dashed lines and symbols in Fig.5.9 show a very good agreement with the analytically predicted dependence. The agreement is not perfect and this may be due to certain approximations adopted in order to derive analytical relations such as the particular form used to describe the nonlinear phase shift, approximated with that expected for a plane wave although the pump pulse is actually tightly localized. However the overall agreement is notable indicating that a deep understanding of the nonlinear processes dominating ultrashort pulse filamentation may be obtained within the X wave model. As a last note, this model predicts that pulse splitting should occur within the filament simply as a result of phase matching in the nonlinear dynamics. This remains true within the approximations of the model:
(i) strict energy and momentum conservation
(ii) the description of the pump and X waves in terms of their carriers only. The symmetry resulting from this analysis might be violated if higher order dispersive and nonlinear effects (e.g. self-generated plasma) are no longer negligible. In other words certain settings (material, pump wavelength and profile etc.) may lead to the formation of asymmetric X waves and even the apparent formation of a single X wave if one of the two is much weaker in intensity than the other.

5.4 Axial and conical emission: the "shocked" X wave

We have shown how interpreting a particular feature, the conical emission, in terms of spontaneous formation of X waves leads to a simple model which may explain many features of the whole filamentation process. Yet in this discussion we ignored the role of the strong axial emission that is also a common feature of filamentation in all media (see for example Figs.5.1,5.4,3.8 or 3.18). In the next section we shall study the Townes profile modulational instability and we will see that at the nonlinear focus the conical and axial spectral components are connected through a longitudinally phase matched Four Wave Mixing process ([92]). However in the fully formed filament this connection is not so obvious as the axial spectrum is usually far more extended in frequency than the conical counterpart so that imposing a Four Wave Mixing process as the connection between the two would require accepting a strong violation of energy conservation. Indeed axial and conical emission are usually treated as independent phenomena and explained using independent models. For example the axial spectrum has been explained as the result of the formation of shock (or very steep) fronts in the pulse in-

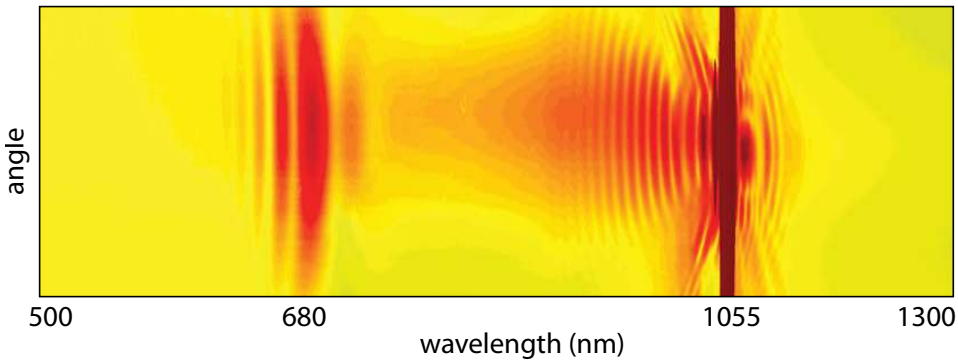

Fig. 5.10. Experimentally measured filament spectrum with a 1 ps, 1055 nm, 5 μJ laser pulse propagating in 15 cm of fused silica.

tensity profile [93]. Studying the on-axis intensity profile an optical shock front is observed and explained to be the result of space-time focusing and self-steepening. This shock front will result in a broad pedestal in the spectrum and is identified with the white light (or axial) continuum. However others have given an explanation of the filamentation spectra in which conical emission and axial continuum are different aspects of the same process: X wave formation. As we have already discussed in chapter 1, the "effective three wave mixing" model proposed by Kolesik et al. ([31, 33]) interprets the same stationary mode profiles used within the X wave model as the result of a phase matched three wave scattering process. If one relaxes the phase matching constraint so that momentum conservation is not strictly imposed then the spectrum will become a volume: the stationary mode profile will expand around the $\Delta k = 0$ lines and the X tails will be connected by a relatively intense axial continuum. This understanding therefore also predicts that the axial continuum should extend only between the X tails: one X tail at the pump wavelength and the other X tail at some shifted wavelength (that is determined in the X wave model by the peak intensity through Eq.5.9) represent the boundary of the axial continuum. Numerical results seem to verify this prediction and Fig.5.10 shows an experimental measurement of a filament spectrum generated with a 100 nm, 1 ps, 5 μJ pulse in 15 cm of fused silica glass. The spectrum clearly shows the pump X tails at 1055 nm and an X tail at 680 nm. Clearly the axial continuum extends between these X tails and shows a sharp drop in energy at 680 nm with no continuum extending further. We expect to see the same behavior also toward the infrared region that is however invisible in this measurement due to the sharp cut-off in the silicon detector sensitivity around 1000-1100 nm.

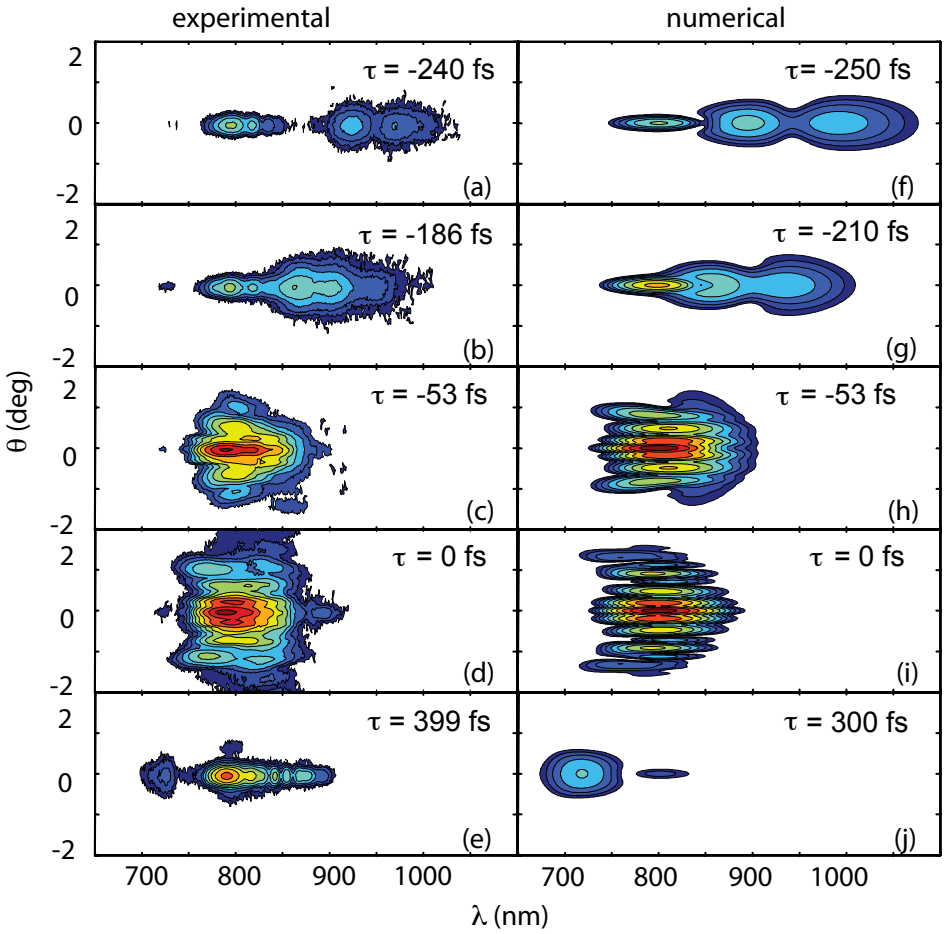

Fig. 5.11. (a)-(e): Experimentally measured Gated Angular Spectra for increasing delay within the filament wave-packet. Input parameters are $\lambda =$ 800 nm, $E = 3$ μJ, duration 100 fs, in 4 cm of water. (f)-(j): numerically simulated GAS experiment with the same input conditions and accounting also for linear, dispersive propagation in the output imaging optics.

It is now interesting to question how this axial continuum should be considered within the X wave model ([94]). Indeed stationary X waves do not exhibit a strong axial spectrum so clearly this is an additional feature related to the filamentation process. An appropriate tool that may give us some insight into the physics of the connection between the axial and conical spectra is the gated angular spectrum (GAS) technique described in chapter 3 ([94]). We should recall that ultrashort laser pulse filamentation is characterized by pulse splitting and that the resulting pulses are strongly compressed in time. It is therefore necessary to use a very short 20-30 fs gate

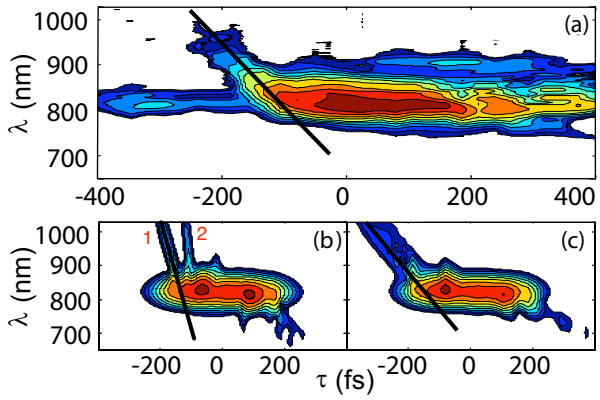

Fig. 5.12. (λ, τ) diagram of the filament characterized in Fig.5.11. (a) experimental data - the solid line highlights the clearly chirped red-shifted axial continuum, (b) numerically simulated pulse inside the water sample showing the presence of two separate red-shifted contributions, one slightly chirped, the other with practically no chirp, (c) the same as in (b) but accounting also for the effect of linear dispersive propagation in the output imaging optics.

pulse in order to apply the GAS technique successfully. The experimental setup is shown in Fig.3.9: a 50 cm focal length lens is used to focus the 100 fs, 800 nm input pump pulse into a 3 cm long sample of pure water. The gate pulse is generated by a white-light parametric amplifier (Light Conversion Ltd., Vilnius, Lithuania) that delivers tunable 20 fs pulses in the 500-700 nm wavelength range. Fig.5.11(a)-(e) shows the experimentally measured (θ, λ) spectra for various relative delays τ of the 20 fs gate pulse within the filament wave packet. Zero delay is defined with respect to a linearly propagating Gaussian pulse. For negative delays (the leading part of the wave-packet) a red-shifted axial emission is observed. With increasing delay (moving toward the wave-packet center) the red-shifted emission increases in frequency. A dependence of frequency on time within a laser pulse is known as chirp and is treated in chapter 3. One of the principal physical effects that leads to pulse chirp is propagation in dispersive media. Normal group velocity dispersion, the same encountered in water at wavelengths shorter than 1000 nm, will lead to a shift of longer wavelengths toward the front of the pulse, just as observed in Fig.5.11. For delays close to the pulse center Fig.5.11 shows evident conical emission and finally, the trailing edge of the wave-packet is characterized again by axial emission this time blue shifted but still with the same chirp sign observed on the leading part of the pulse. The observed pulse chirp renders somewhat difficult any association of the various spectral features to well defined time slices within the pulse

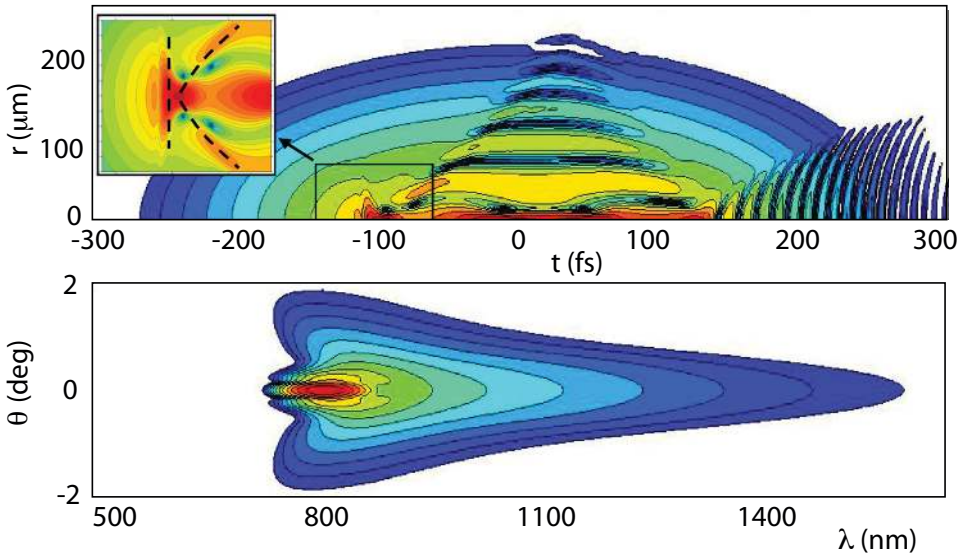

Fig. 5.13. numerically simulated filament wave-packet within the Kerr medium. The top graph shows the near-field. The inset is an enlargement of the leading split pulse highlighting the conical tails and the steep, rising shock front. The bottom graph shows the gated spectrum for this same split pulse that clearly shows the simultaneous presence of both conical emission and axial continuum. These features are explained by the particular nature of the X wave that is not truly stationary in the sense that the central intensity spike presents a steep shock front.

inside the sample at the moment of their generation. We therefore resort to numerical simulations performed with the same input conditions of the experiment. By applying numerically the same GAS experiment method it is possible to compare the numerical simulation with the actual experiment. The results are shown in Fig.5.11(f)-(j) and reproduce quite precisely the most important features that we are interested in here, namely the chirped axial emission and the conical component. We note that in order to achieve this agreement it was necessary to also include the effects of (linear and dispersive) propagation in the optics experimentally used to collect and image the filament at the water sample output. Confident of the good agreement between numerics and experiment we may now plot the data in a slightly different format as shown in Fig.5.12 and focus our attention on the red-shifted axial continuum. The experimental (θ, τ) diagram (a) gives a clearer view of the chirped axial emission and also allows to conclude that the chirp is linear, thus giving a further indication that this chirp is due to dispersive propagation. Fig. 5.12(c) shows the same diagram as simulated numerically

accounting for propagation through optical lenses at the sample output and confirms once more the agreement between numerics and experiments. Finally Fig.5.12(b) shows the same result as in (c) but now without accounting for the external optics: the linear chirp has all but disappeared. Furthermore the axial continuum is also clearly separated into two distinct contributions (also seen as two partially overlapping peaks in Fig.5.11(a) and (b)). The first of these still maintains some linear chirp while the other has practically no chirp at all. We interpret the residual chirp to be due to dispersive propagation within the Kerr medium thus implying that the two contributions are originated at different points within the medium. Indeed the numerical simulation shows that after the first focusing and splitting process the wave-packet goes through a second spatiotemporal focusing stage that leads to a further splitting. The second red-shifted contribution (indicated with "2" in Fig.5.12(b)) clearly shows that the axial spectrum is generated within an extremely short event. The first contribution (indicated with "1" in Fig.5.12(b)) was generated at a shorter propagation distance and has thus acquired some chirp (due to the longer propagation necessary to reach the end of the sample) but, at the moment of generation was also concentrated within an extremely short temporal interval. Furthermore the solid lines in Fig.5.12 indicate that this short time interval is overlapped with the leading split pulse intensity peak. These results lead us to the conclusion that indeed Gaeta was correct in predicting that the axial continuum arises as the result of a shock front ([93]). Moreover if we interpret the intensity peaks in the near-field as the central peaks of spontaneously formed (or forming) X waves then we note how at the moment of formation the X waves are not actually stationary in the sense that they are characterized by a shock front that severely distorts the spectrum.

The presence of a shock front within the X wave is confirmed in Fig.5.13: the top graph shows the numerically simulated wave-packet near-field profile after 1.8 cm propagation, i.e. at the point in which the shock front reaches its steepest point (shortly after the pulse splitting event). The inset is an enlargement highlighting the trailing conical tails and the severe distortion of the leading part of the pulse that exhibits a very steep temporal shock front. Taking a gated angular spectrum of this same pulse (i.e. visualizing only the spectrum generated by this pulse within a 20 fs window) we see that indeed the spectrum is both conical and axial. This is what we may call a "shocked" X wave in order to distinguish the pulse from the true stationary X wave. Further propagation will lead to a relaxation of the shock front and the "shocked" X wave will therefore diffuse toward a finally stationary X wave.

The results shown for the red-shifted axial emission remain true also for the blue-shifted component with the only difference that the shock fronts form

on the trailing edge of the trailing split pulses. However it is important to note that it is well known that in normal GVD and with $n_2 > 0$ shock fronts will form on the trailing edge of the pulse. This is often explained as due to the higher intensity central region that will travel slower than the leading and trailing tails, resulting in an accumulation of energy and steepening at the pulse trailing edge [95]. This is also confirmed by Gaeta [93] and is used to explain the blue shifted continuum emission. Yet here we clearly observe rising shock fronts (i.e. on the leading edge of the pulse), apparently in contradiction with the standard theory of shock-front formation. This result finds a natural explanation within the X wave model: the leading pulse is characterized by superluminal propagation so that the intense peak will travel faster than the surrounding energy reservoir and steepen on its leading edge. In a similar fashion the subluminal peal will steepen on its trailing edge.

6

Filamentation Nonlinear Optics

The intensities reached within a filament may be extremely high, of the order of a few TW/cm^2 in condensed media and even a factor 100 times higher in gases. Furthermore the tightly focused intensity peak maintains its small diameter over many diffraction lengths. For example in water intensity peak diameters of the order of 20 μm are reached corresponding to a Rayleigh range shorter than 1 mm, yet the intensity peak is maintained within the filament over some centimeters. In air the situation is similar: peak diameters of the order of 100 μm yet the filament propagates for distances up to tens of meters, orders of magnitude further than the expected few-centimeter Rayleigh range. This is an ideal context, very high peak intensities over very long distances, in which to observe and exploit nonlinear optical effects.
The term "filamentation nonlinear optics" was first used by Chin et al. ([96]) to describe a series of nonlinear optical processes observed in air filaments such as self phase modulation, spatial self-cleaning, third harmonic generation and seeded Four Wave Mixing.
In this chapter we will focus our attention on filament mediated nonlinear processes in condensed media with particular emphasis on the interaction between the intense filament and a weak seed. We shall give an overview of the basic processes underlying the interaction and show how, starting from the X wave model, it is possible to predict and explain some results obtained in this regime ([97]).

6.1 Seeded filamentation: Cross Phase Modulation

6.1.1 Theory

A intense pump pulse in a kerr medium will experience a self-induced phase change that will depend on the pulses intensity profile. This effect goes under the name of self-phase modulation (SPM) and is related to a physical variation of the material refractive index which may be described by the

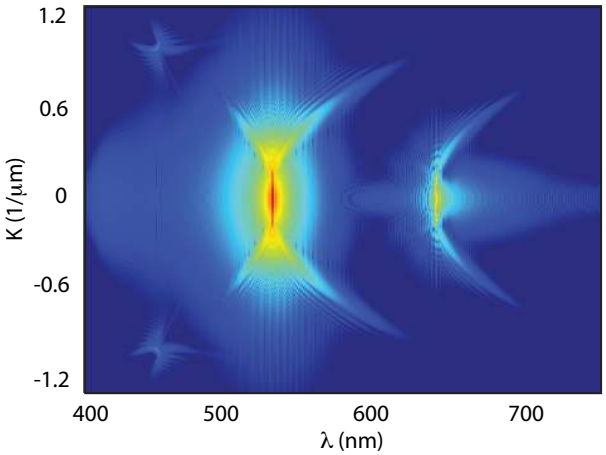

Fig. 6.1. Numerically simulated spectrum of a weak 640 nm weak seed pulse in the presence of an intense optical filament in water. SRS is not switched on so that only Kerr effects take place.

simple relation $n = n_0 + n_2 I$ where n_0 is the linear refractive index and n_2 is the nonlinear refractive index excited by the pulse intensity I. As an example of the entity of the index variation due to SPM consider the case of water: $n_2 \sim 2 \times 10^{-16}$ cm^2/W so that a peak intensity of 1 TW/cm^2 gives an index variation of $\sim 2 \times 10^{-4}$. This is a relatively small variation but due to the fact that it occurs over extremely short temporal or spatial scales it may lead to very visible effects such as self focusing or frequency broadening (see chapter 1). Due to the fact that SPM is related to a physical change in the medium we should expect the variation in refractive index to be felt also by another optical pulse that is co-propagating with the pump pulse. This is called Cross-Phase Modulation (XPM). Equations 1.19 and 1.20 are two Nonlinear Schrödinger equations, one for the strong pump pulse the other for the weak seed pulse, that are coupled through the XPM term $\propto A_p A_p^* A_s$. Lets consider a specific situation and take a closer look at the physical interaction occurring through this coupling term.

In order to be able to distinguish between a pump pulse and a seed pulse these must have for example different carrier frequencies. We may therefore assume that the pump and seed pulses are spatially and temporally overlapping at some point inside the Kerr medium and, due to material dispersion, they will have different group velocities. The intense pump pulse will create a (nonlinear) polarization wave $P \propto A_p A_p^* A_s = I_p A_s$: this may be considered as a wave that has the same envelope of the pump pulse but oscillates at the carrier frequency of the weak seed. XPM that will occur in the full 3D+1 case. This is just another way of explaining a scattering process in which the weak seed is scattered from the nonlinear polarization induced by

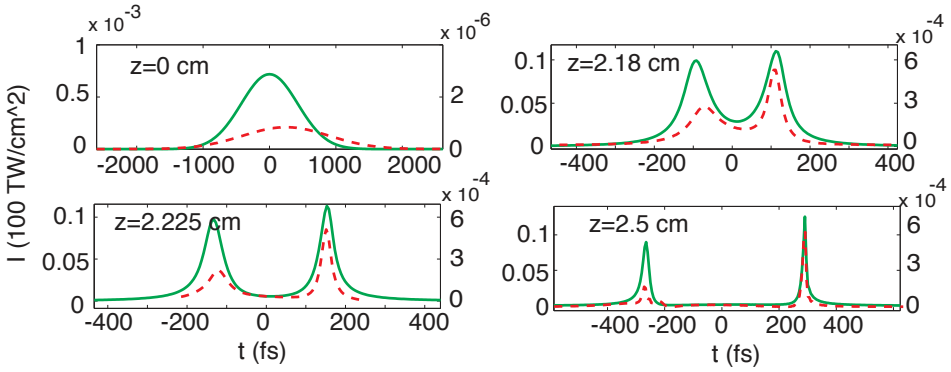

Fig. 6.2. Numerical simulation of a 527 nm, 200 fs pump pulse that forms a filament in presence of a weak seed at 640 nm. Solid lines are the on-axis intensity profiles for the pump filament (left axis). The dashed lines show the on-axis intensity profiles of the weak seed (right axis) that is reshaped through XPM. Clearly the seed develops peaks that mimic the pump profile and travel at the same group velocity of the pump split pulses.

the strong pump.

The weak seed pulse which may be approximated by a plane monochromatic wave at the input with transverse wave-vector and frequency $(0, \omega_0)$, is therefore scattered by this perturbation into an output wave (K_{perp}, ω). This scattering process should preserve the total momentum however, due to the tight spatial localization of the intensity peak within the filament, we need not impose transverse momentum conservation [98, 53]. Therefore, imposing only longitudinal k_z momentum conservation leads to

$$k_{z,out}(K_\perp, \omega) = k_{in}(0, \omega_0) + \frac{\Omega}{v_{pol}} \tag{6.1}$$

where, for energy conservation $\Omega = \omega - \omega_0$ and the polarization perturbation velocity $v_{pol} = v_{g,p}$. The important point here is that Eq.(6.1) identical to Eq.2.13 with $\beta = 0$ and $\alpha = k_0' - 1/v_{g,p}$. In other words, the scattered wave forms a stationary (non-dispersive) conical wave packet that propagates with a group velocity given by that of the input pump. This is rather surprising as it implies that we may arbitrarily choose the carrier frequency ω_s for the seed pulse and this will determine the phase velocity, but the group velocity is determined solely by the pump pulse and may be very different from the expected value $v_{g,s} = d\omega/dk|_{\omega_s}$.

This is a rather surprising discovery and indicates the possibility to generate stationary X waves or more in general conical wave states through XPM. Optical filaments could be the ideal candidate pump pulses for this purpose, not so much because they themselves are already conical waves but most

importantly because of the very high peak intensities reached within the filament and that render the XPM particularly efficient. As a demonstration of this idea Fig.6.1 shows a numerically simulated spectral reshaping of a weak 640 nm seed in the presence of a filament generated by a 3 μJ, 200 fs, 527 nm pump pulse. The pump pulse shows strong X features as already discussed in the previous chapters but the seed too, initially Gaussian, has reshaped into an X wave as predicted by the simple theory outlined above. In order to prove that the pump and seed pulse travel at the same velocity in Fig.6.2 we show the on-axis intensity profiles of the pump (solid lines) and seed pulses (dashed lines) for various propagation distances z. At the input both profiles are Gaussian but the intense pump soon initiates a filament and splits in two. These two pulses travel super and sub-luminally with respect to the input pump wavelength but also with respect to the seed at 640 nm. This leads to the formation of the red and (weaker) blue shifted conical emission (Fig.6.1) and the same conical emission is also responsible for the formation of the peaks appearing in the seed profile and that indeed travel locked with the pump pulses.

6.1.2 Experiments

Figure 6.3 shows the experimental setup used to investigate the interaction between a week seed signal and a much stronger pump that undergoes filamentation. The pump pulse, generated by a Nd:glass laser (Twinkle, Light Conversion Ltd., Vilnius, Lithuania) has a wavelength of 527 nm, a pulse duration of 1 ps and energy was limited to 1-10 μJ while the seed, generated from a parametric amplifier (TOPAS, Light Conversion Ltd., Vilnius, Lithuania) may be tuned continuously across the visible range into the infrared region. The pulse duration in the visible range is 500 fs and energy is limited to 100-250 nJ. A variable delay line ensures the possibility to change the relative delay between pump and seed pulses and optimize the overlap within the Kerr medium.

Figure 6.4(a) shows a measured spectrum for the case in which the pump pulse has not yet formed a filament. This was obtained by fixing the water sample length to 4 cm and varying the input energy until some significant self-focusing (i.e. broadening the spectrum) is observed but without a clear formation of X shaped features. This corresponds to an input energy of about $1.4 - 1.5$ μJ with a collimated beam diameter of 90 μm. The 500 nm seed energy was 250 nJ with a larger beam diameter of 170 μm in order to render less critical the spatial overlap between pump and seed beams. No effect is seen on the seed spectrum unless the delay is changed so that the pulses overlap toward the end of the water sample, i.e. in the region in which the pump reaches its highest intensity. In this condition the observed

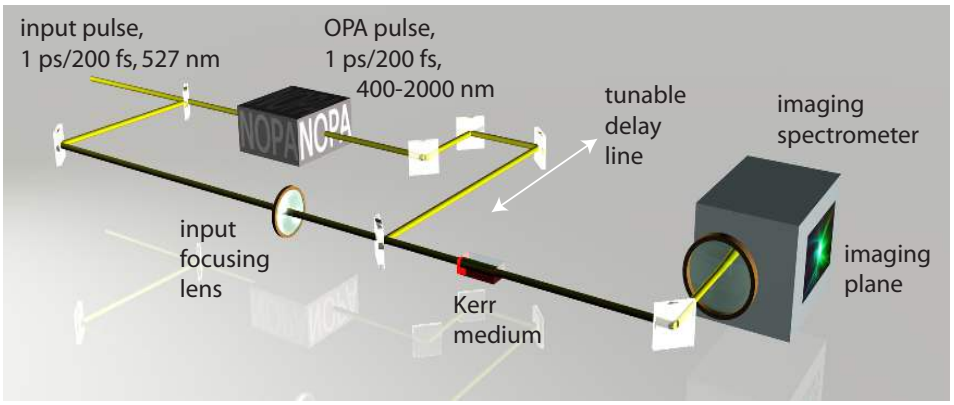

Fig. 6.3. Experimental layout for Filament nonlinear optics based on seeded interactions between a strong pump pulse and a tunable-wavelength weak probe pulse.

spectrum is shown in Fig.6.4(a). This spectrum was captured in full color (Nikon D70) but in the original image the pump spectrum at 527 nm showed no particular features as these were covered by a relatively strong scattering of green light. By removing the red and green channels of the color image and enhancing the blue channel we obtain the spectrum shown Fig.6.4(b). A weak blue-shifted conical emission tail is now visible also around the pump wavelength. This is a signature of the onset of filamentation and the formation of an X wave (although the filament is not fully formed). The input Gaussian seed has also developed a clear conical emission. The group velocities calculated from the conical emission of the seed and pump pulses are $2.33 \pm 0.02 \times 10^8$ m/s and $2.35 \pm 0.1 \times 10^8$ m/s, respectively. The two velocities are practically equal as predicted by our theory for XPM-induced conical emission.

Increasing the input pump energy will lead to the formation of a filament and the appearance of clear X shaped features around the pump wavelength. In Fig.6.5 we show this case with the seed now tuned to 490 nm: as expected the seed is still reshaping with a marked blue conical emission. Proceeding as before, if we take the blue shifted tails around the 527 nm pump wavelength, these give a group velocity of $2.237 \pm 0.004 \times 10^8$ m/s while the seed conical emission gives us $2.27 \pm 0.06 \times 10^8$ m/s, values which are still equal to each other within the experimental error. In Fig.5.2 we showed that the group velocity of the split pulses changes during the filament propagation. The experimental spectra in figs.6.4 and 6.5 (and the relative group velocities) confirm that the weak seed is locally reshaped into an X wave with an intensity peak that follows the same evolution of the pump pulse, as ob-

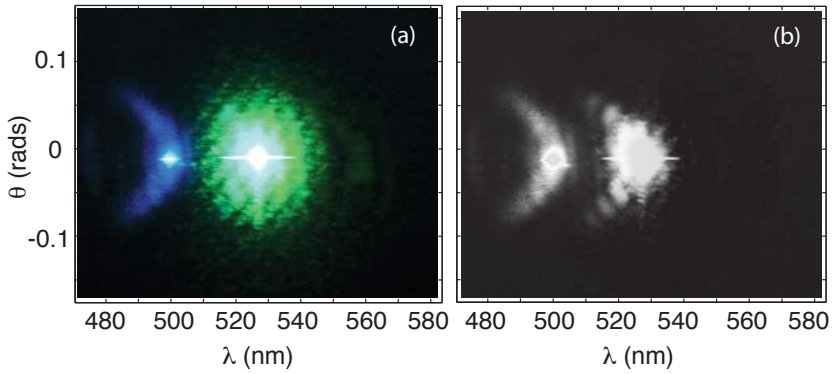

Fig. 6.4. Experimentally measured spectral reshaping of a 500 nm seed pulse with a self-focusing intense 527 nm pump pulse. (a) is the full color image acquired with a Nikon D70 camera. (b) is the same image in black and white after having eliminated the red and green channels so as to render visible the conical emission originating from the pump.

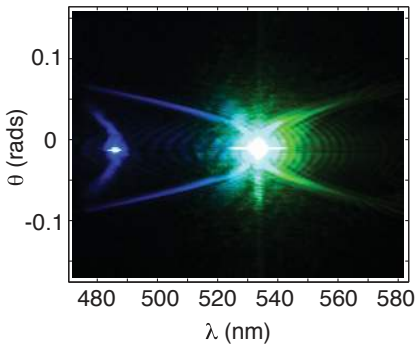

Fig. 6.5. Experimentally measured spectral reshaping of a 490 nm seed pulse with a self-focusing intense 527 nm pump pulse. The pump pulse forms a filament as is evident from the strong conical emission. Strong reshaping of the seed pulse is observed with the formation of a pulse that is locked in group velocity to one of the split pump pulses.

served also in the numerical simulations (Fig.6.2).

These measurements clearly confirm the predictions based on XPM-indiced reshaping. Now we may try to tune the seed wavelength over a broad spectral range in order to verify if other nonlinear processes occur. In particular we may expect Four Wave Mixing and Stimulated Raman Scattering.

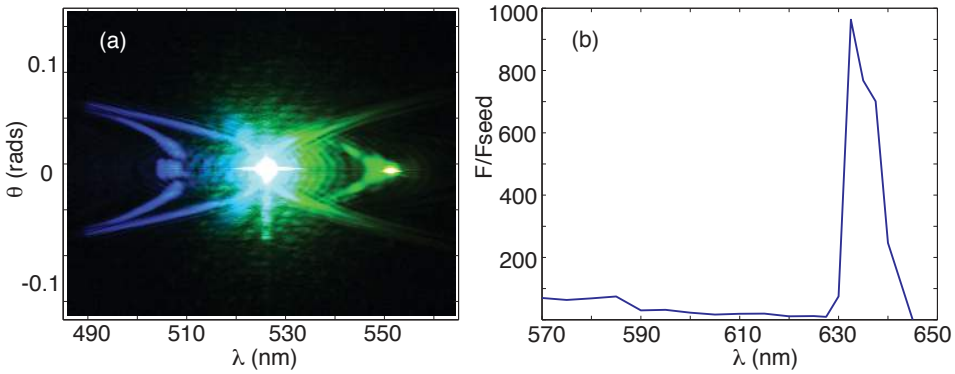

Fig. 6.6. (a) Experimentally measured spectrum with a seeded filament in 3 cm of water. Seed wavelength is 550 nm, idler generated by FWM is at 505 nm. (b) Experimentally measured gain of seed pulse with varying input seed wavelength. A $\sim 80\times$ gain due to FWM is observed, with a bandwidth of 60 nm. The large $1000\times$ gain at $\sim$640 is due to Stimulated Raman Scattering

6.2 Seeded filamentation: Four Wave Mixing

Théberge et al. have proposed a beautiful experiment in which efficient Four Wave Mixing was excited within a 10-30 cm filament (generated in air by a 2 mJ, 800 nm pump pulse) and a tunable weak seed [99]. The process generated an idler wave tunable in the 475-650 nm range with maximum conversion efficiencies (from signal to idler) of the order of 15% (and up to 40% for filaments generated in Argon gas) giving an idler energy of 10 μJ. Using the experimental setup shown in Fig.6.3 it is possible to repeat a similar experiment in condensed media, with much shorter filament lengths and much lower input energies (μJ and not mJ for the pump, nJ and μJ for the seed).

Fig.6.6 shows a measured spectrum of a 3 μJ, 527 nm filament in water in presence of a weak seed tuned to 550 nm. Reshaping of the seed due to XPM is clear but now a third pulse at the idler wavelength (505 nm) has also appeared as a result of Four Wave Mixing. The idler signal also exhibits a clear X-like structure. Deriving the group velocities for the 2 pump pulses $v_{g,1}$, $v_{g,2}$), the signal ($v_{g,s}$) and the idler ($v_{g,i}$) we find

$$
\begin{aligned}
v_{g,1} &= 2.17 \pm 0.02 \times 10^8 \mathrm{m/s} \quad \text{(red-shifted tails)},\\
v_{g,2} &= 2.236 \pm 0.005 \times 10^8 \mathrm{m/s} \quad \text{(blue-shifted tails)},\\
v_{g,s} &= 2.236 \pm 0.006 \times 10^8 \mathrm{m/s},\\
v_{g,i} &= 2.248 \pm 0.01 \times 10^8 \mathrm{m/s}.
\end{aligned}
$$

These values indicate that the seed, idler and leading pump X pulse are all traveling with the same group velocity. We measured the gain at the

seed wavelength by taking the ratio between the peak fluence of the output signal with respect to that of the input seed pulse. This does not give the total gain in energy due to the fact that the input seed is somewhat larger than the tightly focused pump filament but rather a measure of the "local" gain within the seed pulse. Figure 6.6(b) shows that the gain is roughly a factor 80 over a large 60 nm bandwidth. Tuning the seed further away leads to a decrease in the FWM efficiency, yet a huge 1000× increase in gain is observed around 637 nm. This wavelength corresponds to the expected wavelength shift induced by Stimulated Raman Scattering (SRS) in water. The bandwidth of the gain peak also corresponds to the $\sim$ 200 $cm^{-}1$ reported in literature ([98]) therefore confirming that indeed this large gain may be ascribed to SRS.

6.3 Raman X waves

SRS is a resonant nonlinear process by which energy from an incoming pump pulse may be transferred to a Stokes signal at a red-shifted wavelength that depends on the particular material. This energy transfer is mediated by rotational or vibrational levels of the medium and the phase matching constraints are automatically satisfied in this interaction. Therefore the main limitation to SRS frequency conversion with ultrashort laser pulses is no longer related to momentum conservation but rather to group velocity mismatch that leads to detrimental temporal walk-off between the pump and the Stokes pulses. In order to appreciate the effect of GVM let us consider the case under study, i.e. water with a pump pulse at 527 nm and a Stokes signal at 637 nm. The GVM calculated using the known water Sellmeier coefficients [54] is 28 ps/m. This implies that a 1 ps pulse will split by a pulse duration after 3.5 cm, so practically no significant reduction of the SRS conversion efficiency will be observed in a 2-3 cm long water cell. However we noted that in the first cm of propagation within the water cell no SRS was measured. On the contrary significant SRS and high seed gain were measured toward the end of the 3 cm water cell. This is in keeping with the fact that during the first cm the pump pulse still has a relatively low peak intensity. Longer propagation leads to the formation of a filament with much higher peak intensities but also characterized by pulse splitting with a significant temporal compression. Numerical simulations give a pulse duration in this regime of the order of 50 fs and therefore the splitting length will be only 1.8 mm.

Yet our measurements show a very large 1000× gain in the peak fluence at the Stokes frequency indicating that the SRS process is still rather efficient. This may be easily explained with a model in which the seed is reshaped by XPM: an intense (with respect to the input seed profile) peak is formed that

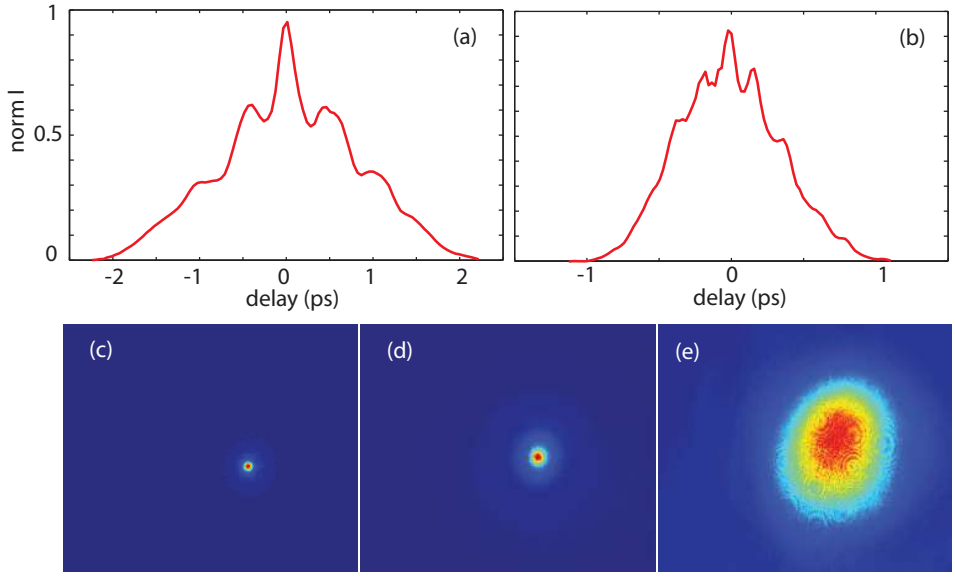

Fig. 6.7. (a) Autocorrelation trace of the pump filament, $E = 3.4$ μJ. The trace shows the presence of three split pulses with a duration FWHM of 70 fs. (b) Autocorrelation trace of the Stokes signal at zero delay. The trace shows 2, maybe 3 split pulses, with a duration FWHM of 60 fs. (c) and (d) are the near field fluence profiles of the filament and of the Stokes pulse at the sample output. (e) is the input seed near field fluence profile.

is sustained by the surrounding XPM-induced conical emission and travels at the same group velocity of the pump pulse. This peak in the seed profile may then be amplified by SRS. In Fig.6.7(a) and (b) we show the autocorrelation traces of the pump filament and of the amplified Stokes signal at the water sample output and for the delay at which the maximum gain was observed. In order to perform these autocorrelation measurements great care was taken in imaging with a telescope the output facet of the water sample onto the nonlinear crystal used for the autocorrelation. Indeed the filament and Stokes pulses are X waves i.e. they are non-dispersive in the medium in which they spontaneously formed (water) due to the angular dispersion that cancels out diffraction and dispersion. But in air, due to the same angular dispersion the X waves will experience a strong anomalous dispersion and therefore spread in time. This problem may be avoided by using an imaging telescope that reconstructs the pulse in amplitude and phase at the nonlinear crystal surface. Some residual broadening is still expected due to propagation in the fused silica lenses but this may be avoided only with a much more complicated and expensive setup using parabolic mirrors. The

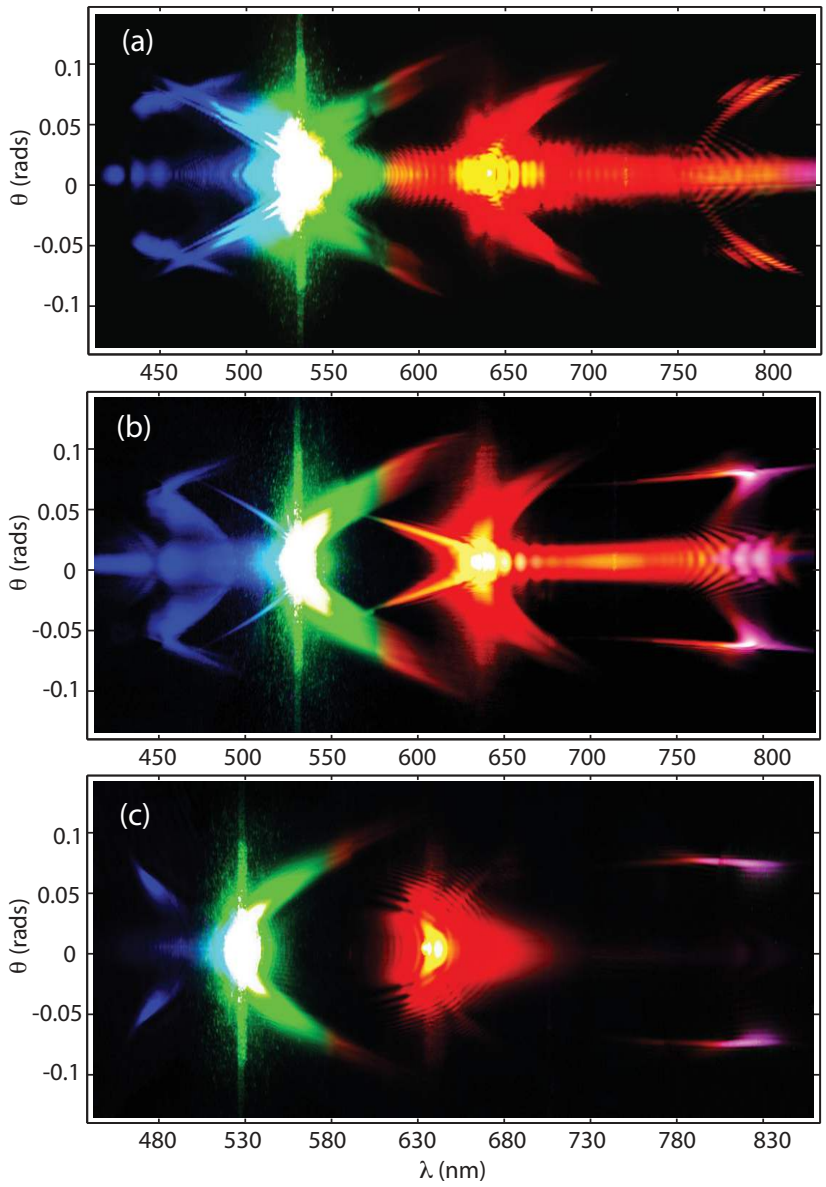

Fig. 6.8. Experimentally measured (θ, λ) spectra of a 527 nm filament in 3 cm of water (pump energy = 2.4 μJ, duration = 1 ps) with a weak $\sim$ 200 nJ seed at 637 nm for various delays τ between pump and seed. (a) $\tau = -400$ fs, (b) $\tau = 0$ fs, (c) $\tau = +400$ fs. The "switching" from one Raman X wave to the other is evident.

autocorrelation traces measured in this way show a large background with five spikes. The large background is in keeping with the nature of X waves that are indeed formed by a large energy reservoir and a central peak. Five

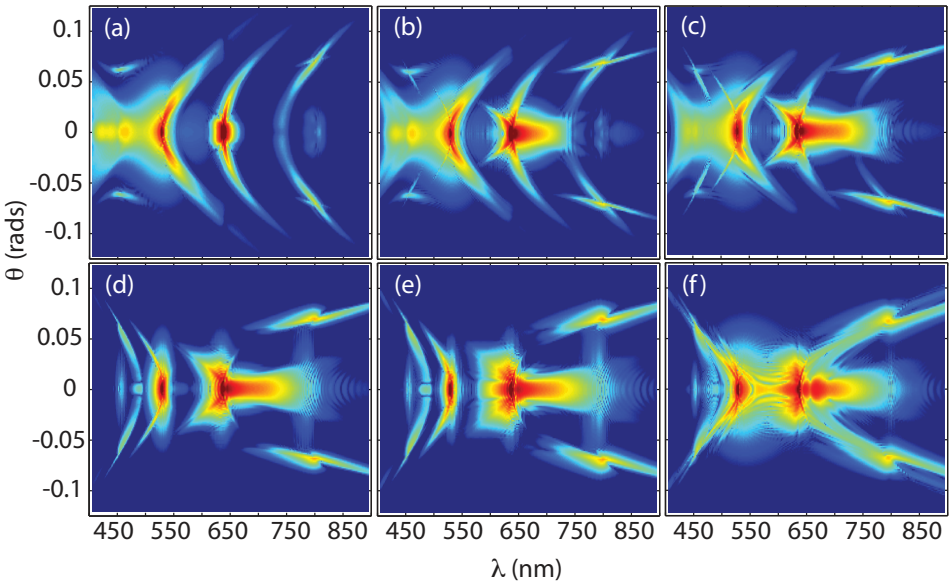

Fig. 6.9. Numerically simulated spectra with the same input parameters as in Fig.6.8 for various delays: (a) 200 fs (b) 400 fs, (c) 600 fs, (d) 800 fs, (e) 1000 fs, (e) 1200 fs. All plots are in a 7 decade logarithmic scale.

peaks in the autocorrelation traces indicate the presence of three intensity peaks in the near field and, assuming a Gaussian shape for these peaks we find FWHM durations of 70 fs for the pump pulses and 60 fs for the Stokes pulses.

Figures 6.7(c)-(e) show the near-field fluence profiles of the pump filament, the amplified seed and the input seed respectively. It is clear that the seed is amplified only in the close vicinity of the filament. The high spatial quality of the filament also leads to an improved spatial quality of the Stokes pulse with respect to the input seed. Note that (d) was obtained by strongly attenuating the beam so as to not saturate the CCD camera and therefore the large background, corresponding to the input seed (that is not amplified) is no longer visible.

We stress that the important result here is not the actual size or duration of the pulses themselves but rather the close correspondence between the filament and the amplified seed indicating a XPM-induced formation of intense X waves at the Stokes frequency that we may therefore call Raman X waves [100].

Figures 6.8(a)-(c) show three experimentally measured spectra of the full pump-filament and Stokes region. Due to the large spectra range covered these spectra are not truly single shot in the sense that they are composed of independent single shot measurements. The different spectra correspond

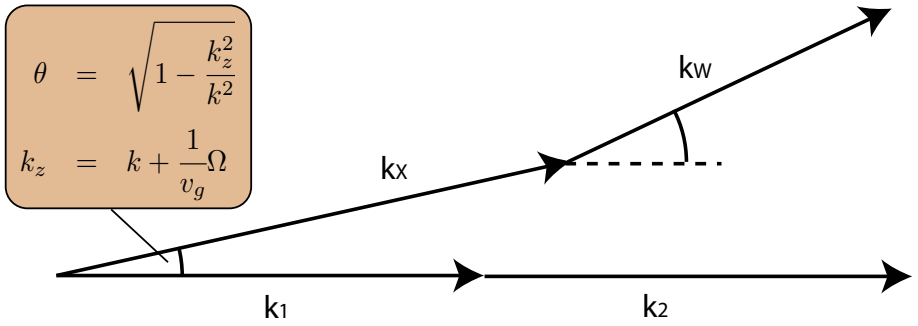

Fig. 6.10. Longitudinal phase matching diagram between 2 on axis photons $k_{1,2}$, 1 X wave photon k_X and 1 "whisker" photon, k_W.

to different input delays between the pump and seed pulses, with delay increasing in steps of 400 fs from (a) to (c). For the intermediate delay, which we arbitrarily define as "zero-delay", clear X features are observed around the pump wavelength as expected due to filamentation, and also around the stokes ∼640 nm wavelength (Raman X waves). It was shown in ref.[100] that the group velocities of the Raman X waves matches quite closely those of the pump X waves thus explaining, as mentioned earlier, the high gain. Furthermore a clear switching mechanism is observed from one Raman X wave (negative delay), to two Raman X waves (zero delay) and finally to a single but opposite Raman X wave for positive delays.

Numerical simulations were performed of this process and are shown in figs.6.9(a)-(f) which display the spectra in (θ, λ) coordinates (in air) for direct comparison with the experiment and for delay increasing in 200 fs steps. The effect of SRS is accounted for as a delayed Kerr nonlinearity with an exponentially damped response function, $R(t)$. The nonlinear term described in Eq.1.32 becomes

$$\begin{aligned} N(\mathcal{E}) &= k_0 \left[\frac{n_2}{n_0} T^2 \left(k_0(1-\alpha)|\mathcal{E}|^2 + \alpha \int_{-\infty}^{t} dt' R(t-t')|\mathcal{E}(t')|^2 \right) - \frac{k_0 \rho}{n_0^2 \rho_c} \right] \mathcal{E} \\ &+ i k_0 T \beta_K |\mathcal{E}|^{2K-2} \mathcal{E} \\ &\text{with} \quad R(t) = R_0 \exp(-\Gamma t) \sin \omega_R t. \end{aligned}$$

where $R_0 = (\Gamma^2 + \omega_R^2)/\omega_R$. Good agreement between numerics and experiments was obtained with a Raman fraction $\alpha = 0.16$, $n_2 = 3.2 \times 10^{16}$ cm^2/W, $\Gamma = 37.5$ THz, $\omega_R = 618$ THz. We note that the requirement of an overall agreement between experiment and numerics leads to a Raman gain coefficient that is actually 30% smaller than that reported in literature [98]. Using these parameters the same switching mechanism is observed as in the experiments. Notably this switching effect can only be observed with a

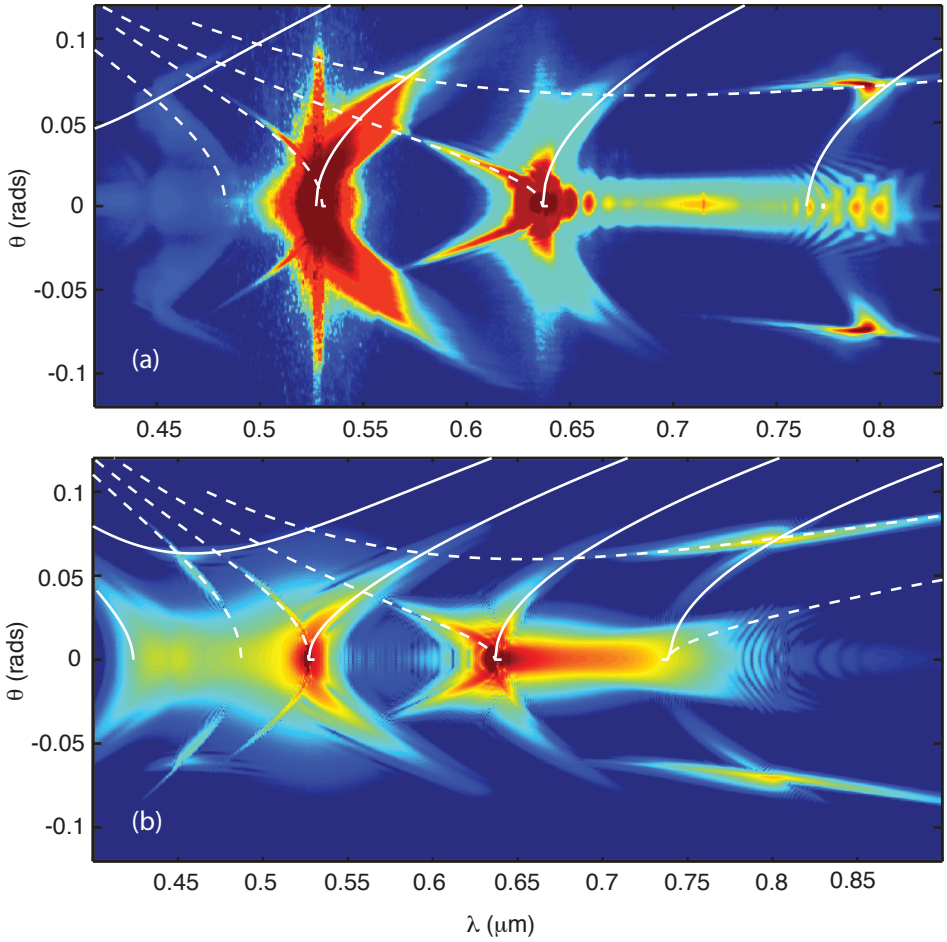

Fig. 6.11. Direct comparison between experimental (a) (taken from Fig.6.8(b)) and numerical (b) (taken from Fig.6.9(c)) spectra. The white lines are the best fits obtained using stationary conical wave profiles and longitudinal phase matching relations as described in fig.6.10.

somewhat limited range of input conditions and most importantly the input seed duration should be somewhat shorter than the input pump duration (in both experiments and numerics these durations were 490 fs and 1 ps FWHM, respectively). This may be explained by noting that the pump is split in two and we may change the delay so that the seed pulse has a significant overlap with only one of the pump X pulses and only a single Raman X wave is excited.

Let us now return to Fig.6.8(b) and draw attention to the off-axis features around 450 nm and 800 nm. Similar features are present in all three graphs in Fig.6.8 and are even visible, although very weak, in Fig.6.1. This last ob-

servation indicates that these features are not a direct product of the SRS process as they are present even when SRS is switched off (in the numerics). The proposed mechanism by which these "whiskers" are created is a longitudinally phase matched FWM between 2 degenerate on-axis photons and 1 photon belonging to an X wave. A scheme of this phase matching configuration is shown in Fig.6.10. We consider two possibilities:

1. the two degenerate on-axis photons belong to the 527 nm pump; the X wave photon belongs to one of the Raman X waves. The Raman X waves are described by the conical wave relation (shown for clarity in Fig.6.10). We have two possible choices for the Raman X wave that are distinguished by the different value of the only free parameter, the group velocity v_g. Due to the underlying XPM reshaping process these values are equal the pump X wave velocities, $v_{g,1}$ and $v_{g,2}$. This phase matching configuration will give rise to the two "whiskers" around 450 nm: each of the two "whiskers" is determined by the one of the two possible values for the group velocity.
2. the two degenerate on-axis photons belong to the Stokes signal; the X wave photon belongs to one of the pump X waves. Here too the angles of the pump photons are described by the conical wave relation using the same values for the group velocity as in 1., $v_{g,1}$ and $v_{g,2}$. This phase matching configuration will give the two "whiskers" located around 800 nm.

In Fig.6.11(a) we reproduce Fig.6.8(b) along with its numerical analog in (b). Both spectra are plotted in the same false color scheme so as to facilitate comparison. The white lines shows the phase matching curves described above. They are obtained from the relations

$$\theta^X_{p,s}(\lambda) = n(\lambda)\sqrt{1-\left(\frac{k_z}{kn(\lambda)}\right)^2}$$

$$\text{with} \quad k_z = k_{p,s}n_{p,s} + \frac{c}{v_g}(k - k_{p,s}) \tag{6.2}$$

$$\theta^w_{b,r}(\lambda) = \cos^{-1}\left(\frac{2k_{p,s}n_{p,s} - k\cos\theta^X_{s,p}}{kn(\lambda)}\right), \tag{6.3}$$

where $\theta^X_{p,s}$ is the X wave dispersion relation for the pump (p) and the seed (s), $k_{p,s} = 2\pi/\lambda_{p,s}$ is the wave-vector calculated at the pump and seed wavelengths and $\theta^w_{b,r}$ gives the "whisker" phase matching relation at the blue (b) $\sim$ 450 nm and red (r) $\sim$ 800 nm wavelengths. It is important to note that there is only one free parameter, namely the X wave group velocity v_g, that determines at the same time the shape of the pump and Raman X waves

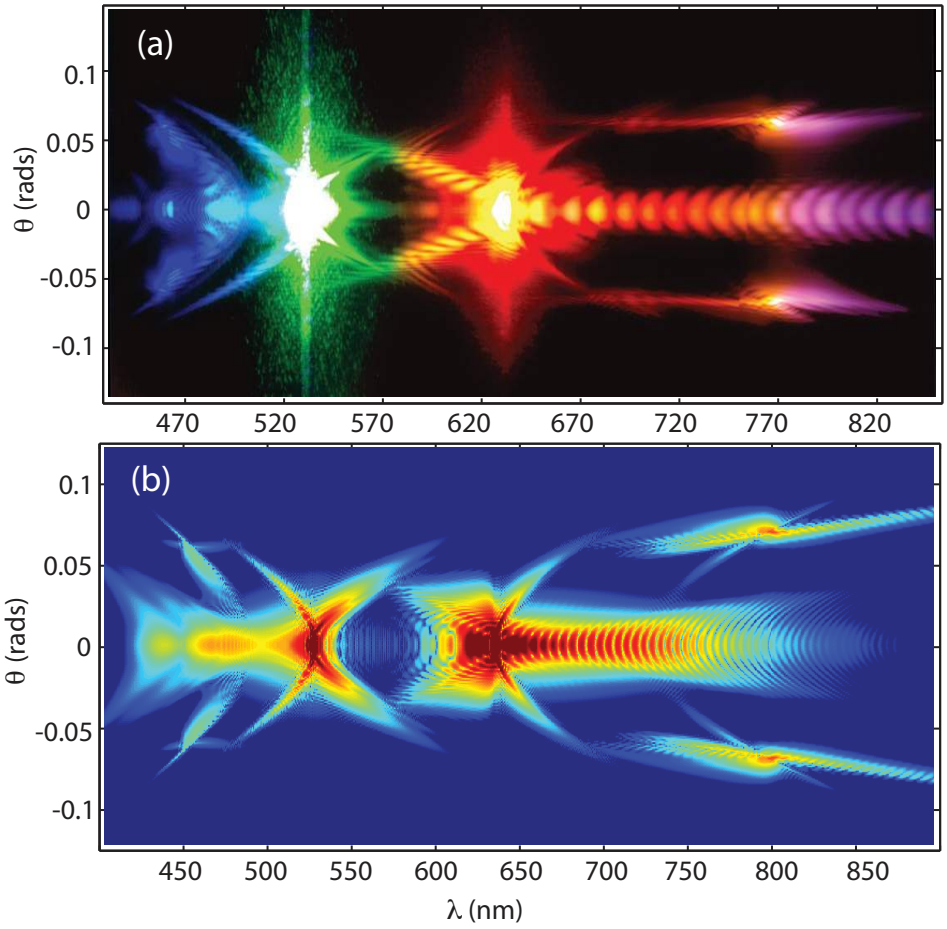

Fig. 6.12. With higher pump energies (3.4 μJ) more complex features and interference fringes due to multiple pulse splitting are observed but the overall structure remains unvaried. (a) experiment and (b) numerics.

and also the precise shape of the "whisker" patterns.
The solid lines correspond to a single value $v_g = v_{g,1,e} = 2.18 \times 10^8$ m/s for the experimental measurement (a) and to $v_g = v_{g,1,n} = 2.192 \times 10^8$ m/s for the numerical spectrum (b). The dashed lines give the pump and Raman X waves and the "whisker" features for $v_g = v_{g,2,e} = 2.238 \times 10^8$ m/s for the experimental measurement (a) and $v_g = v_{g,2,n} = 2.23 \times 10^8$ m/s for the numerical spectrum (b).
So far we have considered only spectra for a fixed input pump energy. Increasing the pump energy does not change the overall picture or behavior although some minor differences are observed. Figures 6.12(a) and (b) show the experimental and numerical spectra with a pump energy of 3.4 μJ. A first

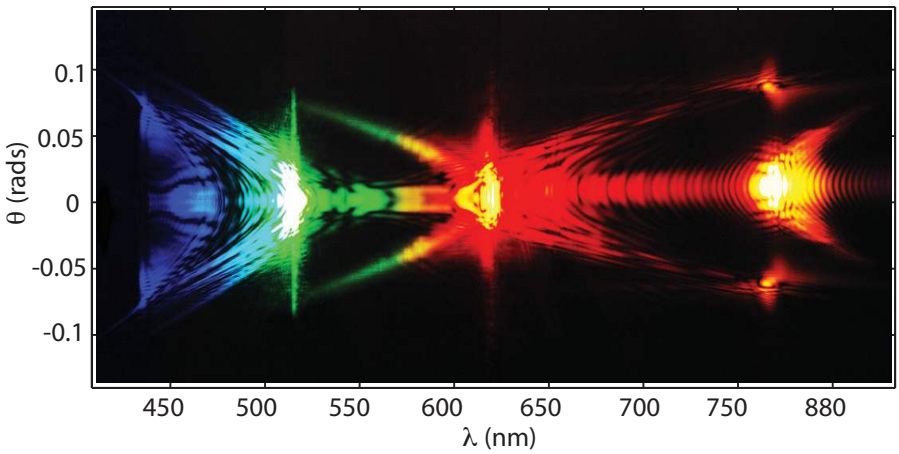

Fig. 6.13. Experimentally measured spectrum for a 3.5 μJ filament in ethanol. The seed is at the Stokes wavelength, 623 nm and the Raman X is so strong that it becomes the dominant feature in the spectrum. At $\sim$ 760 nm a spontaneously formed X wave at the second Stokes wavelength is observed.

observation regards the pump X waves: at lower energies the SRS process leads, for some delays, to a very strong depletion and eventually to a complete disappearance of one of the pump X waves (see for example figs.6.8(b) and (c)). At higher input pump energies the larger amount of energy in the pump avoids such strong depletion. Furthermore the spectra at 3.4 μJ show a generally more complicated profile with many interference fringes that are the result of multiple splitting processes, i.e. similar spectral features generated by temporally shifted split pulses.

As a final comment we note that in media with higher SRS gain, cascaded Raman X generation may be observed. Figure 6.13 shows a spectrum measured with a 3.5 μJ in 4 cm of ethanol. Ethanol has roughly 20$\times$ higher gain than water [98]: the seed at the Stokes wavelength of 623 nm [98] is strongly amplified and the Raman X waves become the dominant feature in the spectrum with a 50% energy conversion efficiency from the pump pulse. At the second Stokes wavelength 760 nm, a strong Raman X wave is also observed that carries about 20% of the input pump energy. A clear depletion of the pump X waves is visible (the red shifted tails that are clearly visible in the absence of the seed, have completely disappeared) as are all "whisker" features albeit at different angles due to the different dispersion properties in ethanol with respect to water.

An interesting observation related to energy measurements is the apparent improvement in the shot-to-shot energy stability of the output amplified seed pulse with respect to the input seed. For example a set of measurements in water we had an input seed energy $E_{in} = 130 \pm 30$ nJ corresponding to 23%

stability. At the sample output we measured an overall 7× gain in energy, $E_{out} = 920 \pm 63$ corresponding to a stability better than 7%. The input pump stability was 1.5% and we may expect intensity clamping to lead to a stabilization of the peak intensities reached within the filament [99] yet this is not sufficient to explain the amplified seed stability. In the low-gain regime the pump is not modified by the interaction with the seed and its dynamics may essentially be approximated by those of the filament with no seeding. Intensity clamping within the filament is explained as a balance between the self-focusing Kerr effect and plasma defocusing[1] and evidence has been reported of such an effect occurring in water [101] however even an ideal, non-fluctuating pump pulse, would be expected to amplify both the seed and its fluctuations. This clearly does not occur ([99]) so some non-trivial interaction between the seed and the pump filament is taking place that needs further investigation. On the other hand, in the pump depletion regime intensity clamping is much less likely and the seed output energy stabilization may simply be explained as an effect related to the pump depletion itself. A decrease in the pump intensity due to depletion will lead to a decrease in the seed gain so a lower energy seed pulse will gain a bit more than higher energy seed pulses with an overall leveling effect of any input fluctuations.

[1] It is important to note that this explanation, although valid for filaments in air should be extended with care in the case of condensed media. For example in water there are other competing mechanisms that may balance the Kerr effect such as nonlinear losses and group velocity dispersion.

References

[1] P.D. Maker and R.W. Terhune. Study of optical effects due to an induced polarization third order in the electric field strength. *Phys. Rev.*, 137(3A):A801–A819, 1965.

[2] P. Butcher and D. Cotter. *The Elements of Nonlinear Optics*. Cambridge University Press, U.K., 1990.

[3] L.W. Liou, X.D. Cao, C.J. McKinstrie, and G.P. Agrawal. Spatiotemporal instabilities in dispersive nonlinear media. *Phys. Rev. A*, 46(7):4202–4208, 1992.

[4] G.P. Agrawal. Modulation instability induced by cross-phase modulation. *Phys. Rev. Lett.*, 59(8):880–883, 1987.

[5] G.P. Agrawal. *Nonlinear Fiber Optics*. Academic Press Inc., San Diego, 1989.

[6] R.Y.Chiao, E. Garmire, and C.H.Townes. Self focusing optical beams. *Phys. Rev. Lett.*, 13(15):479–482, 1964.

[7] M. Hercher. Laser-induced damage in transparent media. *J. Opt. Soc. Am.*, 54:563–563, 1964.

[8] P. Lallemand and N. Bloembergen. Self-focusing of laser beams and stimulated raman gain in liquids. *Phys. Rev. Lett.*, 15:1010–1012, 1965.

[9] A. Couairon and A. Mysyrowicz. Femtosecond filamentation in transparent media. *Phys. Rep.*, 441:47–189, 2007.

[10] N. Aközbek, C.M. Bowden, A. Talebpour, and S.L. Chin. Femtosecond pulse propagation in air: a variational analysis. *Phys. Rev. E*, 61(4):4540, 2000.

[11] A. Braun, G. Korn, X. Liu, D. Du, J. Squier, and G.Mourou. Self-channeling of high-peak-power femtosecond laser pulses in air. *Opt. Lett.*, 20(1):73–75, 1995.

[12] A. Dubietis, E. Gaižauskas, G. Tamošauskas, and P. Di Trapani. Light filaments without self-channeling. *Phys. Rev. Lett.*, 92(25):253903, 2004.

[13] G.G. Luther, A.C. Newell, J.V. Moloney, and E.M. Wright. Short pulse conical emission and spectral broadening in normally dispersive media. *Opt. Lett.*, 19(11):789–791, 1994.

[14] J.E. Rothenberg. Pulse splitting during self-focusing in normally dispersive media. *Opt. Lett.*, 8(17):583–585, 1992.

[15] A. Couairon. Dynamics of femtosecond filamentation from saturation of self-focusing laser pulses. *Phys. Rev. A*, 68:015801–1, 2003.

[16] J.H. Marburger. Self-focusing: theory. *Progr. Quant, Electron.*, 4:35–110, 1975.

[17] A. Couairon, J. Biegert, C.P. Hauri, W. Kornelis, F.W. Helbing, U. Keller, and A. Mysyrowicz. Self-compression of ultra-short laser pulses down to one optical cycle by filamentation. *J. Mod. Opt.*, 53(1-2):75–85, 2006.

[18] J. Kasparian, R. Sauerbrey, and S.L. Chin. The critical laser intensity of selfguided light filaments in air. *Appl. Phys. B*, 71:877, 2000.

[19] A. Becker, N. Aközbek, K. Vijayalakshmi, E. Oral, C.M. Bowden, and S.L. Chin. Intensity clamping and re-focusing of intense femtosecond laser pulses in nitrogen molecular gas. *Appl. Phys. B*, 73:287–290, 2001.

[20] W. Liu, S. Petit, A. Becker, N. Aközbek, C.M. Bowden, and S.L. Chin. Intensity clamping of a femtosecond laser pulse in condensed matter. *Opt. Commun.*, 202:189–197, 2002.

[21] B. Prade, M. Franco, A. Mysyrowicz, A. Couairon, H. Buersing, B. Eberle, M. Krenz, D. Seiffer, and O. Vasseur. Spatial mode cleaning by femtosecond filamentation in air. *Opt. Lett.*, 31(17):2601–2603, 2006.

[22] F. Theberge, N. Aközbek, W. Liu, A. Becker, and S.L. Chin. Tunable ultrashort laser pulses generated through filamentation in gases. *Phy. Rev. Lett.*, 97:023904, 2006.

[23] M. Kolesik and J.V. Moloney. Self healing femtosecond light filaments. *Opt. Lett.*, 29(6):590–592, 2004.

[24] K.D. Moll and A. L. Gaeta. Self similar optical wave collapse: observation of the townes profile. *Phys. Rev. Lett.*, 90(20):203902–1, 2004.

[25] A. Brodeur, C.Y. Chien, F.A. Ilkov, S.L. Chin, O.G. Kosareva, and V.P. Kandidov. Moving focus in the propagation of ultrashort laser pulses in air. *Opt. Lett.*, 22(5):304–306, 1997.

[26] M. Mlejnek, E.M. Wright, and J.V. Moloney. Dynamic spatial replenishment of femtosecond pulses propagating in air. *Opt. Lett.*, 23(5):382–384, 1998.

[27] A. Couairon, E. Gaižauskas, D. Faccio, A. Dubietis, and P. Di Trapani. Nonlinear x-wave formation by femtosecond filamentation in kerr media. *Phys. Rev. E*, 73:016608, 2006.

[28] T. Brabec and F. Krausz. Nonlinear optical pulse propagation in the single cycle regime. *Phy. Rev. Lett.*, 78:3282–3285, 1997.

[29] P. Di Trapani, G. Valiulis, A. Piskarskas, O. Jedrkiewicz, J. Trull, C. Conti, and S. Trillo. Spontaneously generated x-shaped light bullets. *Phys. Rev. Lett.*, 91(9):093904–1, 2003.

[30] A. Dubietis, E. Kucinskas, G. Tamosauskas, E. Gaižauskas, M. A. Porras, and P. Di Trapani. Self-reconstruction of light filaments. *Opt. Lett.*, 29:2893–2895, 2005.

[31] M. Kolesik, E.M. Wright, and J.V. Moloney. Dynamic nonlinear x-waves for femtosecond pulse propagation in water. *Phys. Rev. Lett.*, 92(25):253901, 2004.

[32] M. Kolesik, G. Katona, J.V. Moloney, and E.M. Wright. Physical factors limiting the spectral extent and band gap dependence of supercontinuum generation. *Phys. Rev. Lett.*, 91(4):043905–1, 2003.

[33] M. Kolesik, E.M. Wright, and J.V. Moloney. Interpretation of the spectrally resolved far field of femtosecond pulses propagating in bulk nonlinear dispersive media. *Opt. Expr.*, 13(26):10729–10741, 2005.

[34] M. Kolesik, J.V. Moloney, and M. Mlejnek. Unidirectional optical pulse propagation equation. *Phys. Rev. Lett.*, 89(28):283902, 2002.

[35] J. Durnin, J.J. Miceli, and J.H. Eberly. Diffraction-free beams. *Phys. Rev. Lett.*, 58(15):1499, 1987.

[36] F. Gori, G. Guattari, and C. Padovani. Bessel-gauss beams. *Opt. Commun.*, 64:491–495, 1987.

[37] L.M. Soroko. *Meso-Optics*. World Scientific Pub., 1989.

[38] R.M. Herman and T.A. Wiggins. Production and uses of diffractionless beams. *J. Opt. Soc. Am. A*, 8(6):932–942, 1991.

[39] JR. P. MacDonald, J. Chrostowski, S. A. Boothroyd, and B. A. Syrett. Holographic formation of a diode laser nondiffracting beam. *Appl. Opt.*, 32:6470–6474, 1994.

[40] V. P. Koronkevich, I. A. Mikhaltsova, E. G. Churin, and Yu. I. Yurlov. Lensacon. *Appl. Opt.*, 34:5761, 1995.

[41] R.M. Herman and T.A. Wiggins. Production and uses of diffractionless beams. *J. Opt. Soc. A*, 8:932, 1991.

[42] A. Vasara, J. Turunen, and A.T. Friberg. Realization of general nondiffracting beams with computer-generated holograms. *J. Opt. Soc. A*, 6:1748, 1989.

[43] S. Klewitz, S. Sogomonian, M. Woerner, and S. Herminghaus. Stimulated raman scattering of femtosecond bessel pulses. *Opt. Commun.*, 154:186, 1998.

[44] C.J. Zapata-Rodriguez and M.A. Porras. X-wave bullets with negative group velocity in vacuum. *Opt. Lett.*, 31:3532, 2006.

[45] I. Alexeev, K.Y. Kim, and H.M. Milchberg. Measurement of the superluminal group velocity of an ultrashort bessel beam pulse. *Phys. Rev. Lett.*, 88:073901, 2002.

[46] P. Saari and K. Reivelt. Evidence of x-shaped propagation invariant localized light waves. *Phys. Rev. Lett.*, 79:4135, 1997.

[47] C.J. Zapata-Rodriguez and M.A. Porras. X-wave bullets with negative group velocity in vacuum. *Opt. Lett.*, 31:3532–3534, 2006.

[48] Y. Chen, K. Beckwitt, F.W. Wise, and B.A. Malomed. Criteria for the observation of multidimensional optical solitons in saturable media. *Phys. Rev. E*, 70:046610–1, 2004.

[49] J. Lu and J.F. Greenleaf. Ultrasonic nondiffracting transducer for medical imaging. *IEEE Trans. Ultrason. Ferrelec. Freq. control*, 37(5):438, 1990.

[50] J. Lu and J.F. Greenleaf. Nondiffracting x waves-exact solutions to free-space scalar waveequation and their finite aperture realizations. *IEEE Trans. Ultrason. Ferroelectr. Freq. Control*, 39(1):19–31, 1992.

[51] H. Sõnajalg, M. Rätsep, and P. Saari. Demonstration of the bessel-x pulse propagating with strong lateral and longitudinal localization in a dispersive medium. *Opt. Lett.*, 22:310–312, 1997.

[52] S. Orlov, A. Piskarskas, and A. Stabinis. Focus wave modes in optical parametric generators. *Opt. Lett.*, 27(23):2103–2105, 2002.

[53] D. Faccio, A. Averchi, A. Couairon, A. Dubietis, A. Matijošius R. Piskarskas, F. Bragheri, M. A. Porras, A. Piskarskas, and P. Di Trapani. Competition between phase-matching and stationarity in kerr-driven optical pulse filamentation. *Phys. Rev. E*, 74:047603, 2006.

[54] A.G. Van Engen, S.A. Diddams, and T.S. Clement. Dispersion measurements of water with white light interferometry. *Appl. Opt.*, 37:5679–5686, 1998.

[55] M.A. Porras and P. Di Trapani. Localized and stationary light wave modes in dispersive media. *Phys. Rev. E*, 69:066606–1, 2004.

[56] D. Faccio, M.A. Porras, A. Dubietis, , F. Bragheri, A. Couairon, and P. Di Trapani. Conical emission, pulse splitting, and x-wave parametric amplification in nonlinear dynamics of ultrashort light pulses. *Phys. Rev. Lett*, 96:193901, 2006.

[57] L. Brilloiun. *Wave propagation and group velocity.* Academic Press Inc., New York, 1960.

[58] P.W. Milonni. *Fast Light, Slow Light and Left-handed Light.* Taylor and Francis, Los Alamos, New Mexico, 2005.

[59] C. Conti, S. Trillo, P. Di Trapani, G. Valiulis, A. Piskarskas, O. Jedrkiewicz, and J. Trull. Nonlinear electromagnetic x waves. *Phys. Rev. Lett.*, 90(17):170406–1, 2003.

[60] Y. Silberberg. Collapse of optical pulses. *Opt. Lett.*, 15(22):1282–1284, 1990.

[61] C. Conti and S. Trillo. Nonspreadingwave packets in three dimensions formed by an ultracold bose gas in an optical lattice. *Phys. Rev. Lett*, 92(12):120404, 2004.

[62] M.A. Porras, A. Parola, D. Faccio, A. Dubietis, and P. Di Trapani. Nonlinear unbalanced bessel beams: Stationary conical waves supported by nonlinear losses. *Phys. Rev. Lett.*, 93(15):153902–1, 2004.

[63] A. Dubietis, G. Tamošauskas, I. Diomin, and A. Varanavičius. Self-guided propagation of femtosecond light pulses in water. *Opt. Lett.*, 28(14):1269–1271, 2003.

[64] T.D. Grow, A.A. Ishaaya, L.T. Vuong, A.L. Gaeta, N. Gavish, and G. Fibich. Collapse dynamics of super-gaussian beams. *Opt. Expr.*, 14:5468, 2006.

[65] R. Trebino. *Frequency Resolved Optical Gating: The Measurement of Ultrashort Laser Pulses*. Kluwer Academic Press, Boston, 2002.

[66] P. Gabolde and R. Trebino. Single-shot measurement of the full spatiotemporal field of ultrashort pulses with multispectral digital holography. *Opt. Expr.*, 14(23):11460–11467, 2006.

[67] J. Moses and F.W. Wise. Soliton compression in quadratic media: high- energy few-cycle pulses with a frequency-doubling crystal. *Opt. Lett.*, 31(12):1881–1883, 2006.

[68] B. Schenkel, J. Biegert, U. Keller, C. Vozzi, M. Nisoli, G. Sansone, S. Stagira, S. De Silvestri, and O. Svelto. Generation of 3.8-fs pulses from adaptive compression of a cascaded hollow fiber supercontinuum. *Opt. Lett.*, 28(20):1881–1883, 2003.

[69] D. Faccio, A. Matijošius, A. Dubietis, R. Piskarskas, A. Varanavičius, E. Gaižauskas, A. Piskarskas, A. Couairon, and P. Di Trapani. Observation of nonlinear x-waves in kerr media. *Phys. Rev. E*, 72:037601, 2005.

[70] D. Faccio, P. Di Trapani, S. Minardi, A. Bramati, F. Bragheri, C. Liberale, V. Degiorgio, A. Dubietis, and A. Matijošius. Far-field spectral characterization of conical emission and filamentation in kerr media. *J. Opt. Soc. Am. B*, 22(4):862–869, 2005.

[71] G.S. He, G.C. Xu, Y. Cui, and P.N. Prasad. Difference of spectral superbroadening behavior in kerr-type and non-kerr-type liquids pumped with ultrashort laser pulses. *Appl. Opt.*, 32(24):4507–4512, 1993.

[72] R.R. Alfano. *The Supercontinuum Laser Source*. Springer-Verlag, New York, 1989.

[73] I. Golub. Optical characteristics of supercontinuum generation. *Opt. Lett.*, 15(6):305–4307, 1990.

[74] E.T.J. Nibbering, P.F. Curley, G. Grillon, B.S. Prade, M.A. Franco, F.Salin, and A.Mysyrowicz. Conical emission from self guided femtosecond pulses in air. *Opt. Lett.*, 21(1):62–64, 1996.

[75] I. S. Golubtsov and O. G. Kosareva. Influence of various physical factors on the generation of conical emission in the propagation of high-power femtosecond laser pulses in air. *J. Opt. Technol.*, 69(7):462–467, 2002.

[76] O.G. Kosareva, V.P. Kandidov, A. Brodeur, C.Y. Chen, and S.L. Chin. Conical emission from laser-plasma interactions in the filamentation of powerful ultrashort laser pulses in air. *Opt. Lett.*, 22(17):1332–1334, 1997.

[77] F. Bragheri, C. Liberale, V. Degiorgio, D. Faccio, A. Matijošius, G. Tamosauskas, A. Varanavicius, and P. Di Trapani. Time-gated spectral characterization of ultrashort laser pulses. *Opt. Commun.*, 256(1-3):166–170, 2005.

[78] J.M. Dudley, G. Genty, and S. Coen. Supercontinuum generation in photonic crystal fiber. *Rev. Mod. Phys.*, 78:1135, 2006.

[79] L. Mandel and E. Wolf. *Optical Coherence and Quantum Optics*. Cambridge University Press, New York, 1995.

[80] J.W. Goodman. *Statistical Optics*. Wiley Interscience Publisher, New York, 1985.

[81] O. Svelto and D.C. Hanna. *Principles of lasers, Fourth edition*. Plenum Press, New York, 1998.

[82] O. Jedrkiewicz, A. Picozzi, M. Clerici, D. Faccio, and P. Di Trapani. Emergence of X-shaped spatiotemporal coherence in optical waves. *Phys. Rev. Lett.*, 97(24):243903, 2006.

[83] R.W. Boyd. *Nonlinear Optics*. Academic Press, New York, 2002.

[84] E. Yablonovitch and N. Bloembergen. Avalanche ionization and the limiting diameter of filaments induced by light pulses in transparent media. *Phys. Rev. Lett.*, 29(14):907–910, 1972.

[85] W.H. Press, S.A. Teukolsky, W.T. Vetterling, and B.P. Flannery. *Numerical Recipes*. Cambridge University Press, UK, 1992.

[86] J. Berenger. Three dimensional perfectly matched layer for the absorption of electromagnetic waves. *J. Comput. Phys.*, 127:363–379, 1996.

[87] D. Faccio, M.A. Porras, A. Dubietis, G. Tamosauskas, E. Kucinskas, A. Couairon, and P. Di Trapani. Angular and chromatic dispersion in kerr-driven conical emission. *Opt. Commun.*, 265:672, 2006.

[88] E.R. Peck and K. Reeder. Dispersion of air. *J. Opt. Soc. Am.*, 62:958, 1972.

[89] M.A. Porras, A. Dubietis, E. Kucinskas, F. Bragheri, A. Couairon, D. Faccio, and P. Di Trapani. From x- to o-shaped spatiotemporal spectra of light filaments in water. *submitted to Opt. Lett.*, 2005.

[90] M. J. Potasek. Modulational instability in an extended nonlinear schrodinger equation. *Opt. Lett.*, 12(11):921–923, 1987.

[91] S. Wen and D. Fan. Spatiotemporal instabilities in nonlinear kerr media in the presence of arbitrary higher-order dispersions. *J. Opt. Soc. Am. B*, 19(7):1653–1659, 2002.

[92] M.A. Porras, A. Parola, D. Faccio, A. Couairon, and P. Di Trapani. The spatiotemporal instability of the townes profile: From self-focusing to filament dynamics of ultrashort light pulses. *Phys. Rev. A*, in press, 2007.

[93] A.L. Gaeta. Catastrophic collapse of ultrashort pulses. *Phys. Rev. Lett.*, 84(16):3582–3585, 2000.

[94] F. Bragheri, D. Faccio, A. Couairon, A. Matijosius, G. Tamošauskas, A. Varanavičius, V. Degiorgio, A. Piskarskas, and P. Di Trapani. Conical-emission and shock-front dynamics in fs laser pulse filamentation. *Phys. Rev. A*, in press, 2007.

[95] F. DeMartini, C.H. Townes, Gustafson T.K, and P.L. Kelley. Self-steepening of light pulses. *Phys. Rev.*, 164(2):312–323, 1967.

[96] S.L. Chin, F. Théberge, and W. Liu. Filamentation nonlinear optics. *Appl. Phys. B*, 86:477–483, 2007.

[97] D. Faccio, A. Averchi, A. Couairon, M. Kolesik, J.V. Moloney, A. Dubietis, G. Tamošauskas, P. Polesana, A. Piskarskas, and P. Di Trapani. X wave generation by cross-phase-modulation induced spatio-temporal reshaping and amplification within optical filaments. *Opt. Expr.*, in press, 2007.

[98] M. Wittmann and A. Penzkofer. Spectral superbroadening of femtosecond laser pulses. *Opt. Commun.*, 126:308–317, 1996.

[99] F. Théberge, N. Aközbek, A. Becker W. Liu, and S. L. Chin. Tunable ultrashort laser pulses generated through filamentation in gases. *Phys. Rev. Lett.*, 97:023904, 2006.

[100] D. Faccio, A. Averchi, A. Dubietis, P. Polesana, A. Piskarskas, P. Di Trapani, and A. .Couairon. Stimulated-raman x-waves in ultrashort optical pulse filamentation. *Opt. Lett.*, 32:184, 2007.

[101] V.P. Kandidov, O. Kosareva, I.S. Golubtsov, W. Liu, A. Becker, N.Aközbek, C.M. Bowden, and S.L. Chin. Self-transformation of a powerful femtosecond laser pulse inot a white-light laser pulse in bulk optical media (or supercontinuum generation). *Appl.Phys. B*, 77:149–165, 2003.